Doctoral Thesis in Physics

Shape memory Heusler alloys for thin film applications

spintronics and magnetocalorics

Niclas Teichert

April 20, 2016

Bielefeld University
Department of Physics

Declaration

I wrote this thesis by myself and used none but the indicated resources. Text and figures were partly taken from corresponding publications, which originate directly from this work.

(Niclas Teichert)

Reviewers:

Prof. Dr. Andreas Hütten
Prof. Dr. Thomas Huser

Doctoral thesis
April 20, 2016

Contents

Introduction

The *martensitic phase transformation* (MT) is a structural instability best known as the underlying reason for the functional behaviors *shape-memory effect* and *superelasticity*. The MT describes a diffusionless first order solid to solid phase transformation between a high symmetry phase, called austenite, and a low symmetry phase, called martensite. The material transforms from austenite to martensite as it is cooled below the transformation temperature. Moreover, external stress, hydrostatic pressure, or, if at least one of the phases is ferromagnetic, an external magnetic field can be used to trigger the transformation or shift the transformation temperature. The functional behavior associated with a field induced transformation is called the *magnetic shape memory effect* (MSME).

The MSME was first reported by K. Ullakko in 1996 for the stoichiometric Heusler compound Ni_2MnGa.[1] Apart from Ni_2MnGa the MSME was found in related off-stoichiometric Heusler compounds $Ni_2Mn_{1+x}Z_{1-x}$, Z=Al, In, Sn, Sb where the exact composition is decisive for the transformation temperature.[2, 3] Along with the MSME these *magnetic shape memory alloys* (MSMAs) exhibit other effects like magnetoresistance [4] due to different electrical resistivity between austenite and martensite, and the *giant magnetocaloric effect*. In general, the magnetocaloric effect (MCE) describes a temperature or entropy change of a material subjected to a change of an external magnetic field. The largest field induced entropy changes are observed in the vicinity of coupled magnetic and structural, so-called magne-

tostructural transformations, and are therefore called *giant magnetocaloric effects*. This effect is expected to take a vital role in future solid-state refrigeration technology in order to supersede the conventional vapor refrigeration technology since it obviates the need for greenhouse gases as refrigerants and promises high cooling efficiency, estimated to be up to 75% of Carnot efficiency.[5] There is a variety of magnetocaloric materials under discussion for this purpose and among the most promising ones there are Heusler compounds like, e.g., Ni-(Co-)Mn-Sn and Ni-(Co-)Mn-In because they exhibit large field induced entropy changes and consist only of relatively inexpensive materials. The cobalt in these alloys is added at the expense of Ni in order to increase the Curie temperature and strengthen the ferromagnetism of the austenite phase of these compounds.

Another aspect of several magnetic shape memory Heusler compounds is that the martensite state at low temperatures exhibits a cluster spin-glass behavior,[6] i.e. a magnetically frustrated state consisting of ferromagnetic (FM) clusters in an antiferromagnetic (AF) matrix. A side effect of the cluster spin-glass is an intrinsic exchange bias (EB) effect. EB occurs at the interface between AF and FM ordered phases, e.g. in thin film structures, and leads to a shift of the coercive field of the FM phase. It is commonly used in spintronic applications like magnetic tunnel junctions where an antiferromagnet acts as a *pinning layer* for an adjacent ferromagnet to ensure an independent switching of two ferromagnetic electrodes and allows for them to be used as logic or memory devices. In the cluster spin-glass both FM and AF regions coexist, and therefore the EB is called *intrinsic* and has not yet been used in spintronics.

The focus of this work is to examine Heusler based MSMAs for applications beyond actuation by using epitaxial thin films. As a natural starting point we chose to examine the potential of the intrinsic EB of magnetic shape memory Heusler compounds for use in spintronic applications, which represents a classical thin film domain. Therefore, epitaxial Ni-Mn-Sn films are embedded as pinning layers into a CoFeB/MgO/CoFeB tunnel junction. Ni-Mn-Sn is chosen because the exchange bias effect in bulk samples [7] and thin films [8] is well studied and because the characteristics of the martensitic transformation in Ni-Mn-Sn films were extensively studied in previous work.[9–11]

The second thematic priority is to evaluate the potential of magnetocaloric Heusler compound thin films. In the field of magnetic refrigeration polycrystalline bulk or ribbon samples are commonly used since the absolute cooling

capability of a material is proportional to the amount of substance. However, the interest in thin film materials is growing because they are conceivable for nanotechnological cooling devices since they offer relatively fast heat transfer due to their large surface to volume ratio and also ductility if the films are freestanding. Moreover, epitaxial thin films represent an ideal model system for crystallographic studies on the martensitic structure because they are single crystalline and the crystallographic orientation is determined by the substrate. For this topic, Ni-Co-Mn-Al thin films are chosen because reports on this compound especially in thin films are sparse in the literature[12, 13] and for other candidates like Ni-Co-Mn-In [14] the field induced entropy change is much weaker than in comparable bulk samples. It also has to be considered that substrate constrained thin film are impractical for magnetocaloric applications because the substrate provides a massive heat sink with ideal thermal contact to the magnetocaloric films which dilutes any temperature change. Therefore, the magnetocaloric and crystallographic experiments were conducted on substrate constrained and freestanding films.

This thesis is organized as follows: In Chapter 2, the basics necessary for understanding this work will be stated, starting with the martensitic transformation, including its driving force and the origin of its microstructure in general and in epitaxial thin films. Moreover, the magnetocaloric effect will be explained and indirect methods to estimate magnetocaloric properties will be elucidated. Lastly, an introduction to the exchange bias effect in conventional ferromagnetic/antiferromagnetic heterostructures will be given and the origin of the intrinsic exchange bias in martensitic Heusler compounds will be clarified. Then, in Chapter 3, the sample preparation of substrate constrained and freestanding epitaxial films will be explained, and the analytical tools used for this thesis will be introduced.

Chapter 4 will present the experimental results of the implementation of Ni-Mn-Sn thin films as pinning layers in magnetic tunnel junctions. First, the structural properties of the Ni-Mn-Sn layer will be illuminated before the exchange bias effects as determined by magnetization measurements, is presented. Next, the exchange bias fields as extracted from tunnel magnetoresistance curves will be elucidated and compared to those from magnetization measurements.

The main chapter (Chapter 5) of this thesis deals with the analysis of magnetocaloric Ni-Co-Mn-Al thin films. In the first part, the sample quality and crystallographic properties of the films will be illuminated, where substrate

constrained films and freestanding films are considered separately. In the following section the magnetic properties of the films will be shown and based on the obtained results the magnetocaloric potential of selected films will be illuminated in the subsequent section. With all the results presented in this chapter, a phase diagram of Ni-Co-Mn-Al films will be set up and elucidated.

In Chapter 5 substrate constrained and freestanding Ni-Co-Mn-Al films will be characterized by means of structural characterization and magnetization measurements with the aim of exploring their potential as magnetocaloric materials. The scientific findings of this thesis will be summarized in Chapter 6. The final Chapter 7 will provide an outlook on some promising *work in progress* projects involving shape memory thin films related to our research.

Fundamentals

This chapter will provide the relevant theoretical basics for understanding this work. In the first section the martensitic transformation, its driving force, microstructure and the specifics for martensitic Heusler compounds will be introduced. In what follows the basics of the magnetocaloric effect will be presented. In the last section the classical model of the exchange bias will be shown and the current description of the exchange bias in Ni-Mn based Heusler compounds will be given.

Further reading about the specific topics is found in, e.g., the following references. Martensitic transformation and microstructure: Planes et al. [3], Bhattacharya [15], Song et al. [16], and Song et al. [17], martensitic Heusler compounds: Planes et al. [3], Auge [11], Kaufmann et al. [18], and Niemann [19], the magnetocaloric effect: Planes et al. [3], Smith et al. [20], and Buchelnikov et al. [21], and about exchange bias: Nogués and Schuller [22] and Ali et al. [23].

2.1 The martensitic transformation

The martensitic transformation is a first-order diffusionless solid to solid phase transition from a high temperature phase with high symmetry, called austenite, to a low temperature phase with a lower symmetry, called martensite. The transformation is displacive which means that one phase is a
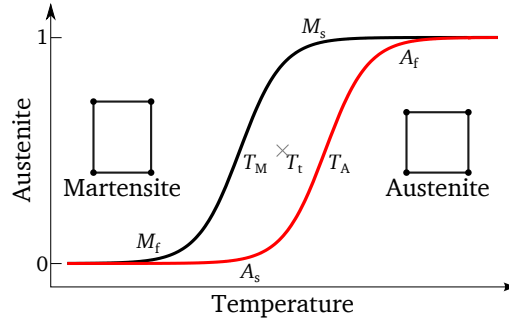
Figure 2.1. The characteristic transformation temperatures of the forward (black) and reverse (red) martensitic transformation.

distorted form of the other phase and involves some small displacement of the atoms.[24] Typical structural transformations are, e.g., cubic to tetragonal, cubic to orthorombic, cubic to monoclinic, or tetragonal to monoclinic. Fig. 2.1 sketches the the temperature dependence of the phase fractions of austenite and martensite during the martensitic transformation. The austenite-martensite or forward transformation occurs between the martensite start and martensite finish temperatures, M_s and M_f, respectively. Consequently, the martensite-austenite or reverse transformation temperatures are the austenite start (A_s) and austenite finish (A_f) temperatures. However, in many cases it is sufficient to consider only two transformation temperatures T_M and T_A which denote the inflection points in the transformation region or even only one transformation temperature T_t marking the center of the thermal hysteresis or the temperature of equal Gibbs free energy for martensite and austenite (cf. Sec. 2.1.1).

The diffusionless structural transformation can be described mathematically as a deformation by a Bain transformation matrix.[15] As an example the Bain transformation matrix from a cubic austenite with lattice parameter a_0 to a tetragonal martensite with lattice parameters a and c is described in Fig. 2.2. Depending on the material both types of tetragonal deformations, $c/a > 1$ and $c/a < 1$, are possible, where one of the lattice parameters is larger than a_0 and the other one is smaller because the volume change over the martensitic transformation is usually small.

Since the martensite has a lower symmetry than the austenite there are multiple possible orientations of the martensite lattice relative to the austenite
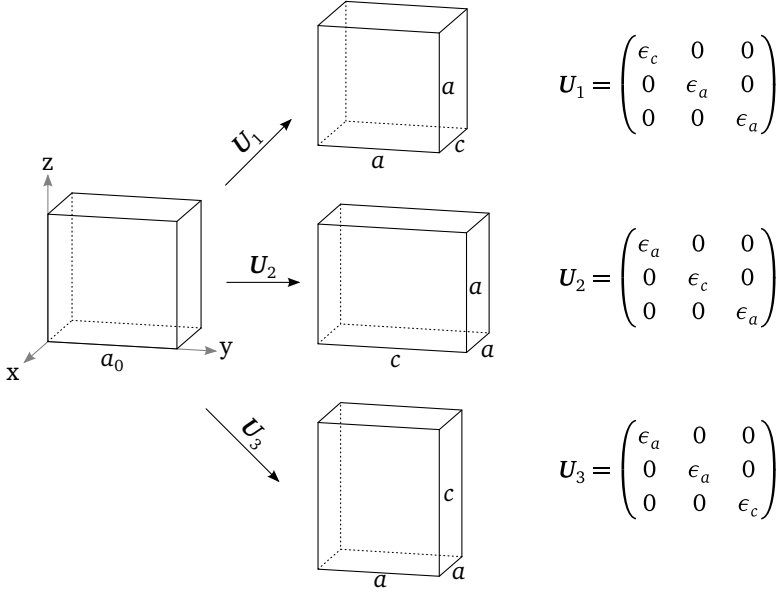
Figure 2.2. The different martensitic variants and related transformation matrices for a cubic to tetragonal martensitic transformation with $\epsilon_a = a/a_0$, $\epsilon_c = c/a_0$.

lattice. Those different orientations are called *martensitic variants* and the number of different martensitic variants is given by

$$N = \frac{\text{number of rotations in } \mathscr{P}_A}{\text{number of rotations in } \mathscr{P}_M} \tag{2.1}$$

where $\mathscr{P}_A$ and $\mathscr{P}_M$ are the point groups of the austenite and martensite lattice, respectively. So, for a cubic to tetragonal transformation we obtain $N = 24/8 = 3$ (cf. Fig. 2.2) and for cubic to orthorhombic $N = 24/4 = 6$.[15]

2.1.1 Gibbs free energy

The driving force of the martensitic transformation is the difference in Gibbs free energy $\Delta G = G_A - G_M$ between austenite and martensite. The Gibbs free energy is given as

$$G = U + pV - TS - \mu_0 HM - \sigma \epsilon V \tag{2.2}$$

with the pressure p, volume V, temperature T, entropy S, magnetic field H, magnetization M, mechanical stress σ, and strain ϵ. The total energy U at

$T = 0$ of the martensite structure is lower than for austenite due to a band Jahn-Teller effect, which splits the degenerate $3d$ states.[25] Furthermore, the volume of the martensite state is usually slightly reduced as compared to austenite. So, without any magnetic field or mechanical stress, the martensite is stable at low temperatures. However, the entropy of the austenite state is higher due to higher symmetry of the structure and lower phonon frequencies, and therefore, a higher temperature stabilizes the austenite. [24]

In addition to temperature, the martensitic transformation can also be triggered magnetically if at least one of the phases is ferromagnetic. The driving force for this *field induced transformation* is the difference in magnetization between both phases which leads to a difference in Gibbs free energy (cf. Eq. 2.2)

$$\Delta G = -\mu_0 H (M_{\mathrm{A}} - M_{\mathrm{M}}) \tag{2.3}$$

with the external field H and the magnetizations of austenite and martensite M_{A} and M_{M}, respectively. Thus, if the magnetization of austenite is higher than that of martensite, an external field will favor the austenite state and can induce the reverse transformation, i.e. the transformation temperatures T_{M} and T_{A} are field dependent and decrease through the application of a magnetic field. Typical shifts are in the order of a few K/T. A field induced martensitic transformation is accompanied by a magnetocaloric effect which is described in Sec. 2.2. The transformation temperature T_{t} is defined as the temperature where the Gibbs energies of austenite and martensite are equal, i.e.

$$G_{\mathrm{M}}(H, T_{\mathrm{t}}(H)) = G_{\mathrm{A}}(H, T_{\mathrm{t}}(H)). \tag{2.4}$$

Solutions to this equation satisfy the *Clausius-Clapeyron relation* for magnetic field induced phase transformations

$$\frac{\partial T_{\mathrm{t}}(H)}{\partial H} = -\mu_0 \frac{M_{\mathrm{A}}(H, T_{\mathrm{t}}) - M_{\mathrm{M}}(H, T_{\mathrm{t}})}{S_{\mathrm{A}}(H, T_{\mathrm{t}}) - S_{\mathrm{M}}(H, T_{\mathrm{t}})} \tag{2.5}$$

which can be used in experiment to estimate the total entropy change between two magnetic phases $\Delta S_{\mathrm{tot}} = S_{\mathrm{A}}(H, T_{\mathrm{t}}) - S_{\mathrm{M}}(H, T_{\mathrm{t}})$ from the shift of T_{t} with an applied external field.[1]

In the following, a simple approach[17] to estimate the Gibbs energy close to the martensitic transformation is introduced. Since the focus of this work

---

[1] In experiment, either T_{M} or T_{A} is used in Eq. 2.5, they differ from T_{t} if the transformation is accompanied by a thermal hysteresis.

is on temperature and field induced transformations we consider isobaric processes. Here, the Gibbs free energy is dependent on the temperature and magnetic field and the following Maxwell relations apply:

$$\frac{\partial G(H,T)}{\partial H} = -\mu_0 M, \quad \frac{\partial G(H,T)}{\partial T} = -S. \tag{2.6}$$

Integration of the first relation of Eq. 2.6 leads to

$$G(H,T) = -\mu_0 \int_0^H M(h,T)\,\mathrm{d}h + f(T) \tag{2.7}$$

where $f(T)$ is the field independent part of the Gibbs free energy.[17] By combining Eq. 2.6 with the definition of the heat capacity, we obtain

$$C(H,T) = T\frac{\partial S(H,T)}{\partial T} = -T\frac{\partial^2 G(H,T)}{\partial T^2} \tag{2.8}$$

which means that the zero field heat capacity is given as

$$C(0,T) = -Tf''(T). \tag{2.9}$$

From this, the field independent contribution to the Gibbs free energy is obtained by integration

$$f(T) = f(T_0) + \int_{T_0}^T \left[f'(T_0) - \int_{T_0}^T \frac{C(0,t_1)}{T}\,\mathrm{d}t_1 \right]\mathrm{d}t_2 \tag{2.10}$$

where as reference temperature T_0 usually the zero field transformation temperature ($T_0 = T_{\mathrm{t}}(H=0)$) is chosen. $f(T_0)$ and $f'(T_0)$ then denote integral constants. Using Eqs. 2.6 and 2.7 we obtain the entropy function

$$S(H,T) = \mu_0 \int_0^H \frac{\partial M(h,T)}{\partial T}\,\mathrm{d}h + \int_{T_0}^T \frac{C(0,t)}{t}\,\mathrm{d}t - f'(T_0) \tag{2.11}$$

Furthermore, at temperatures close to the phase transformation and if the field induced shift of T_{t} is small, it is often a good approximation to treat the heat capacities for each phase as constants C_{A} and C_{M} for austenite and martensite, respectively. So, the zero field entropy functions become

$$S_{\mathrm{M}}(0,T) = C_{\mathrm{M}}\ln(T/T_0) - f'_{\mathrm{M}}(T_0), \tag{2.12}$$

$$S_{\mathrm{A}}(0,T) = C_{\mathrm{A}}\ln(T/T_0) - f'_{\mathrm{A}}(T_0). \tag{2.13}$$

The difference of the integration constants yields the zero field latent heat

$$L = [S_A(0, T_0) - S_M(0, T_0)] \, T_0 \qquad (2.14)$$

and without loss of generality the integration constants are chosen to be

$$f_M'(T_0) = 0, \quad f_A'(T_0) = -L/T_0. \qquad (2.15)$$

So, the field independent Gibbs free energy (Eq. 2.10) becomes

$$f_M(T) = -C_M[T_0 - T + T \ln(T/T_0)] + f_M(T_0), \qquad (2.16)$$

$$f_A(T) = -C_A[T_0 - T + T \ln(T/T_0)] - L(T - T_0)/T_0 + f_A(T_0), \qquad (2.17)$$

and due to the condition that the Gibbs free energies of both phases are equal at the phase transition ($G_M(0, T_0) = G_A(0, T_0)$), the integral constants are chosen to be $f_M(T_0) = f_A(T_0) = 0$.

For the magnetic part of the Gibbs free energy one can model the magnetization functions of each phase according to molecular field theory by

$$M(H, T) = N_v \mu_m B_j \left(\frac{\mu_m \mu_0 (\gamma M + H)}{k_B T} \right) \qquad (2.18)$$

with the magnetic moment per formula unit μ_m, the number of spins per unit volume N_v, the molecular field constant γ, the Boltzmann constant k_B, and the jth Brillouin function

$$B_j(z) = \frac{2j+1}{2j} \coth \left(\frac{2j+1}{2j} z \right) - \frac{1}{2j} \coth \left(\frac{z}{2j} \right). \qquad (2.19)$$

The final Gibbs free energy planes $G(H, T)$ of each phase are estimated using the above considerations and plotted in Fig. 2.3(a).[2] High temperatures and magnetic fields favor the austenite phase over the martensite phase. The intersection of both planes, i.e. the phase boundary, marks the field dependent transformation temperature $T_t(H)$, which is described by the Clausius-Clapeyron relation (Eq. 2.5).

---

[2]The third law of thermodynamics dictates that $G(T)$ must be monotonically decreasing for all temperatures (i.e. $S(T) > 0$). To fix this, one could add a contribution $aT + b$ to $f(T)$ without changing the message of this chapter.
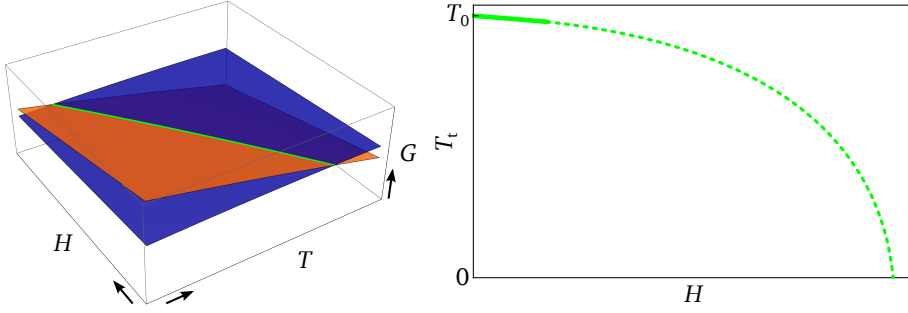
Figure 2.3. Gibbs free energy. (a) Typical temperature and field dependence of the Gibbs free energy of austenite (orange) and martensite (blue), calculated using the approximations given in the text. High temperatures as well as high fields stabilize the austenite phase. The phase boundary highlighted by a green line represents $T_t(H)$, which is also shown in (b). The dashed line is an extrapolation according to Song et al. [17].

The above considerations do not take into account the thermal hysteresis which is observed between the forward and reverse martensitic transformation. The transformation is driven by nucleation and growth of new phase nuclei, which causes an energy barrier and prevents the transformation directly at parity between G_M and G_A. The transformation starts as the nucleation barrier is exceeded by undercooling to the temperature $M_s < T_t$ for the forward transformation or overheating to $A_s > T_t$ for the reverse transformation and finishes after further undercooling or overheating at $M_f < M_s$ or $A_f > A_s$, respectively.

2.1.2 Martensitic microstructure

As mentioned above, at the critical temperature T_t martensite and austenite have the same Gibbs energy. The landscape of the joint Gibbs energy G of martensite and austenite depending on the lattice deformation around the martensitic transformation can schematically be described as in Fig. 2.4. At high temperatures above T_t the energy minimum is at zero deformation, therefore, the austenite is stable. At low temperatures the energy minimum is at finite deformations related to the transformation matrices U_1 and U_2, which means that the martensite is stable. However, the final deformation state the system will reach at low temperature is subject to boundary con-
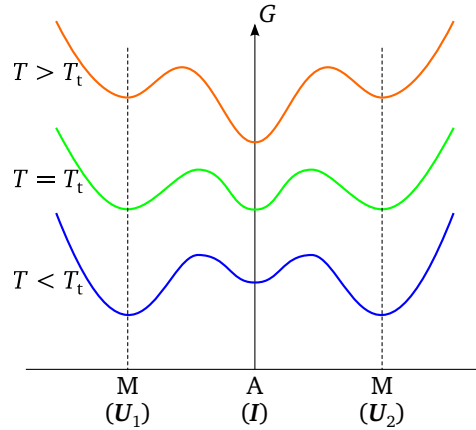
Figure 2.4. Gibbs free energy density as a function of the deformation at different temperatures. Adapted from Bhattacharya [15].

ditions which usually do not correspond to one of the energy wells. If the boundary condition is somewhere in between the energy wells, the system can accommodate it by making a mixture of the different wells so as to meet the boundary condition on average. This leads to fine twinning of the martensite phase. One important boundary condition is that of a coherent *habit plane* i.e. the martensite-austenite interface. Mathematically, the kinematic compatibility condition

$$F - G = a \otimes \hat{n} \tag{2.20}$$

ensures an *invariant plane* between two regions with deformations F and G where a and $\hat{n}$ are some vectors. $\hat{n}$ is the normal vector of the interface between the two regions.

For the austenite-martensite interface one of the matrices is the identity I and the other is QU_I where U_I corresponds to the Ith martensite variant and Q is some rotation. This example is visualized in Fig. 2.5(b) for the two dimensional case. In this 2D example a coherent habit plane is possible for a single martensitic variant, but it is already visible that the habit plane does generally not coincide with a low-indexed lattice plane.

For the austenite-martensite interface in the 3D case it can be shown that Eq. 2.20 is only valid if one eigenvalue of the transformation matrix U is equal to one, one smaller than one and one greater than one.[15] Generally, this condition is not fulfilled. This obstacle can be overcome by the martensite
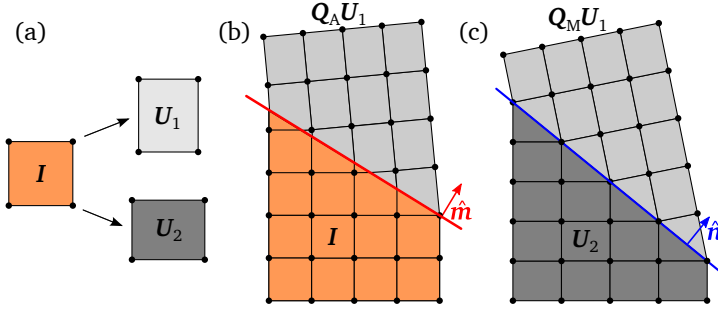
Figure 2.5. Kinematic compatibility condition between martensite and austenite. (a) The austenite transforms into the variants with transformation matrices U_1 and U_2. (b) and (c) visualize the habit plane equation (Eq. 2.22) and twinning equation (Eq. 2.21), respectively. The habit plane equation is fulfilled for $\lambda = 1$ in this two dimensional example.

phase by building up fine twins at the interface to the austenite. If we consider an alternation of two martensitic variants I and J at the habit plane with variant fractions λ and $1 - \lambda$, it is possible to form an exact habit plane if the following two equations based on the compatibility condition Eq. 2.20 are satisfied for some rotations Q, Q_I and Q_J and vectors a, b, $\hat{n}$ and $\hat{m}$:

$$QU_J - U_I = a \otimes \hat{n} \tag{2.21}$$

$$\lambda Q_J U_J + (1 - \lambda)Q_I U_I - I = b \otimes \hat{m} \tag{2.22}$$

Equation 2.21 is the *twinning equation* and is fulfilled if an invariant plane between the two variants with transformation matrices U_I and U_J exists. Equation 2.22 is the *austenite-martensite interface equation*. If the twins are not atomically small, an interpolation layer will form between austenite and martensite where the deformations match none of the energy wells shown in Fig. 2.4. If L is the length of the austenite-martensite interface, $\lambda L/n$ and $(1 - \lambda)L/n$ are the variant width where n is the number of twins. The thickness of the interpolation layer is then ξ/n (cf. Fig. 2.6).

The relevant energy contributions of the martensitic microstructure are the deformation energy and the interface energy. In order to minimize the deformation while fulfilling the boundary condition at the habit plane, a fine mixture of twins is necessary, optimally $n \to \infty$. However, the interface energy increases with the number of twin boundaries, and thus far away from
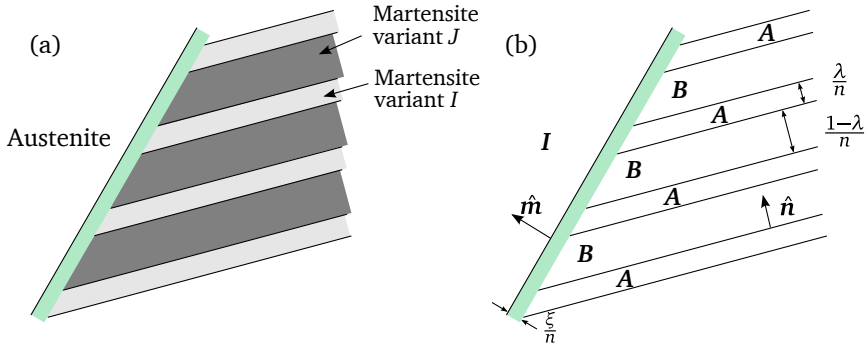
Figure 2.6. Microstructure at the austenite-martensite interface. (a) shows an alternation of two martensitic variants I and J at the habit plane. In (b) the sequence of deformations that meet the conditions Eq. 2.21 and Eq. 2.22 is sketched. $A = Q_I U_I$ and $B = Q_J U_J$ are the deformations corresponding to variants I and J and λ and $(1-\lambda)$ are the phase fractions. $\hat{m}$ and $\hat{n}$ are the orientations of the habit plane and the twinning plane, respectively. ξ/n is the width of the interpolation layer between austenite and martensite with a total number of n twins at the interface.

the habit plane $n \to 0$ is preferable. In reality, a microstructure as seen in Fig. 2.7 is observed close to the habit plane. The martensite builds up a fine laminate structure close to the habit plane and the variant width increases with increasing distance. This refinement process towards the interface is called *branching*.[15]

Despite a coherent interface to the austenite, it is also important for the martensitic structure to be able to embed within the austenite without generating macroscopic deformations. This so-called *self-accommodation* is of great importance for martensitic thin films on rigid substrates because the substrate prohibits any macroscopic deformation of the material. For a cubic austenite the necessary and sufficient condition for self-accommodation is volume preservation during the martensitic transformation. Mathematically this means $\det U_I = 1$.

Self-accommodation is the key condition for the functional behavior of martensitic materials and the following effects are only found in materials with only small volume change during the martensitic transformation. The most popular effect is the *shape memory effect*. This means that a material which was deformed in the martensite state recovers its original shape when transformed back to austenite. The effect is sketched in Fig. 2.8(a). In step 1
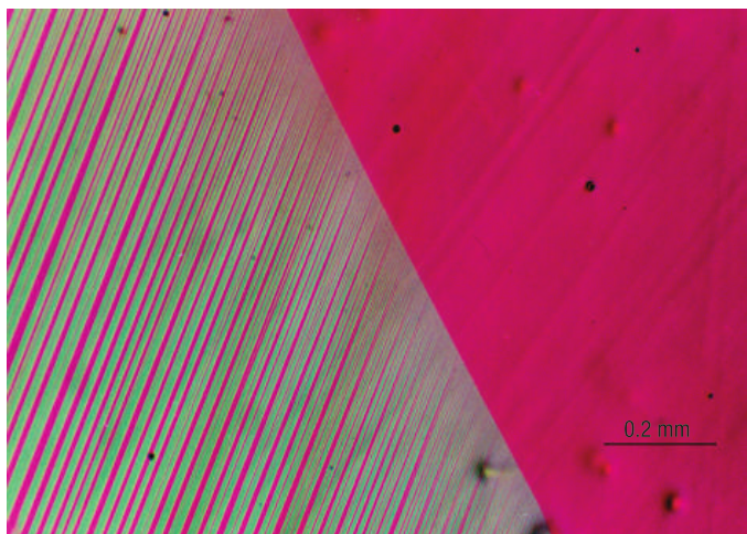
Figure 2.7. Optical micrograph of the martensite-austenite interface of Cu-Al-Ni. Reprinted by permission from Macmillan Publishers Ltd: Nature Materials (Cui et al. [26]), ©2006.

the material is in the austenite state, under cooling the material transforms into the martensite state without changing its macroscopic shape. An external stress σ favors martensitic variants with the long axis parallel to its direction and thus the material deforms (step 3). In step 4 the original shape can be recovered during the reverse transformation due to the displacive nature of the martensitic transformation.

A related effect is *superelasticity* (Fig. 2.8(b)). Here, the temperature of the material is kept constant slightly above the martensitic transformation temperature T_{M}. If stress is applied now, the material will first expand according to its elastic modulus. Under higher stress, however, it will transform into the martensite state with variants that have their long axis parallel to the stress direction. After releasing the stress the material will transform back to austenite. Superelasticity is widely used in medical braces and spectacle frames. The most prominent material for both superelasticity and shape memory effect is Ni-Ti around the equiatomic composition.

Furthermore, analogue to the shape-memory effect there is also the *magnetic shape memory effect* where, depending on the magnetic properties of
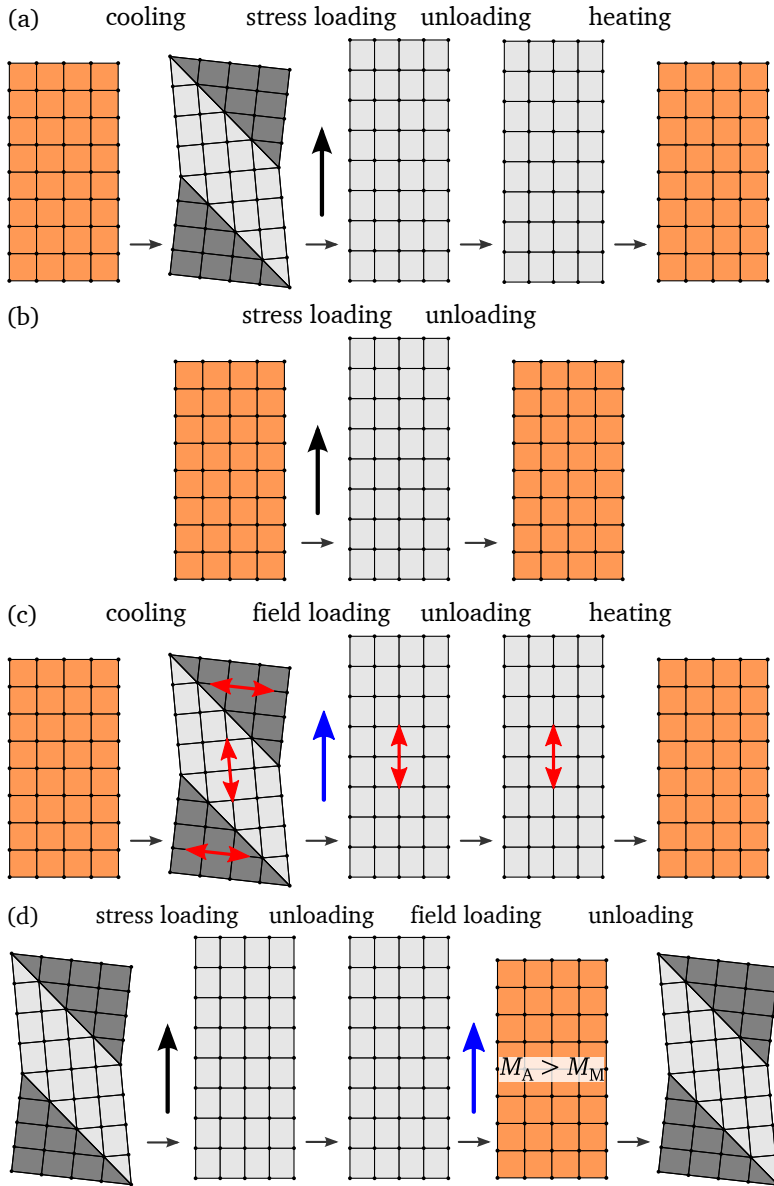
Figure 2.8. Sketches of (a) the conventional shape memory effect, (b) superelasticity, (c) the shape memory effect type 1 and (d) shape memory effect type 2. The basis for type 1 is a magnetocrystalline anisotropy in the martensite phase, and for type 2 a magnetization difference between martensite and austenite. Inspired by Planes et al. [3].

the material, an applied magnetic field has a similar effect as an external stress (type 1) or a temperature change (type 2): If the martensite state is magnetic, it is likely to show magnetocrystalline anisotropy due to the low symmetry. An external magnetic field will then favor martensitic variants with their magnetic easy axis parallel to the external field. Thus, the magnetic field can have a similar effect on the martensite to that of external stress (cf. Fig. 2.8(c)). The effect was found by Ullakko et al. [1] in 1996 in a Ni_2MnGa single crystal and later up to 10 % field induced strain was measured in off-stoichiometric Ni_2MnGa based single crystals.[3, 27] The type 2 magnetic shape memory effect (Fig. 2.8) is based on a field induced transformation due to a magnetization difference between martensite and austenite (cf. Sec. 2.1.1).

As sketched in Fig. 2.1, the martensitic transformation is accompanied by a thermal hysteresis between the forward and reverse transformations. The hysteresis resembles the energy barrier on the transformation path between the austenite and martensite. Two important factors for the hysteresis width are kinematic compatibility at the austenite-martensite interface and the volume change during transformation. The hysteresis is narrow if an exact austenite-martensite interface exists and if the martensite is self-accommodating. However, other physical parameters like the interfacial energy constant, the elastic moduli, transformation temperature and latent heat can also influence the hysteresis width.[26, 28]

Freestanding thin films

In thin films with two free surfaces the kinematic compatibility conditions for forming an interface between two martensitic variants or between one variant and austenite are less restrictive than for bulk. The conditions Eq. 2.21 and Eq. 2.22 for an invariant plane are simplified to *invariant line conditions*

$$(\boldsymbol{Q}\boldsymbol{U}_I - \boldsymbol{I})\hat{\boldsymbol{e}} = 0, \qquad \hat{\boldsymbol{e}} \cdot \hat{\boldsymbol{e}}_3 = 0 \tag{2.23}$$

$$(\boldsymbol{Q}\boldsymbol{U}_I - \boldsymbol{U}_J)\hat{\boldsymbol{e}} = 0, \qquad \hat{\boldsymbol{e}} \cdot \hat{\boldsymbol{e}}_3 = 0 \tag{2.24}$$

where $\hat{\boldsymbol{e}}$ is a unit vector and $\hat{\boldsymbol{e}}_3$ is normal to the film plane. As a result, under certain conditions it is possible for a single variant to form an exact interface to austenite.[15] The films relevant in this work are grown in $[001]_{cubic}$ direction and the condition for tetragonal martensite for the variants 1 and
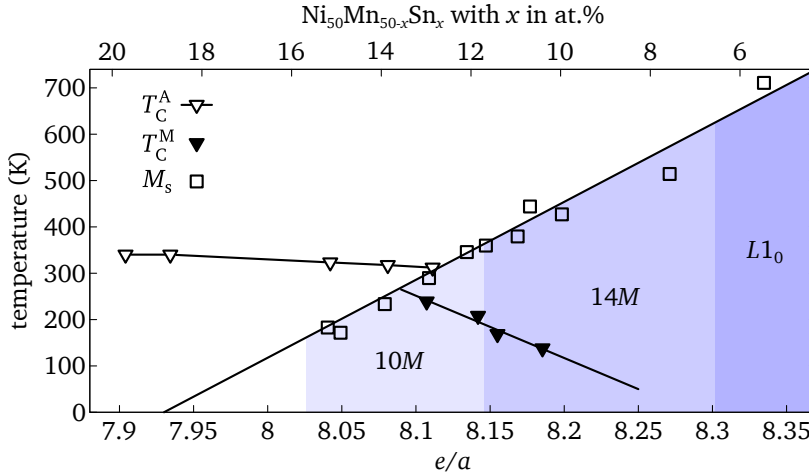
Figure 2.9. Magnetic and structural phase diagram of $Ni_2Mn_{2-x}Sn_x$. Figure taken from Auge [11]. The data points are taken from Planes et al. [3].

2 from Fig. 2.2 is $(\epsilon_a^2 - 1)(\epsilon_b^2 - 1) \leq 0$. For variant 3 with out of plane c-axis the invariant line condition with the austenite (Eq. 2.23) cannot be fulfilled. Martensite-martensite interfaces between each pair of variants are, however, possible in bulk and thin films. The twin boundaries coincide with $\{110\}_{cubic}$ lattice planes.

2.1.3 Martensitic transformation in Ni-Mn-based Heusler compounds

Several full-Heusler compounds from the Ni_2MnZ family where Z stands for, e.g., Al, Ga, Ge, In, Sn, or Sb, are known to exhibit martensitic transformations. Except for Ni_2MnGa, all of these only show the martensitic transformation in off-stoichiometric compounds where Mn is partly substituted for Z. The martensitic transformation temperature in those compounds is highly dependent on the valence electron concentration per atom, e/a, and hence, on the composition.[3, 29] As an example, the phase diagram for $Ni_2Mn_{1+x}Sn_{1-x}$ is given in Fig. 2.9.

In Fig. 2.10(a) the austenite crystal structure of $Ni_2Mn_{1+x}Z_{1-x}$ Heusler compounds is sketched. The $L2_1$ structure is a face centered cubic structure (space group $Fm3m$) with a four atom basis. The coordinates of the basis
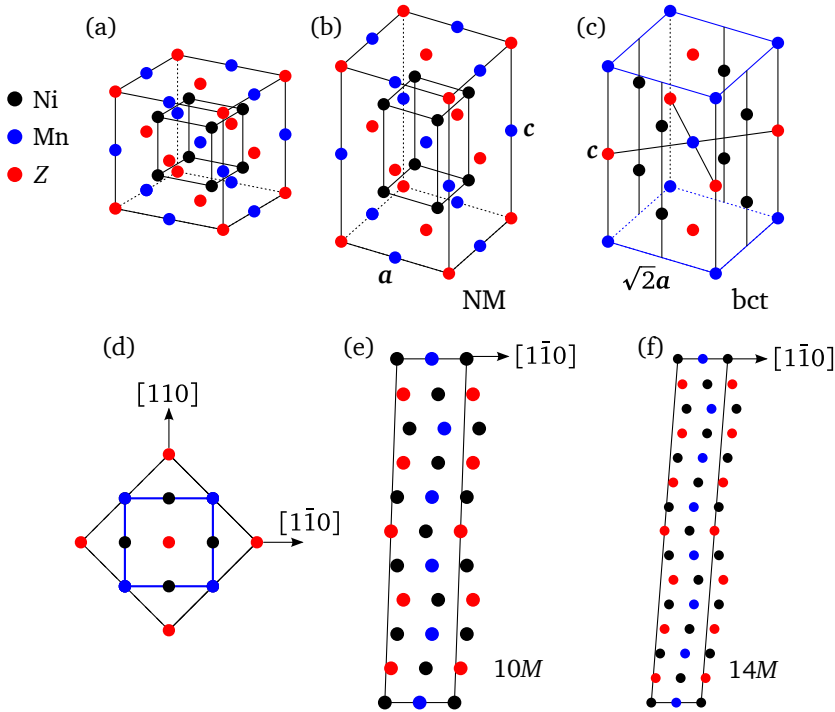
Figure 2.10. Crystal structures and notations of austenite and martensite. (a) shows the $L2_1$ unit cell of $Ni_2Mn_{1+x}Z_{1-x}$ Heusler compounds and (b) shows the tetragonal distorted cell, which is denoted as 'NM'. (c) shows the corresponding bct $D0_{22}$ unit cell and the relation between NM and bct cells is depicted in (d) in top view. (e) and (f) show $10M$ and $14M$ monoclinic tetragonal structures.

sites are $A = (0,0,0)$, $B = \left(\frac{1}{2}, \frac{1}{2}, \frac{1}{2}\right)$, $C = \left(\frac{1}{4}, \frac{1}{4}, \frac{1}{4}\right)$, and $D = \left(\frac{3}{4}, \frac{3}{4}, \frac{3}{4}\right)$ where Ni occupies the C and D sites, Mn the B site and due to the off-stoichiometry, the A site is partly occupied by Z and partly by the excess Mn atoms. In Wycoff notation, the A site is called 4a, the B site 4b and C and D are 8a sites. Intermixing of the atoms at the 4a and 4b positions (i.e. Mn and Z) leads to $B2$ ($Pm\bar{3}m$) structure, which is a common type of chemical disorder of the Heusler structure.[30]

Common martensitic crystal structures in these alloys are tetragonal $D0_{22}$ for $L2_1$ ordered austenite or $L1_0$ for $B2$ ordered austenite, and the modulated monoclinic structures $10M$ and $14M$ ('M' stands for monoclinic), which for $B2$ austenite are often also denoted as $5M$ and $7M$, respectively. Figure 2.10(b)

and 2.10(c) show the relationship between the body centered tetragonal (bct) unit cell and the $L2_1$ unit cell. The tetragonal structure is obtained from the cubic structure by distortion along one of the cubic axes and redefining the unit cell where two of the axes are obtained from $\langle 110 \rangle_{L2_1}$ axes (see Fig. 2.10(d)). For better comparability to the $L2_1$ structure we will use the lattice constants of the tetragonally distorted $L2_1$ 'NM' cell with all edges parallel to the cubic unit cell and the lattice parameters a_{NM} and c_{NM}. NM stands for *non-modulated martensite* in contrast to the modulated structures which are described below. The relations between the lattice constants of the bct and the NM unit cell are simply $a_{NM} = \sqrt{2}\, a_{bct}$ and $c_{NM} = c_{bct}$.

The modulated structures 10M and 14M are depicted in Fig. 2.10(e) and 2.10(f). They are both obtained from periodic stacking of (110) type austenite planes where each plane is slightly displaced in $[1\bar{1}0]$ direction relative to the neighboring planes. The periodicity of the modulation is $(5\bar{2})_2$ for 14M and $(3\bar{2})_2$ for 10M martensite. According to Khachaturyan et al. [31] the modulated structures can be interpreted as periodically nanotwinned bct structure which forms as an adaptive phase at the habit plane. Due to a twin coarsening mechanism, larger NM twins can originate from this structure with increasing distance to the habit plane. This coarsening does not necessarily occur since the total energies of the NM and the 14M martensite can be almost degenerate.[32] However, if larger NM variants originate from the 14M structure they must have the same crystallographic orientation as the nanotwinned variants.[33] This requirement was used to prove the concept of adaptive martensite for epitaxial Ni-Mn-Ga films by Kaufmann et al.[18] by using the single crystalline substrate as a reference system.

The adaptive 14M structure is sketched in Fig. 2.11. Here, we follow the procedure from Kaufmann et al. [18] and use for the 14M structure a unit cell with all edges almost parallel to the Heusler $L2_1$ cell. The lattice parameters of this cell are defined by the corresponding Bragg reflections arising from the periodical superlattice.[34] A nanotwinned superlattice consisting of two tetragonal variants with variant fractions λ and $1-\lambda$ gives the lattice parameters $a_{14M} \approx \lambda a_{NM} + (1-\lambda)c_{NM}$, $b_{14M} \approx \lambda c_{NM} + (1-\lambda)a_{NM}$ and $c_{14M} = a_{NM}$. Additionally, the concept of adaptive martensite dictates $b_{14M} = a_0$ in order to form a coherent austenite-martensite interface. With this confinement for b_{14M}, $a_{14M} = a_{NM} + c_{NM} - a_0$ follows.[18] The 14M unit cell in the common bct notation as sketched in Fig. 2.10(f) is indicated in gray in Fig. 2.11.
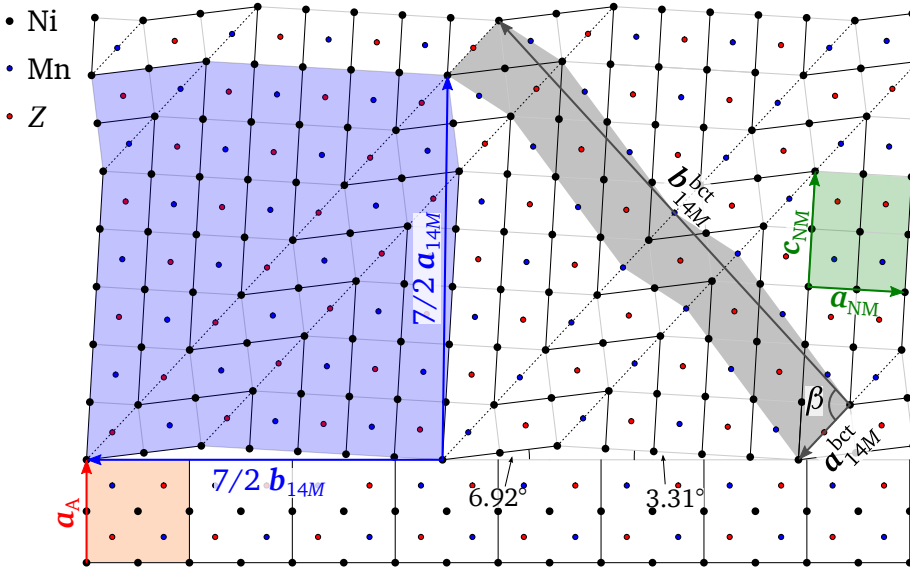
Figure 2.11. Concept of adaptive martensite. The sketch shows the modulated 14*M* structure (blue) as nanotwinned NM structure (green). In addition, the relationship between the bct notation (gray) and the notation based on the $L2_1$ unit cell (blue) is shown. The sketch is reproduced from [19] and is to scale with the lattice parameters of $Ni_{40.0}Co_{9.3}Mn_{32.9}Al_{17.8}$ (see Tab. 5.2, sample Al-17.8).

2.2 The magnetocaloric effect

The *magnetocaloric effect* (MCE) describes an adiabatic temperature change ΔT_{ad} or entropy change ΔS under a change of the external magnetic field from an initial field H_i to a final field H_f (cf. Fig. 2.12). The effect was discovered by Weiss and Piccard in Nickel in 1918.[35, 36] In a para- or ferromagnetic transition the magnetic field reduces the magnetic entropy by aligning the magnetic moments. Simultaneously the lattice entropy, and hence, the temperature increases. This effect is reversible, so if the field is removed after heat dissipation, the material cools down.

The largest magnetocaloric effects are observed in the vicinity of magnetic phase transitions where small fields can considerably increase the magnetic ordering. Therefore, Gd ($T_C = 293\,\text{K}$) was found to be the most suitable material for room-temperature applications and a first prototype of a magnetic regenerator was presented in 1976 by Brown [37]. In 1997, Pecharsky
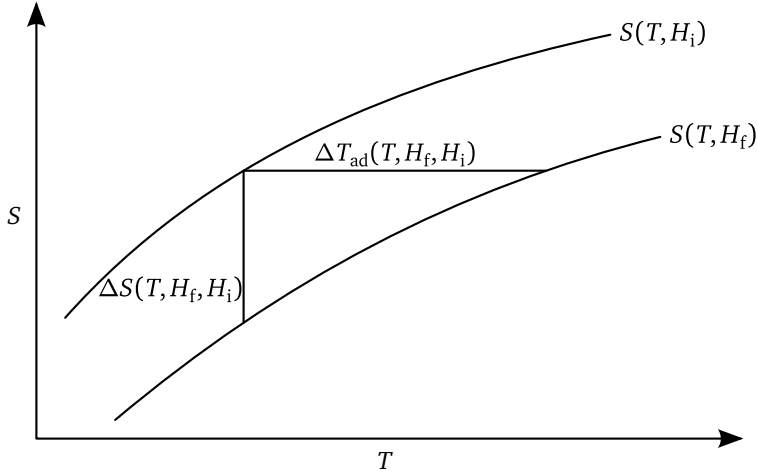
Figure 2.12. The magnetocaloric magnitudes ΔT_{ad} and ΔS between two entropy curves at different applied fields. Inspired by Smith et al. [20].

and Gschneidner reported the discovery of the so-called *giant magnetocaloric effect* in the vicinity of a first order magnetostructural phase transition of $Gd_5(Si_2Ge_2)$ close to room temperature.[38] This led to increasing scientific interest in the coupling of magnetic and lattice degrees of freedom and in magnetic refrigeration as an alternative to conventional gas compression technology. It is expected that the giant MCE will play a vital role in future environment friendly refrigeration technology since it obviates the need for greenhouse gases as refrigerants and promises high cooling efficiency, estimated to be up to 75 % of Carnot efficiency.[5, 20]

The entropy change under application of an external field is mainly dependent on a material's change in magnetization with temperature $\partial M / \partial T$ which is greatest near a magnetic phase transformation. Magnetocaloric materials can be divided into two classes depending on the sign of the temperature change when a magnetic field is applied: materials that exhibit the conventional magnetocaloric effect (cMCE) heat up ($\partial M / \partial T < 0$) and materials that yield the inverse magnetocaloric effect (iMCE) cool ($\partial M / \partial T > 0$) under application of a magnetic field.

At second-order ferromagnetic to paramagnetic transitions the conventional MCE is observed. At first order transitions both types of MCE can arise depending on the type of transition. Sizeable magnetocaloric effects

occur at magnetostructural or magnetovolume transitions between strong ferromagnetic or ferrimagnetic and weaker ferrimagnetic, antiferromagnetic and paramagnetic phases which are also called *metamagnetic* transitions.[5, 21]

In order to quantify caloric effects we start with the total differential of the entropy[3] assuming an isobaric process:

$$dS = \left(\frac{\partial S}{\partial T} \right)_H dT + \left(\frac{\partial S}{\partial H} \right)_T dH. \tag{2.25}$$

If we now use

$$\left(\frac{\partial S(H,T)}{\partial T} \right)_H = \frac{C(H,T)}{T}, \tag{2.26}$$

and consider an adiabatic process ($dS = 0$) we can rewrite Eq. 2.25 as

$$dT = -\frac{T}{C(H,T)} \left(\frac{\partial S}{\partial H} \right)_T dH. \tag{2.27}$$

The adiabatic temperature change is obtained by integration:

$$\Delta T_{ad}(H_f, H_i, T_i) = -\int_{H_i}^{H_f} \frac{T}{C(H,T)} \left(\frac{\partial S}{\partial H} \right)_T dH \tag{2.28}$$

with T_i as the temperature where the field change from H_i to H_f is initiated. This equation is usually simplified for evaluation of experimental data. For common materials and realistic field, and if T_i is close to room temperature, $T_i \gg \Delta T_{ad}$ is valid and $T(H) \approx T_i$ can be approximated. If furthermore the field dependence of C is ignored ΔT_{ad} can be directly related to the isothermal entropy change ΔS:[4]

$$\Delta T_{ad}(H_f, H_i, T_i) \approx -\frac{T_i}{C(H_f, T_i)} \Delta S(H_f, H_i, T_i). \tag{2.29}$$

Further, ΔS can be calculated using Eq. 2.26 leading to

$$\Delta S(H_f, H_i, T) = \int_0^T \frac{C(H_f, t)}{t} dt - \int_0^T \frac{C(H_i, t)}{t} dt \tag{2.30}$$

---

[3]Note that in section 2.1.1 the thermodynamic potentials of the austenite and martensite phase were treated separately while in this consideration $S(H,T)$ means the total entropy function of the material, which is possibly a mixed phase sample.

[4]ΔS is the field induced entropy change while ΔS_{tot} in Sec. 2.1.1 means the entropy difference between martensite and austenite at a given temperature and magnetic field. Therefore, $\Delta S_{tot}(H_f, T)$ is an upper limit for $\Delta S(H_f, H_i, T)$.

which shows that both magnitudes ΔS and ΔT_{ad} can be calculated from $C(H, T)$.

However, for small scale samples like thin films the heat capacity cannot be measured using standard methods and the thermodynamic magnitudes have to be approximated from better accessible quantities like temperature and field dependent magnetization measurements in our case. The approach for this is based upon the differential of the Gibbs free energy (Eq. 2.2) assuming an isobaric process

$$\mathrm{d}G = -S\,\mathrm{d}T - \mu_0 M\,\mathrm{d}H \tag{2.31}$$

with the vacuum permeability μ_0 and the fact that the second derivative of the Gibbs free energy ($\partial^2 G / \partial T\,\partial H$) is independent of the order of differentiation which leads to the following well known Maxwell relation:

$$\left(\frac{\partial S}{\partial H}\right)_T = \mu_0 \left(\frac{\partial M}{\partial T}\right)_H . \tag{2.32}$$

If this is now applied to Eq. 2.25 considering an isothermal process ($\mathrm{d}T = 0$) we obtain the *integrated Maxwell relation*

$$\Delta S_{\mathrm{m}} = \mu_0 \int_{H_{\mathrm{i}}}^{H_{\mathrm{f}}} \left(\frac{\partial M}{\partial T}\right) \mathrm{d}H . \tag{2.33}$$

So, by numerical evaluation of Eq. 2.33 the field induced entropy change can be approximated from temperature and external field dependent magnetization measurements.

Technically, the Maxwell relation is only applicable to second order phase transitions because in first order transitions the magnetization $M(T)$ is discontinuous. In reality, however, constraints and local variations of stoichiometry within the sample lead to a continuous 'second-order-like' transition and the results obtained from the Maxwell relation are in good agreement with those from direct differential scanning calorimetry measurements.[39]

2.3 The exchange bias effect

The exchange bias effect (EB) describes a unidirectional magnetic anisotropy resulting in a shift of the magnetic hysteresis along the direction of the applied field and was first observed for surface oxidized Co nanoparticles by Meiklejohn and Bean [40]. It is observed in structures with interfaces
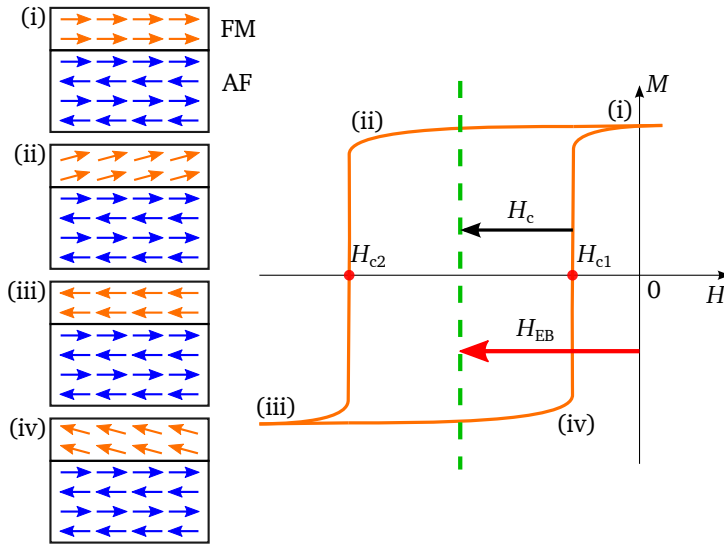
Figure 2.13. Classic model of the exchange bias effect. The left and right coercive fields, H_{c1} and H_{c2}, are shifted by the exchange bias field H_{EB}. Sketches (i)–(iv) schematically show the spin configuration at the corresponding points of the magnetic hysteresis. Inspired by Fan et al. [42].

between ferromagnetic (FM) and antiferromagnetic (AF) phases, e.g., thin film structures with adjacent FM and AF layers.[22] It is required for the EB that the Curie temperature T_C of the FM layer is higher than the Néel temperature T_N of the AF layer. When the structure is cooled through T_N with applied magnetic field, the magnetic moments of the antiferromagnet at the AF/FM interface align with the moments in the FM layer. This alignment pins the FM layer in this direction after the field is removed. The pinning, which leads to a shift of the magnetic hysteresis, is observed below the blocking temperature T_B of the antiferromagnet, where $T_B < T_N$. The orientations of magnetic moments in a layered AF/FM structure is sketched in Fig. 2.13. EB generated this way is commonly used to pin one of the magnetic electrodes in magnetic tunnel junctions (MTJs) (see below). EB is also observed, e.g., at spin-glass/FM interfaces [23] and in materials containing AF and FM clusters[41].
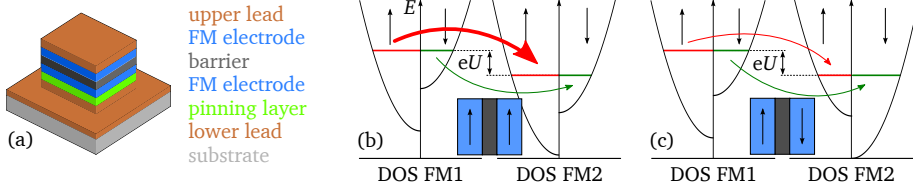
Figure 2.14. Magnetic tunnel junctions (MTJs) and tunnel magnetoresistance (TMR). (a) shows the typical layer stack of an MTJ. In (b) and (c) the spin resolved densities of states (DOS) around the Fermi level for the two magnetic electrodes for parallel (b) and antiparallel (c) configuration with applied voltage U are sketched.

2.3.1 Magnetic tunnel junctions

Trilayer structures consisting of two ferromagnetic metal layers separated by a thin insulating layer are called magnetic tunnel junctions (MTJs). The typical layer stack of an MTJ consisting of a tunnel barrier that is sandwiched between a pinned and an unpinned magnetic electrode and equipped with upper and lower electric leads is sketched in Fig. 2.14(a). The out-of-plane conductivity of an MTJ strongly depends on the mutual orientation of the magnetization of both magnetic layers. The density of states at the Fermi surface is spin dependent, which leads to a spin polarization of the current. Also the barrier thickness (typically 1-2 nm) is smaller than the spin diffusion length and the tunneling probability is increased if the density of states in the counter electrode is high. So, if both magnetic electrodes are of the same material, the resistance of the MTJ is lower in parallel alignment compared to antiparallel alignment (see Fig. 2.14(b) and 2.14(c)).

In order to achieve antiparallel orientation, either the coercive fields of both layers must be different from each other or the coupling between the layers at zero field must be antiferromagnetic. The common method to achieve different coercive fields is to pin one of the electrodes using the exchange bias effect. The most prominent applications of exchange biased MTJs are magnetic read heads in modern hard disk drives where the unpinned electrode is used to detect the stray field direction of the recording medium.

2.3.2 Exchange bias in martensitic Heusler compounds

In the martensitic phase of off-stoichiometric Ni-Mn based Heusler alloys an intrinsic exchange bias effect, i.e. a shift of the magnetic hysteresis, is

observed at low temperatures.[7, 43–46] Accordingly, these compounds are promising candidates for pinning ferromagnetic electrodes of MTJs without the commonly used antiferromagnets, MnIr and MnPt.[47–49] Replacing these materials in industrial applications is desirable because of the rarity and high cost of iridium and platinum. Since this effect is not observed in stoichiometric Ni_2MnGa, it is likely to be caused by the excess Mn atoms.[50] In Fig. 2.15 the *ab initio* calculated coupling constants for $Ni_{51.6}Mn_{32.9}Sn_{15.5}$ for a tetragonal martensite phase ($c/a = 1.2$) are shown.[51] The striking feature is that the Mn atoms on Mn sites (Mn_{Mn}) couple antiferromagnetically to the nearest neighbor Mn atoms on Sn sites (Mn_{Sn}) and ferromagnetically to the second nearest Mn_{Sn} while neighboring Mn_{Mn} atoms couple ferromagnetically. This leads to a formation of a so-called *cluster spin-glass* state at low temperatures consisting of FM clusters embedded in an AF matrix.[6] Bhatti et al. verified the inhomogeneity of the martensite phase of $Ni_{50-x}Co_xMn_{40}Sn_{10}$ ($x = 6$ and 8) at low temperature by small-angle neutron scattering measurements.[52] They estimate the size of the FM clusters to be 2–3 nm and the center-to-center spacing of these clusters to be 12 nm.[52, 53] During field cooling, the moments of FM clusters align along the external field and the AF moments align accordingly due to the exchange coupling which gives rise to the exchange bias effect.

More detailed studies including zero field cooling measurements of the off-stoichiometric Ni-Mn based Heusler alloys also show exchange bias at low temperature[8] but accompanied by reentrant spin-glass behavior due to strong magnetic frustration.[6, 54, 55]
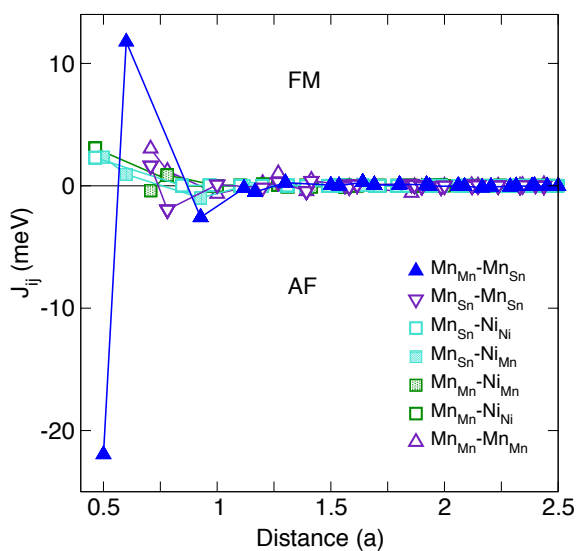
Figure 2.15. Calculated magnetic exchange parameters J_{ij} for tetragonal martensitic Ni$_{51.6}$Mn$_{32.9}$Sn$_{15.5}$ ($c/a = 1.2$) depending on the inter-atomic distance.[51]

Experimental details

This chapter gives a brief introduction to the preparation and analytical tools and methods used for this project. All films were prepared by magnetron sputtering. Selected films were released from the substrate by selective chemical wet etching of sacrificial V buffer layers. Structural analysis was done by X-ray diffraction measurements and for the chemical analysis X-ray fluorescence and energy dispersive X-ray spectroscopy were employed. For magnetometry either a vibrating sample magnetometer or a superconducting quantum interference device was used. The method for the electrical transport measurements shown in section 4.4 is briefly explained there. Basic knowledge about standard methods like atomic force microscopy (AFM), scanning electron microscopy (SEM) and transmission electron microscopy (TEM) is presupposed, thus these methods are not introduced here.

3.1 Thin film fabrication

The Ni-Mn-Sn and Ni-Co-Mn-Al Heusler compound thin films presented in this thesis were deposited by RF and DC magnetron co-sputtering on single crystalline MgO substrates with (001) orientation from elemental targets. For Ni-Co-Mn-Al, a V buffer layer is deposited before the Heusler layer in order to allow the fabrication of freestanding films (see below). The film thickness of
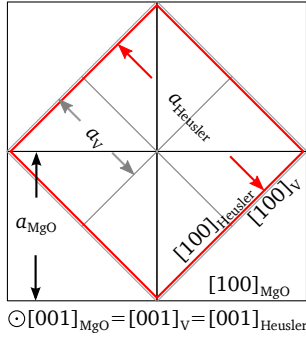
Figure 3.1. Epitaxial relation and lattice misfit between MgO substrate, V buffer layer and Heusler compound. The sketch is to scale with the bulk lattice parameters of MgO (4.212 Å), V (3.03 Å), and $Ni_{40}Co_{9.3}Mn_{32.9}Al_{17.8}$ (5.83 Å).

the V layer is typically 35 nm. On MgO(001) substrates, V grows epitaxially in [001] direction with a body-centered cubic structure and a lattice constant of $a_V = 3.030$ Å. Because $\sqrt{2}\,a_V \approx a_{MgO} = 4.212$ Å the in-plane lattice relation is $[100]_{MgO} \parallel [110]_V$. Furthermore, MgO(001) substrates with and without V seed layers induce epitaxial growth for many Heusler compounds including Ni-Co-Mn-Al and Ni-Mn-Sn due to the low lattice misfit.

The ultra high vacuum sputter chamber was constructed by BESTEC, BERLIN and is sketched in Fig. 3.2. It is equipped with six DC and two RF 3" sputter sources arranged in a confocal sputter-up geometry and allows for co-deposition from up to four targets. The substrate holder can be heated up to 900°C to optimize crystallization conditions and rotated for homogeneous film thickness and composition. As the sputter gas, high purity (6N) argon is used at a pressure of typically 2×10^{-3} mbar. The system is also equipped with an e-beam evaporator, which is mainly used to deposit protective MgO capping layers. For the deposition of additional layers the substrate can be transferred without breaking the vacuum to a second sputter chamber by LEYBOLD VACUUM equipped with seven sources for single source sputtering at room temperature. The film thickness is checked by means of X-ray reflectometry measurements.

3.1.1 Fabrication of freestanding films

The freestanding Heusler films presented in this thesis were prepared by a chemical wet etching technique of a sacrificial V buffer layer between the MgO substrate and the Heusler compound. For the wet etching process the commercially available etchant Cr ETCH No.1 by MICROCHEMICALS was used
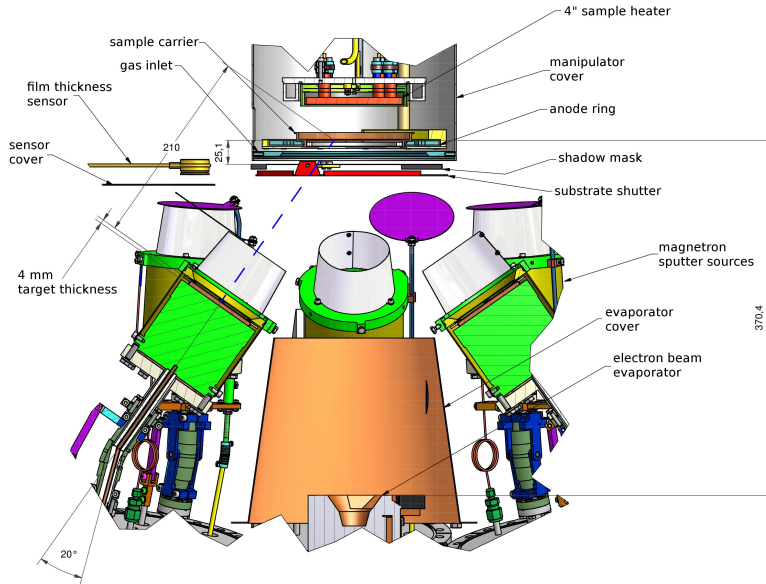
Figure 3.2. Technical drawing of the BESTEC co-sputtering machine.[56]

which is also suitable for etching V while leaving the investigated Heusler alloy films intact.

In order to release a several square millimeter thin film specimen the coated substrate is placed in the etchant for about 10 minutes until the film is visibly detached. Afterwards, the film can easily be peeled off the substrate, taken out of the etchant and placed in deionized water to neutralize the acid and subsequently cleaned in ethanol. Finally, the freestanding film can be placed upon any surface (e.g. TEM grid or Si wafer) for further characterization.

For the pole figure measurements shown in section 5.2.2 the freestanding film is kept on the original MgO substrate in order to ensure the same crystallographic orientation as the substrate constrained films.

3.2 Chemical composition analysis

The chemical composition of the Ni-Mn-Sn films was calibrated using X-ray fluorescence spectroscopy (XRF) with an Ag tube on separately prepared
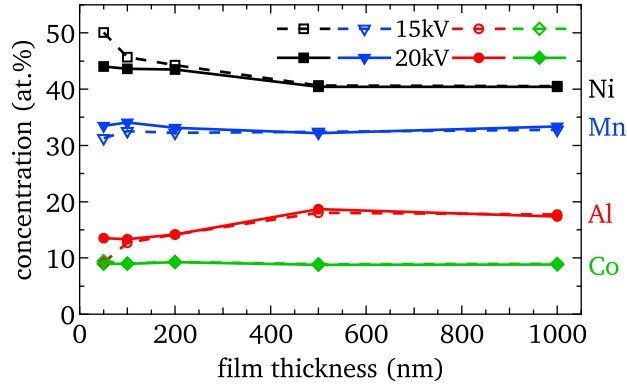
Figure 3.3. Results of quantitative EDX analysis of a Ni-Co-Mn-Al film thickness series with the same composition. Acceleration energies are 15 kV (dashed lines) and 20 kV (solid lines).

Heusler films on amorphous fused silica substrates. The spectra were measured with an AMPTEK XR-100CR Si-PIN detector and a digital pulse processor under He atmosphere. The Ag tube is operated at 40 kV and equipped with a 250 μm thick Al primary beam filter to reduce background and eliminate Ag-L lines from the spectrum. The measured spectrum is processed by removing escape and sum peaks, smoothing and background removal. Finally the processed spectrum is analyzed by means of a standardless fundamental parameters analysis.

Effects of reabsorption and secondary fluorescence are dependent on film thickness and density and taken into account by the software. However, they can still lead to considerable errors in the analysis of thick films, i.e. in samples which are neither within the bulk limit where the primary beam is completely absorbed in the sample nor within the limit of thin films where these effects can be neglected. The film thickness for the calibration samples was chosen to be 300 nm which is well within the thin film limit for Ni-Mn-Sn.

The validity of the results obtained can easily be checked by comparing the strongly composition dependent martensitic transformation temperatures to the phase diagram for bulk material (Fig. 2.9). As a result of the Al primary beam filter, characteristic lines of light elements below 3 keV (Al K_α, 1.49 keV) are suppressed [57] and therefore the composition of Ni-Co-Mn-Al was not determined by XRF. For this material energy-dispersive X-ray spectroscopy

(EDX) in a scanning electron microscope was chosen to quantify the chemical composition. The method is also standardless and based on a fundamental parameters analysis and the processing and analysis of the spectrum are analogous to XRF. However, due to the low penetration depth of electrons compared to X-ray photons and resulting multiple excitation events, there is a strong effect of the film thickness on the EDX spectrum, which leads to errors in the analysis. To account for this, the method was calibrated using a Ni-Co-Mn-Al film thickness series of constant composition (i.e. prepared using the same sputter powers). The results of the elemental analysis of this series are depicted in Fig. 3.3 at 15 kV and 20 kV acceleration voltage and it was found that the calculated compositions from EDX converge above 500 nm. Therefore, it was assumed that the results of the 1000 nm sample are closest to the real composition and the difference between the 1000 nm film and 200 nm film was used to estimate the real composition of other 200 nm films of similar composition. The statistical error of each point is below 1 at.%. The validity of the final results can also be checked by comparing the martensitic transformation temperatures to reported values for bulk material from the literature.

3.3 X-ray diffraction

X-ray diffraction (XRD) is the standard tool to determine the crystal structure of solids. Elastic scattering of X-rays with wavelength λ_X occurs due to constructive interference at a set of lattice planes with interplanar distance d. The diffraction angle θ can be calculated using Bragg's law

$$n\lambda_X = 2d \sin\theta \tag{3.1}$$

where n is the diffraction order. In an orthorhombic material the interplanar distance can be expressed with the lattice parameters a, b, c and Miller's indices h, k, l:

$$d_{hkl} = \frac{1}{\sqrt{\left(\frac{h}{a}\right)^2 + \left(\frac{k}{b}\right)^2 + \left(\frac{l}{c}\right)^2}}. \tag{3.2}$$

In tetragonal ($a = b$) and cubic ($a = b = c$) materials Eq. 3.2 simplifies accordingly. The structure factor $F(hkl)$ contains information about the
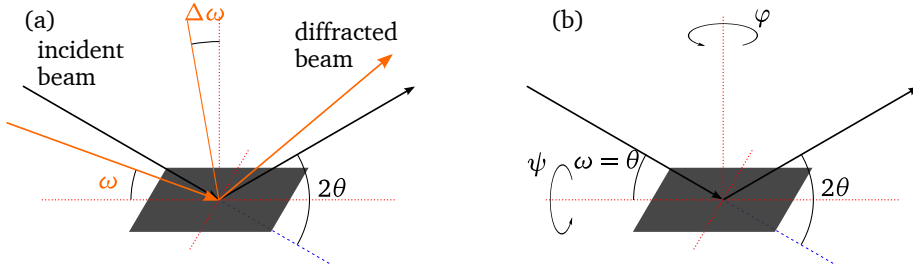
Figure 3.4. Sketch of the XRD geometries used. (a) Bragg-Brentano geometry and (b) open Eulerian cradle.

crystal structure and determines which (hkl) lattice planes give intensity in the XRD spectrum. It is given as

$$F_{hkl} = \sum_{n=1}^{N} f_n(\theta) \exp(2\pi i(hx_n + ky_n + lz_n)).$$ (3.3)

where the index n counts the atoms in the unit cell with coordinates (x_n, y_n, z_n) and atom form factors f_n.

The cubic Heusler structure consists of four interpenetrating fcc sublattices, denoted as A, B, C, D, with the average atomic form factors f_A, f_B, f_C, f_D. Thus, with Eq. 3.3 three types of reflections can be identified:

$$h,\ k,\ l \quad \text{all odd} \qquad F_{111} = \left| 4\sqrt{(f_A - f_C)^2 + (f_B - f_D)^2} \right|$$ (3.4)

$$(h + k + l)/2 = 2n + 1 \qquad F_{200} = |4[f_A - f_B + f_C - f_D]|$$ (3.5)

$$(h + k + l)/2 = 2n \qquad F_{400} = |4[f_A + f_B + f_C + f_D]|.$$ (3.6)

Only the reflections of the third type (Eq. 3.6) are not dependent upon chemical order and hence are called *fundamental reflections*. The XRD scans shown in this work were measured using a PHILLIPS X'PERT PRO MPD in Bragg-Brentano geometry as sketched in Fig. 3.4(a). The source is equipped with a Cu anode with $\lambda_X = 1.5419\,\text{Å}$ which is the weighted average of the K_{α_1} and K_{α_2} wavelength. The sample is fixed in the center of the goniometer and the source and detector move with equal but opposing angular velocity around the sample. This technique is only sensitive to lattice planes parallel to the sample plane. However, it is possible to give both goniometer arms an angular offset of $\Delta\omega$ while keeping the scattering angle 2θ unchanged,

which is necessary to observe martensitic lattice orientations that are tilted away from the sample surface. This offset is equivalent to an eucentric tilt of the sample by $\Delta\omega$ around the axis perpendicular to the scattering plane. The corresponding crystal axis can then be chosen by manually adjusting the in-plane orientation of the substrate on the sample stage. For the Bragg-Brentano geometry there is a custom built LN_2 cryostat available where the temperature can be adjusted between 150 K and 460 K.

For a detailed analysis of the real space orientation of martensitic variants a 4-circle goniometer with an open Eulerian cradle is used which allows us to set the sample orientation by an azimuth φ and polar angle ψ as shown in Fig. 3.4. This configuration only allows measurements at ambient temperature.

3.4 Magnetometry

The magnetic moment of the investigated films was studied using a vibrating sample magnetometer (Quantum Design PPMS at IFW-Dresden) and a super-conducting quantum interference device (SQUID, Quantum Design MPMS XL 7 at the Helmholtz-Zentrum Dresden-Rossendorf) with in-plane applied magnetic field. The sample mass was then calculated from the composition (cf. Sec. 3.2), the film thickness from XRR measurements, and the sample area which is measured using a digital optical microscope (KEYENCE VHX-600). The magnetization data is corrected for diamagnetic contributions of the MgO substrate which is easily identified in temperature and field dependent measurements because the diamagnetic susceptibility is negative, and independent of field and temperature.

Temperature and field dependent magnetization data was used to estimate the isothermal entropy change for selected films by numerical evaluation of the integrated Maxwell relation Eq. 2.33.

Exchange bias effect in Ni-Mn-Sn films for spintronic applications

This chapter demonstrates that the intrinsic exchange bias effect of Ni-Mn-Sn can be used to apply a unidirectional anisotropy to magnetic tunnel junctions. For this purpose, epitaxial Ni-Mn-Sn films were used as pinning layers for microfabricated CoFeB/MgO/CoFeB magnetic tunnel junctions. We compared the exchange bias field (H_{EB}) measured after field cooling in $-10\,\mathrm{kOe}$ external field by magnetization measurements with H_{EB} obtained from tunnel magnetoresistance measurements. Consistently for both methods an exchange bias field of about $H_{\mathrm{EB}} = 130\,\mathrm{Oe}$ at $10\,\mathrm{K}$ was found, which decreases with increasing temperature and vanishes above $70\,\mathrm{K}$. This chapter is based upon Teichert et al. [58].

4.1 Introduction

To guarantee a reliable readout in magnetic read heads based on magnetic tunnel junctions, at least one of the magnetic layers is pinned by an adjacent antiferromagnet. The technologically most relevant antiferromagnet for spintronic applications is MnIr. Currently, much scientific effort is put into finding a replacement material that does not contain iridium or other rare and costly materials.[59] For this, Ni-Mn-Sn represents a promising candidate due
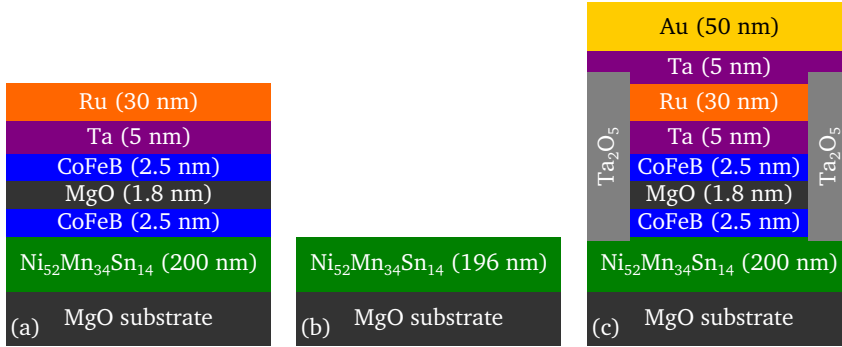
Figure 4.1. Sketches of the layer system: (a) as-deposited (sample A), (b) etched (sample B), and (c) after annealing and nanofabrication (sample C).

to its intrinsic exchange bias. Since it is magnetic as well, it could in principle serve as both pinning layer and magnetic electrode at once. However, as a magnetic electrode Ni-Mn-Sn is unfavorable because its spin-polarization is small.[60] Therefore, in our project the well established CoFeB[61] is used for the magnetic electrodes.

The samples used for this project were prepared by magnetron sputtering and subsequent e-beam lithography as follows. In a first step we deposited the 200 nm thick $Ni_{52}Mn_{34}Sn_{14}$ layer on MgO(001) substrates by co-sputtering from elemental targets. The substrate temperature during deposition was 650°C. After the deposition process the samples were cooled to room temperature and the additional layers $Co_{40}Fe_{40}B_{20}/MgO/Co_{40}Fe_{40}B_{20}/Ta/Ru$ were deposited with film thicknesses as shown in Fig. 4.1(a). This 'as-deposited' sample is referred to as sample A. To get a single $Ni_{52}Mn_{34}Sn_{14}$ layer as a reference sample the upper layers of sample A were removed by Ar ion beam etching while the progress is monitored by means of secondary ion mass spectrometry. Hereby, we obtain a 196 nm thick Ni-Mn-Sn layer on MgO substrate marked as sample B (cf. Fig. 4.1(b)).

In order to prepare the MTJs for tunnel magnetoresistance (TMR) measurements sample A is annealed at 350°C for one hour for proper crystallization of the CoFeB electrodes.[62] Afterwards, elliptical MTJs (300 nm × 180 nm) were patterned out of the layer stack by e-beam lithography and subsequent Ar ion milling. The ion milling was stopped right below the lower CoFeB layer in order to keep the Ni-Mn-Sn film intact. This is necessary because

the crystallite size of shape memory materials has a high impact on the transformation characteristics since the martensitic transformation can be impeded in too small crystals.[9, 63, 64] The MTJs were insulated by Ta_2O_5 and equipped with Ta/Au contact pads by RF and DC magnetron sputtering. This annealed and patterned sample is referred to as sample C and the final layer structure is sketched in Fig. 4.1(c).

The resistance-area product of the tunnel junctions in parallel configuration is RA= $3.0(6)\,k\Omega\,\mu m^2$, which is in good agreement with other reports on CoFeB/MgO/CoFeB MTJs.[48] Ni-Mn-Sn is known to show sizeable resistance changes in dependence of temperature and magnetic field.[9, 65, 66] However, those are part of the lead resistance which is three to four orders of magnitude smaller than the junction resistance and thus can be neglected.

4.2 Structural properties of the Ni-Mn-Sn layer

The crystal structure of the $Ni_{52}Mn_{34}Sn_{14}$ layer on single crystalline MgO(001) substrate (film B) was investigated using XRD. A θ–2θ scan (cf. Fig. 4.2(a)) reveals film growth in [001] direction because only the (002) and (004) reflections of the austenite phase of Ni-Mn-Sn are visible. The austenite lattice constant is $a_0 = 6.00\,Å$. Figure 4.2(b) shows a 360° φ-scan of the (022) reflection ($\psi = 45°$, $2\theta = 42.7°$) using a 4-circle goniometer where $\varphi = 0°$ is the MgO[100] direction. It shows the 4-fold symmetry and reveals epitaxial growth with the relation MgO(001)[110]‖Ni-Mn-Sn(001)[100]. The slight height difference of the four peaks originates from imperfect sample alignment. Figure 4.2(c) shows the Ni-Mn-Sn(111) peak at $\varphi = 0°$ and $\psi = 54.74°$ which demonstrates that the film crystallizes in $L2_1$ structure. Structural investigation of the martensite phase of epitaxial Ni-Mn-Sn films with very similar composition is found in Teichert et al. [9].

The inset of Fig. 4.2 shows an AFM micrograph of a separately prepared 200 nm $Ni_{52}Mn_{34}Sn_{14}$ film which reveals several nanometer high spikes at the surface of the film. Those spikes are unfavorable for the fabrication of magnetic tunnel junctions since they cause shortcuts in the MgO barrier and make it necessary to fabricate small MTJs that fit between the spikes. The contour of an MTJ is sketched in the micrograph as a black ellipse.
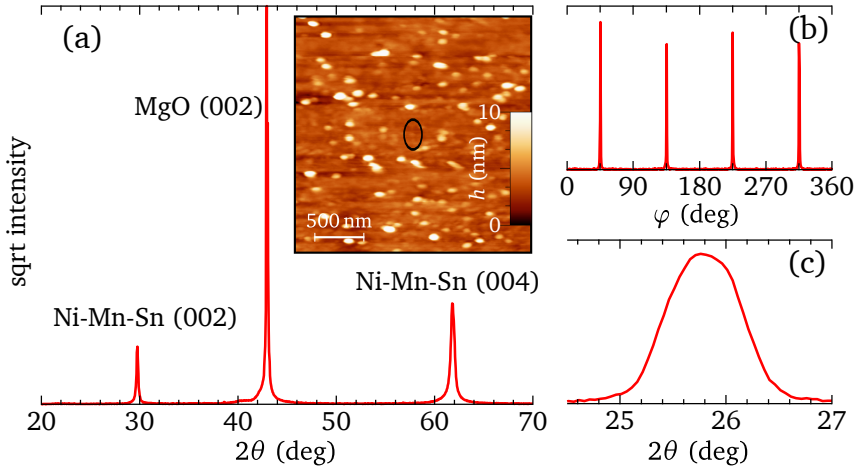
Figure 4.2. XRD patterns of MgO(substrate)/$Ni_{52}Mn_{34}Sn_{14}$(200nm) at room temperature. (a) In the gonio-scan the (004) and (002) peaks of the austenite phase are observed together with the MgO(002) peak. (b) 360° φ-scan of the Ni-Mn-Sn(022) peak at $\psi = 45°$ and $2\theta = 42.7°$ reveals epitaxial growth. (c) The 2θ-scan of the Ni-Mn-Sn(111) peak at $\varphi = 0°$ and $\psi = 54.74°$ shows that the film crystallizes in $L2_1$ structure. The inset of (a) shows an AFM micrograph of a separate $Ni_{52}Mn_{34}Sn_{14}$ layer which was originally prepared without additional layers. It exhibits spikes on the Ni-Mn-Sn, which limit the maximum size of the nanostructured MTJs. For scale, the contour of an MTJ is sketched as a black ellipse.

4.3 Magnetization measurements

In order to determine the magnetic properties and elucidate the martensitic transformation of the Ni-Mn-Sn film, the temperature dependence of the magnetization was studied. The given magnetization values are the measured magnetic moments normalized with the total volume of magnetic material (205 nm thickness for sample A and 196 nm for sample B). Figure 4.3(a) shows the magnetization versus temperature measured in low external field for samples A and B in field cooling (FC) and field heating (FH) modes, and (for sample A) during heating after the specimen was cooled in zero magnetic field (ZFC). Apart from the higher magnetization of sample A due to the presence of the magnetic CoFeB layers, samples A and B show the same temperature dependence. The distinct drop in magnetization upon cooling results from the martensitic transformation. For Ni-Mn-Sn, the
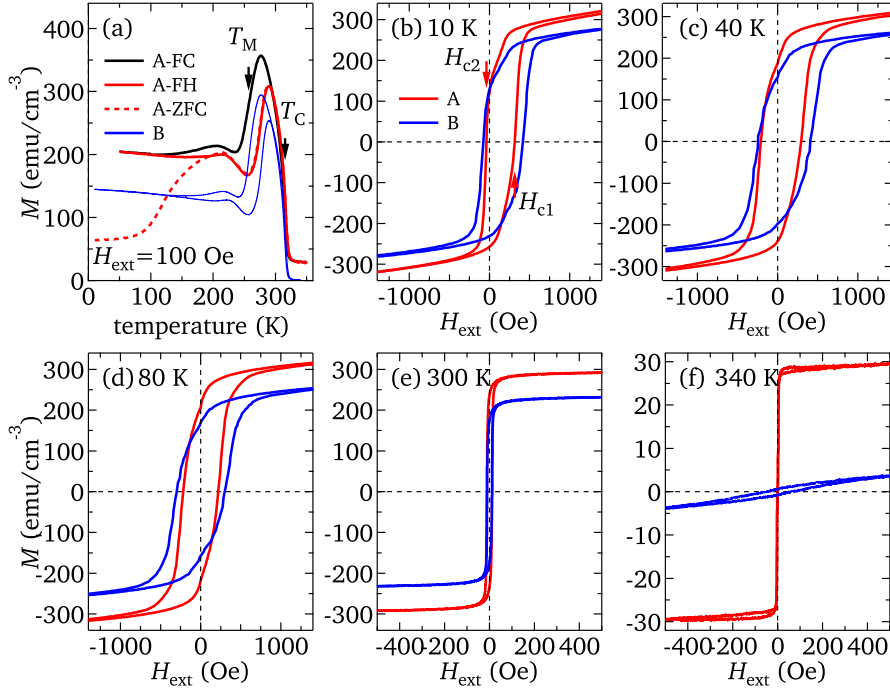
Figure 4.3. Magnetization measurements of samples A and B. (a) $M(T)$ curves at 100 Oe applied field. The FC (solid black line) and FH (solid red line) curves of sample A envelop a thermal hysteresis due to the martensitic transformation. The FH and ZFC (dashed red line) curves are split at low temperature. The martensitic transformation temperature T_M and Curie temperature T_C of Ni-Mn-Sn are indicated by arrows. FC and FH curves of sample A are shown as blue lines. (b)–(f) show $M(H)$ curves at different temperatures after field cooling at -10 kOe of samples A (red line) and B (blue line). The EB leads to a shift of H_{c1} and H_{c2} in positive field direction at low temperature.

magnetization of martensite is lower than of austenite. The reason for the magnetization change is a change in the alignment of magnetic moments of the Mn atoms on Mn sites (Mn_1) and Mn atoms on Sn sites (Mn_2) which are known to couple antiferromagnetically in austenite and martensite. However, due to changed lattice constants the antiferromagnetic coupling between Mn_1 and Mn_2 is increased in the martensite.[8, 67, 68] The martensitic transformation temperature and Curie temperature of the Ni-Mn-Sn are $T_M = 257$ K and $T_C = 316$ K, respectively, determined from inflection points

of the FC magnetization curve. Above T_C the magnetization of sample A drops to 27 emu cm^{-3}. This remaining magnetization results from the CoFeB, which has a higher Curie temperature. The splitting between the ZFC and FH curve originates from the coexistence of ferromagnetic and antiferromagnetic regions at low temperatures in the martensite phase, which is the basis for the EB (see also Sec. 2.3.2).[6, 29, 52]

The intrinsic EB in Ni-Mn-Sn is commonly determined via isothermal magnetization curves at low temperature after cooling the specimen in an external magnetic field. Figure 4.3(b)–4.3(f) depict the magnetic hysteresis loops of samples A (red lines) and B (blue lines) after field cooling to 10 K in a −10 kOe external field. From Fig. 4.3(b) and 4.3(c) it is clearly visible that at low temperatures the magnetic hysteresis is shifted and the positive coercive field H_{c1} is larger than the negative coercive field H_{c2}, which leads to a finite exchange bias field $H_{EB} = (H_{c1} + H_{c2})/2$ (see also Fig. 2.13). Above 80 K (Fig. 4.3(d)–4.3(e)) the curves are symmetrical and $H_{EB} = 0$. Above T_C (cf. Fig. 4.3(f)) the magnetization of sample B is small and sample A mainly shows the magnetization of CoFeB. The saturation magnetization (M_S) of CoFeB appears too small because the magnetic moment is normalized using a film thickness of 205 nm as described above. Considering only 5 nm leads to $M_S = 1150$ emu cm^{-3} for CoFeB, which coincides well with results from other studies.[69]

Apart from higher magnetization, sample A also shows lower coercive fields and lower H_{EB} than sample B due to the presence of CoFeB, which itself has low coercivity as seen in Fig. 4.3(f). However, from the $M(H)$ curves in Fig. 4.3 separate magnetic switching of one or both CoFeB layers is not observed. That means all magnetic layers are ferromagnetically coupled in the unpatterned sample A: the lower CoFeB layer is coupled by direct contact to the Ni-Mn-Sn and the upper layer most likely through pinholes in the MgO barrier.

The magnetization around the Curie temperature is further investigated by $M(H)$ measurements presented in Fig. 4.4. As expected from the $M(T)$ curves (Fig. 4.6(a)) the magnetization of sample B drops rapidly between 300 K and 340 K. Also, when comparing $M(T)$ of sample A with sample B at $T_C = 316$ K one can see that the magnetization of the CoFeB layers is comparable to the magnetization of the Ni-Mn-Sn layer.

Figure 4.4. $M(H)$ measurements of 196 nm thick Ni-Mn-Sn film (sample B) at 300 K, $T_C = 316$ K, and 340 K. For comparison $M(H)$ at 316 K is also shown for sample A. At T_C the magnetization of the CoFeB layers is comparable to that of the Ni-Mn-Sn.
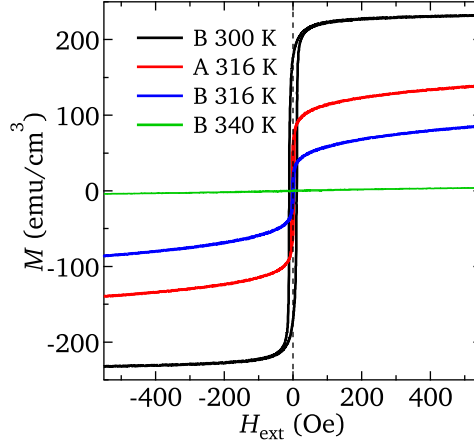
4.4 Tunnel magnetoresistance measurements

The TMR measurements shown in this chapter were carried out using a common 2-probe DC method with a constant 100 mV DC bias voltage in a Cryogenic He cryostat system where the external field is applied along the major axis of the elliptical MTJs.

4.4.1 Exchange bias

In what follows, the EB is determined from TMR measurements using sample C. Fig. 4.5 shows the TMR ratio defined as TMR $= (R-R_p)/R_p$ versus external field with the field applied along the major axis of the elliptical MTJs. R_p denotes the resistance at parallel alignment of both CoFeB electrodes, i.e. the resistance under high applied field. Here, the EB is defined as $H_{EB}^{TMR} = (H_{m1} + H_{m2})/2$ and deduced from H_{m1} and H_{m2}, which denote the external fields of maximum TMR under increasing and decreasing field, respectively. The exchange bias effect at low temperature is clearly visible from Fig. 4.5(a) and 4.5(b) since $H_{m1} > |H_{m2}|$ and vanishes above 80 K (Fig. 4.5(c)–4.5(f)) in agreement with Fig. 4.3(b)–4.3(f).

Below T_C (Fig. 4.5(a)–4.5(e)) the curves are asymmetrical and show spikes of maximum TMR with different amplitudes under increasing and decreasing external field. Furthermore, the TMR amplitude fluctuates around 30 % and does not show any systematic temperature dependence. This is caused by the absence of a fully antiparallel state of the magnetic electrodes and is
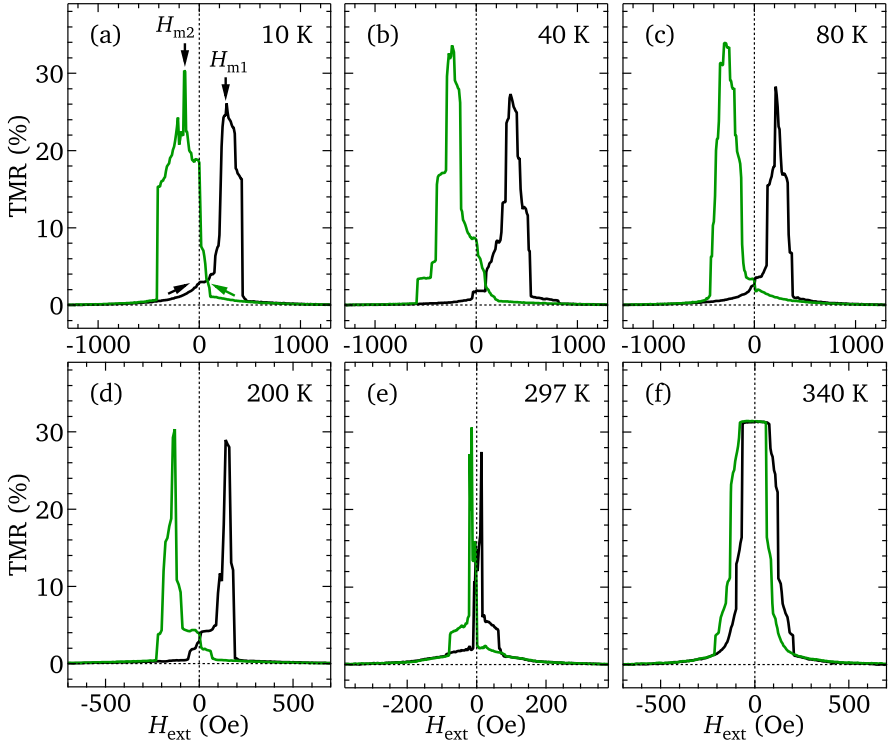
Figure 4.5. TMR curves measured using sample C at 100 mV bias voltage after field cooling at −10 kOe. Black and green lines are measured under increasing and decreasing field, respectively. At low temperature the EB is visible ((a) and (b)). (f) shows the TMR for paramagnetic Ni-Mn-Sn where the curve is symmetrical.

contrary to the situation above T_C (Fig. 4.5(f)) where symmetrical curves with a plateau of maximum TMR are observed. The resistivity change occurs in multiple steps which reflect Barkhausen jumps of domain walls in the upper CoFeB electrode and the lower electrode, where the magnetic part is a Ni-Mn-Sn/CoFeB bilayer below T_C and just CoFeB above T_C. Since the Ni-Mn-Sn layer was left intact during the patterning process the magnetic domains below T_C extend beyond the MTJs and are not pinned by their geometry. This causes a random influence on the shape of the resistance curves. Barkhausen jumps are not observed in the $M(H)$ curves in Fig. 4.3 because the measured sample area (several square millimeters) is much larger than the domain size, which is apparently not the case for the MTJs.

The plateau of maximum TMR at 340 K around $H_{ext} = 0$ reveals AF coupling of the magnetic electrodes in zero field. This can be explained by magnetostatic coupling of the CoFeB layers induced by uncompensated magnetic poles at the edges of the electrodes.[70] Contrary, below T_C, at zero applied field the alignment of the magnetic electrodes is only partly AF. The remanence of Ni-Mn-Sn is smaller than its saturation magnetization (cf. Fig. 4.3(b)–4.3(f)) and the AF coupling of the CoFeB electrodes is apparently too weak to fully align the magnetization of Ni-Mn-Sn below. A detailed discussion of the temperature dependence of the TMR is presented in Sec. 4.4.2.

The rather modest TMR amplitudes of maximum 34 % despite our choice of CoFeB as magnetic electrode material and 1.8 nm MgO barrier are probably caused by rather poor quality of the tunnel barrier. The surface roughness of the underlying Ni-Mn-Sn layer of $r_{rms} = 0.7$ nm (see the inset of Fig. 4.2(a)) when excluding the spikes is larger than that of conventional Ta underlayers ($r \approx 0.2$ nm [71]). This reduces the quality of the MgO barrier, and, hence, the TMR amplitude. Furthermore, the MTJ layer stack is not optimized by means of film thicknesses and selection of the optimum materials for the magnetic electrodes and the tunnel barrier in order to obtain maximum TMR.

4.4.2 Temperature dependence of the tunnel magnetoresistance

Figure 4.6 shows tunnel magnetoresistance (TMR) curves measured at different temperatures where at selected temperatures three sequentially measured loops are shown to demonstrate the non-reproducibility of the shape of the resistance curves. Up to 314 K all TMR curves are asymmetrical and non-reproducible because the magnetic switching is dominated by Barkhausen jumps of the underlying Ni-Mn-Sn layer in which the domain walls move independently from the size and position of the magnetic tunnel junctions (MTJs). Also, in the martensite state (below $T_M = 256$ K) the resistance always shows spikes of maximum TMR instead of plateaus and non-reproducible TMR amplitudes (cf. also Fig. 4.5(a)–4.5(c)). This clearly indicates that no fully antiparallel state of the magnetic electrodes is present. The reason for this is the rather complex domain structure in the martensite phase. The domain size and orientation of the magnetic easy axis is coupled to the size and orientation of martensitic variants in the film.[72] Based on the AFM micrograph in Fig. 4.7 of a structurally very similar 200 nm thick epitaxial
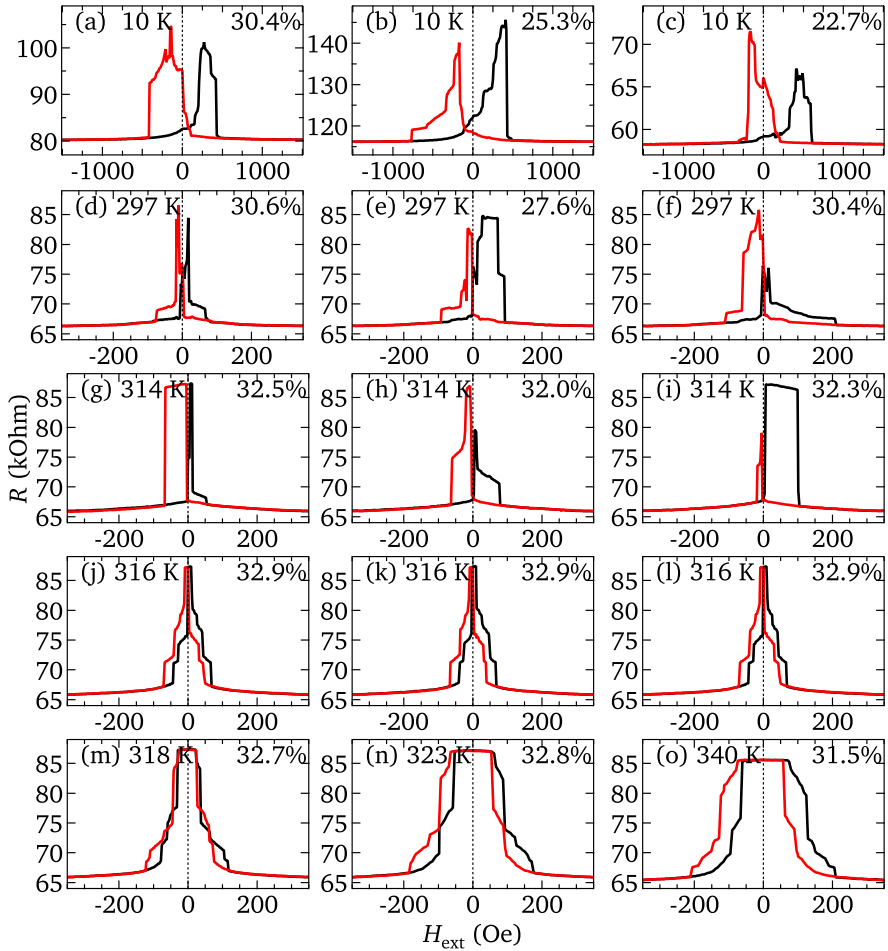
Figure 4.6. Tunnel magnetoresistance at different temperatures. (a)–(c) resistance curves of different MTJs at 10 K. Successively measured curves of the same MTJ at (d)–(f) 297 K, (g)–(i) 314 K, and (j)–(l) 316 K. (m), (n), (o) TMR at 318 K, 323 K, and 340 K, respectively. The TMR amplitude is given in the upper right corner. Black and red lines denote increasing and decreasing field, respectively. At low temperature the shape of the curves is non-reproducible but the exchange bias effect is clearly visible. When the Ni-Mn-Sn layer is austenitic and ferromagnetic the TMR is highly asymmetrical and non-reproducible (d)–(i). Above the Curie temperature of the austenite the curves are symmetrical and reproducible, and show antiparallel coupling at zero external field.
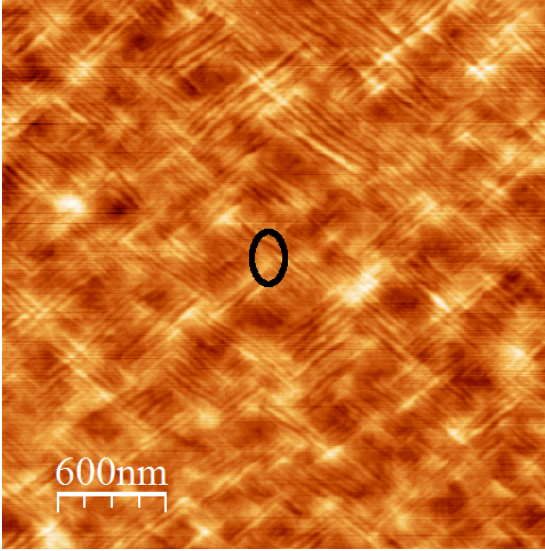
Figure 4.7. AFM micrograph of 200 nm thick epitaxial Ni-Co-Mn-Sn film at room temperature. The margins are parallel to the MgO[100] direction. The size of an MTJ is shown for scale as a black ellipse. The image shows traces of martensitic variants with a periodicity of approximately 50 nm. Therefore, the MTJ partly covers several martensitic variants.

$Ni_{50}Co_1Mn_{36.5}Sn_{12.5}$ film which is martensitic (10M) at room temperature we expect a domain width of about 50 nm. Because adjacent variants have different orientations of the magnetic easy axis it is likely that a fully antiparallel state of the MTJ cannot be achieved. Despite this random influence the exchange bias effect at low temperatures is clearly observed (Fig. 4.6(a)–4.6(c)). In the austenite phase below the Curie temperature of Ni-Mn-Sn ($T_C = 316$ K) antiparallel states are observed but not reproducibly (Fig. 4.6(d)–4.6(i)). Antiparallel states are observed at low fields but not at zero field. The increased Barkhausen noise just below T_C is probably attributed to an increased domain width in the austenite compared to the martensite. The shape of the curves changes drastically above T_C (Fig. 4.6(j)–4.6(o)): The TMR is symmetrical and reproducible and at zero field the electrodes are antiparallelly aligned. The plateau around zero field widens with increasing temperature. As described in Sec. 4.4.1, this is caused by stray field coupling between the CoFeB layers when the Ni-Mn-Sn magnetization vanishes (compare also Fig. 4.4).

4.4.3 Shape anisotropy of the elliptical MTJs

Due to the elliptical shape and the accompanying shape anisotropy of the MTJs we observe different $R(H)$ curves depending on the direction of the
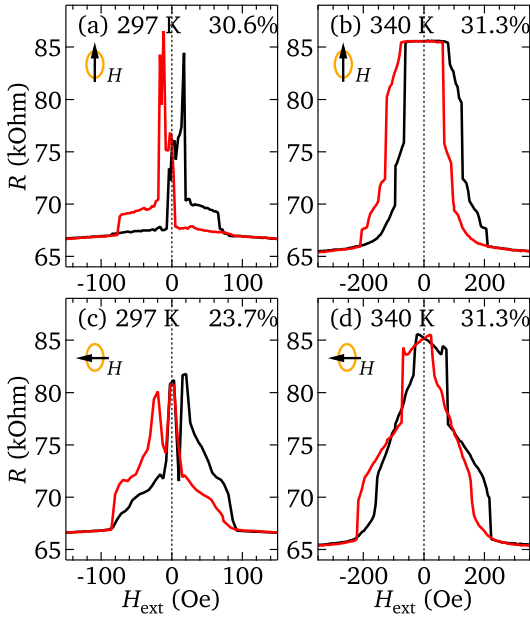
Figure 4.8. TMR curves with external field applied along the major axis (a)–(b) and along the minor axis (c)–(d) of the elliptical MTJs. Black and red lines denote increasing and decreasing external field, respectively. The TMR amplitude is given in the upper right corner.

external magnetic field. In Fig. 4.8 the TMR under different directions of the external field are compared for two different temperatures. In Fig. 4.8(a) and 4.8(b) the external field is applied parallel to the major axis and in Fig. 4.8(c) and 4.8(d) parallel to the minor axis of the ellipses. For both temperatures an external field applied along the minor (hard) axis instead of the major (easy) axis leads to broader TMR curves and more gradual magnetic switching due to the shape anisotropy of the elliptical MTJs. Furthermore, Fig. 4.8(c) and 4.8(d) show two maxima for each field direction where the maximum near zero field presumably corresponds to (partly) antiparallel configuration along the major axis and the other maximum presumably corresponds to partly antiparallel configuration along the minor axis.

4.5 Comparison

The temperature dependence of the EB is depicted in Fig. 4.9 where both methods of determining EB are compared. Figure 4.9(a) shows H_{c1}, H_{c2}, and H_{EB} as determined by magnetization measurements of samples A (red symbols) and B (blue symbols). At low temperature $|H_{c1}|$ and $|H_{c2}|$ are differ-
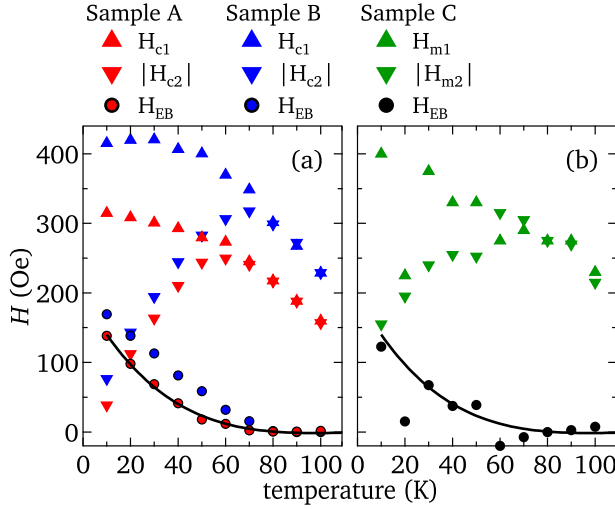
Figure 4.9. Temperature dependence of the EB after field cooling at $-10\,\text{kOe}$. (a) H_{c1}, H_{c2}, and H_{EB} determined from magnetization measurements of samples A (red symbols) and B (blue symbols). The black line is a guide to the eye and identical in (a) and (b). (b) H_{m1}, H_{m2}, and H_{EB} determined from TMR curves using sample C.

ent. With increasing temperature $|H_{c2}|$ strongly increases while $|H_{c1}|$ mildly decreases up to 60 K. Above 70 K the values of positive and negative coercive fields are equal and decrease with increasing temperature. Accordingly, H_{EB} strongly decreases with increasing temperature from $H_{EB} = 138\,\text{Oe}$ for sample A and $H_{EB} = 169\,\text{Oe}$ for sample B at 10 K to zero above 70 K. The magnitude and temperature dependence of H_{EB} of sample B is comparable to that of bulk Ni-Mn-Sn.[7, 43] Both coercive fields as well as H_{EB} of sample A are reduced by the CoFeB layers. The exchange bias effect in the lower CoFeB electrode is imprinted from the underlying Ni-Mn-Sn layer with larger magnetic moment. For comparison, pinning of CoFeB with MnIr leads to about $H_{EB} = 200\,\text{Oe}$ at room temperature.[73]

Figure 4.9(b) depicts the corresponding results from TMR measurements. The depicted data are average values obtained from TMR curves of two different MTJs measured during the first and second field loop at each temperature point. H_{m1} and H_{m2} show the same trends as H_{c1} and H_{c2}. As mentioned earlier, below T_C the measured TMR curves exhibit Barkhausen noise. This acts as a random influence on H_{m1} and H_{m2} and can be of the

same order of magnitude as the exchange bias which leads to a very small H_{EB} at 20 K and a negative H_{EB} at 60 K. Nevertheless, it is clearly visible from Fig. 4.9 that H_{EB} has the same magnitude and temperature dependence for samples A and C. So, the intrinsic EB of Ni-Mn-Sn can be observed in TMR measurements.

4.6 Conclusions

In summary, we investigated the exchange bias effect of MgO(substrate)/Ni-Mn-Sn/CoFeB/MgO/CoFeB and MgO(substrate)/Ni-Mn-Sn thin film structures after field cooling by two different methods: direct magnetization measurements and TMR measurements. Magnetization measurements are used to quantify the intrinsic EB of the Ni-Mn-Sn layer and the influence of the magnetic moment of the thin CoFeB layers. TMR measurements are sensitive to the interaction between the Ni-Mn-Sn layer and the CoFeB tunnel electrodes. Since we have shown a comparable EB effect in MTJs and magnetization measurements, we conclude that epitaxial Ni-Mn-Sn thin films can serve as pinning layers in these devices.

Besides these promising results, for the application of Ni-Mn based Heusler alloys as pinning layers in MTJs it has to be noted that the temperature dependence of the exchange bias and the TMR amplitude have to be improved in order to compete with MnIr as pinning layer. Therefore, as a first step the surface quality of the Heusler layer should be minimized by optimization of the growth conditions and composition. A flat surface improves the quality of the tunnel barrier and therefore the TMR amplitude. Moreover, it allows for the fabrication of MTJs with larger area which are less susceptible to Barkhausen jumps. In order to improve the exchange bias, the Ni-Mn Heusler family should be screened comprehensively for alloys with large blocking temperature.

Ni-Co-Mn-Al films for magnetocaloric applications

In this chapter the potential of Ni-Co-Mn-Al thin films for magnetocaloric applications is examined. For this purpose, structural, magnetic, and magnetocaloric properties of epitaxial Ni-Co-Mn-Al thin films with different compositions were studied and compared. Obviously, substrate constrained epitaxial films are unfavorable for magnetocaloric devices due to the heat sink provided by the substrate. So, selected films were released from the substrate in order to compare the magnetocaloric properties and to investigate the influence of the substrate constraint on the structural properties and the martensitic transformation.

We find that the martensitic transformation temperatures are strongly dependent on the composition and also differ between freestanding and substrate constrained films. The crystal structure of the martensite phase of substrate constrained films is shown to be a modulated adaptive 14*M* structure composed of tetragonal non-modulated building blocks. After detaching the film, the structure is simply tetragonal. The metamagnetic martensitic transformation occurs from strongly ferromagnetic austenite to weakly magnetic martensite. The structural properties of the films were investigated by atomic force microscopy and temperature dependent X-ray diffraction. Magnetic and magnetocaloric properties were analyzed using temperature de-

pendent and isothermal magnetization measurements. We find that substrate constrained and freestanding Ni-Co-Mn-Al films show giant inverse magnetocaloric effects with magnetic entropy change of up to $7.3\,\mathrm{J\,kg^{-1}K^{-1}}$ for $\mu_0\Delta H = 2\,\mathrm{T}$. This chapter is partly based upon Teichert et al. [74].

5.1 Introduction

In the ongoing search for magnetocaloric materials, Mn-rich Heusler compound based magnetic shape memory alloys (MSMA) of the system Ni-Mn-Z (Z=Sb, Ga, In, Sn) turned out to be very promising due to low cost of the containing elements and sizeable magnetocaloric effects (MCE).[3, 75, 76] Substitution of Co for Ni in Ni-Mn-Z is known to improve the metamagnetic behavior of the martensitic transformation, and thus the magnetocaloric properties, as it increases the austenite Curie temperature T_C^A and leads to a transformation from weakly magnetic martensite to ferromagnetic austenite.[77–81] The reason for the large change in magnetization at the transformation temperature is a change of the magnetic coupling between Mn atoms on Mn sites and Mn atoms on Z sites due to the change of the interatomic distances.[8, 67]

Off-stoichiometric Ni-Mn-Al also shows a martensitic transformation but only accompanied by small changes in magnetization and hence negligible MCE.[82, 83] The compound crystallizes in a $B2+L2_1$ mixed phase where the $B2$ phase is antiferromagnetic and the $L2_1$ phase is ferromagnetic.[2, 84, 85] Substitution of up to 10 at.% Co for Ni strongly promotes the ferromagnetism in the austenite phase and leads to a metamagnetic martensitic transformation.[81] The magnetization difference between austenite and martensite enables magnetic field induced reverse transformation together with an inverse magnetocaloric effect.[86–88]

Our interest is in epitaxial thin films of magnetocaloric materials as they present a good model system to study underlying physics due to the fixed crystallographic orientation. Additionally, thin films offer a high surface to volume ratio and also ductility if they are released from the substrate,[89] and thus they are promising for small scale magnetocaloric applications. In earlier studies we could show that the characteristics of the martensitic transformation and magnetocaloric properties of 200 nm Ni-Mn-Sn thin films

Table 5.1. List of the investigated thin films. The compositions are given in at.%. T_M and T_A denote the martensitic and austenitic transformation temperatures, and T_C the austenite Curie temperature. The film Al-19.1 does not show a martensitic transformation. Freestanding films are marked by an asterisk.

sample	Ni	Co	Mn	Al	T_M (K)	T_A (K)	T_C (K)
Al-19.1	39.4	9.2	32.3	19.1	no MT		408
Al-19.1*					245	316	
Al-18.4	39.7	9.3	32.6	18.4	206	323	411
Al-18.4*					342	391	
Al-17.8	40.0	9.3	32.9	17.8	348	388	415
Al-17.8*					391	445	
Al-16.4	40.7	9.5	33.4	16.4	425	450	424
1000 nm*	40.4	8.8	33.4	17.4	-	450	-

are comparable to those of bulk material,[9, 10, 66] so this film thickness was also chosen for the present project. Reports about Ni-Co-Mn-Al are sparse in the literature,[12, 13] and thus we want to provide insight into the structural and magnetocaloric properties of epitaxial Ni-Co-Mn-Al thin films.

For this experiment we prepared a set of four 200 nm films with different compositions and, hence, different transformation temperatures. Additionally, one film with 1000 nm thickness was prepared for structural investigations on freestanding films. The films were prepared by magnetron co-sputtering on MgO(001) substrates with 35 nm thick V buffer layers at a substrate temperature of 500°C. The composition differences in the 200 nm series were realized by different sputter powers on the Al source.

The film compositions as determined by EDX are listed in Tab. 5.1 together with the transformation temperatures determined from magnetization measurements as described below in Sec. 5.3. The films from the 200 nm series are labeled according to their Al content. Freestanding films are marked by an asterisk. The deviation from the real composition is estimated to be up to ±2 at.% but the relative composition differences within the 200 nm series are more precise. Within the error bars the given compositions and corresponding transformation temperatures are in good agreement with those from other studies on bulk material.[81]
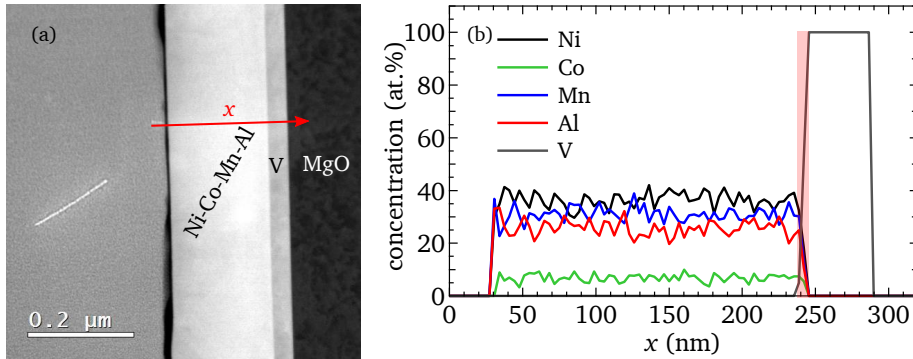
Figure 5.1. TEM image (a) and EDX line scan (b) of Al-17.8. The trace of the linescan is indicated in (a) as a red arrow. The red area in (b) marks the V/Ni-Co-Mn-Al interface.

5.2 Structure

5.2.1 Films on substrate

As a first verification of the sample quality, the V/Ni-Co-Mn-Al structure is checked for homogeneity of the chemical composition and sharpness of the interface, which are key conditions for all conclusions of this chapter. A sharp V/Ni-Co-Mn-Al interface is specifically important for the the preparation of freestanding films so that the Heusler layer is not damaged by the wet-etching process. Figure 5.1(a) shows a TEM image (provided by W. Hetaba, TU Wien) of a cross section of the film Al-17.8, which clearly reveals smooth V and Ni-Co-Mn-Al layers separated by a sharp interface. To check for interdiffusion across the interface, an EDX linescan was performed, which is presented in Fig. 5.1(b). It is evident that the V/Ni-Co-Mn-Al interface spans about 7 nm whereas the MgO/V interface spans only 4 nm, which represents the resolution limit of the linescan. So, some interdiffusion V/Ni-Co-Mn-Al interface cannot be excluded, but since it is locally confined to a few nanometers, no significant influence on the film properties is expected. It has to be noted that the absolute values of the Ni-Co-Mn-Al composition which can be read from the linescan do not fit the values given in Tab. 5.1 which are obtained from another EDX system (see Sec. 3.2), because the data of the linescan was not processed for quantitative analysis. Nevertheless, it
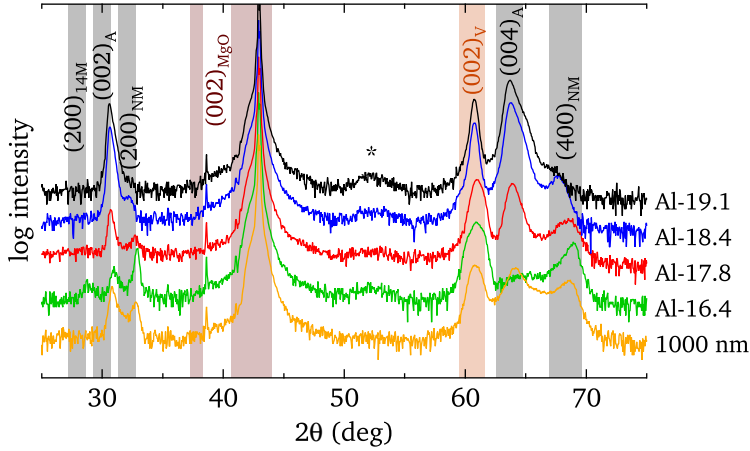
Figure 5.2. Room temperature XRD patterns of the investigated epitaxial Ni-Co-Mn-Al films on MgO substrate.

is clearly visible from Fig. 5.1 that the composition is homogeneous over the whole thickness, and promptly drops to zero at the V/Ni-Co-Mn-Al interface.

Figure 5.2 shows the XRD patterns of all analyzed films at room temperature (RT). The films are grown epitaxially with the relation MgO[100](001)∥Ni-Co-Mn-Al[110](001). At $2\theta = 64°$ the $(004)_A$ peak of the cubic austenite is visible. The existence of the $(002)_A$ superstructure peak at 30.5° indicates $B2$ structure. Odd superlattice reflections confirming $L2_1$ structure (e.g. (111)) were not found within further analysis using a four-circle goniometer. This is in accordance with other studies of bulk Ni-(Co-)Mn-Al, which report $B2$ as the dominating structure.[13, 81, 85] Nevertheless, we give the lattice constants with reference to $L2_1$ for comparability to other Heusler compound based MSMAs.[1] The $(400)_{NM}$ peak at 69° belongs to the martensite phase. From the $(004)_A$ and $(400)_{NM}$ peak intensities at room temperature it is visible that the amount of martensite at RT and thus the transformation temperature increases with decreasing Al content (i.e. increasing e/a), which is also reported for Ni-Mn-Al.[83] Further explanation of the indexing of the martensite reflections is found below.

Besides peaks belonging to Ni-Co-Mn-Al the $(002)_{MgO}$ peaks from the substrate at 42.9° (Cu K_α) and 38.6° (Cu K_β) and the $(002)_V$ peak of the

---

[1]Due to the higher symmetry, the $B2$ lattice constant is half the $L2_1$ value.
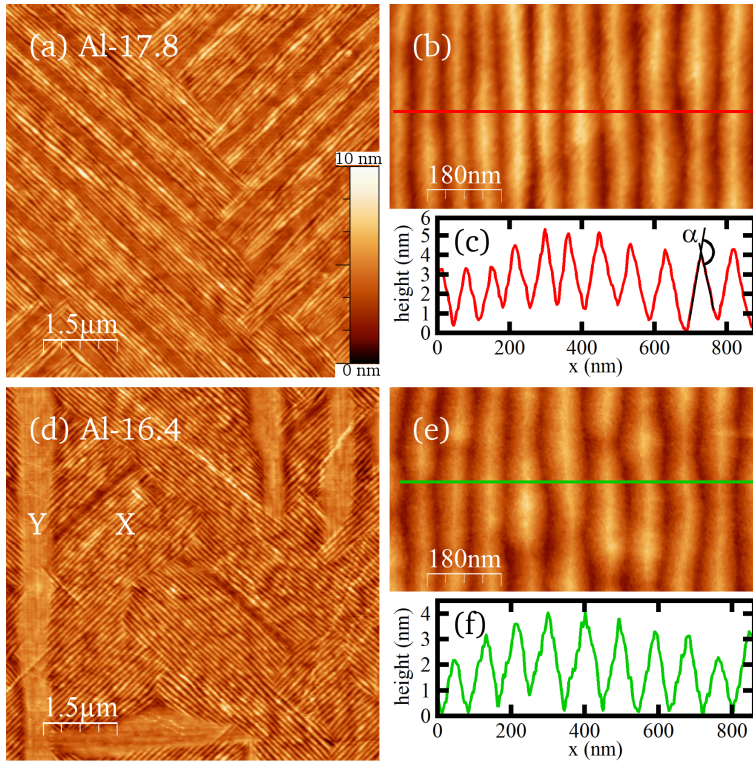
Figure 5.3. AFM micrographs and height profiles of Al-17.8 (a)–(c) and Al-16.4 (d)–(f). The picture margins of (a) and (d) are parallel to the substrate edges. The letters A and B label the two topography types found for Al-16.4. (b) and (e) show 45° rotated close-ups of the nanostructure and show the trace of the corresponding height profile, shown in (c) and (f), respectively.

buffer layer at 61° are also visible. The weak reflection marked by an asterisk is present in all films but could not be indexed unequivocally. It probably belongs to a binary impurity phase.

The films Al-17.8 and Al-16.4 which are mainly martensitic at room temperature allow for detailed investigation of the martensitic phase. For this purpose, firstly the surface morphology of the films is analyzed by AFM which helps to identify the microstructures occurring in the film. The micrographs for Al-17.8 and Al-16.4 are shown in Fig. 5.3. The surface of Al-17.8 indicates an austenite/martensite mixed phase. About 80 % of the surface shows a typical martensitic microstructure with traces inclined by 45° to the

substrate edges, which is also seen for epitaxial Ni-Mn-Ga thin films.[90] The periodicity of the variant traces is 83 nm. The flat ribbons parallel to the twinning traces belong to the austenite phase.[91] This is in accordance with the XRD measurements of this film and confirms a mixed state at RT for Al-17.8 (Fig. 5.2). The topography of the film originates from the twinning periodicity and the twinning angles of the variants involved. Thus, the surface angle α can be used to determine the twin structure involved.[91] From Fig. 5.3(c), $\alpha = 11°$ is determined and the structure can be identified using the relation $c/a = \tan(45° - \alpha/2)$, which equals $c/a = 0.84$ for Al-17.8. The structure is comparable to that of martensitic epitaxial Ni-Mn-Ga films.[90, 91]

The AFM micrograph of the completely martensitic film Al-16.4 in Fig. 5.3(d) reveals two types of martensitic microstructure which are described by Niemann as type X and type Y.[19] Both microstructures are typical of 14M martensite. They differ by the orientation of the 14M unit cell which exhibits predominantly in-plane b_{14M}-axis orientation for type X and out-of-plane b_{14M}-axis for type Y. Type X reveals traces inclined by 45° with a periodicity of 88 nm, and type Y is almost flat and oriented parallel to the substrate edges. Therefore, type X is also the dominating microstructure of Al-17.8 (Fig. 5.3(a)). From the topography of type X we can extract $\alpha = 10°$ leading to $c/a = 0.84$. The type Y microstructure shows only shallow surface angles of about 1° because the a–c twinning angle lies in the film plane for this structure.

For a detailed structural description of substrate constrained 14M films, the reader is referred to the recent doctoral thesis by R. Niemann.[19]

In order to determine all relevant lattice parameters of the martensite by XRD, it has to be considered that the martensitic lattice planes are tilted by small angles away from the lattice vectors of the austenite in order to fulfill the twinning equation and habit plane equation (Eqs. 2.21 and 2.22). These tilts make it necessary to adjust the sample alignment in the XRD system. This was achieved by measuring XRD patterns under certain ω offset combined with a specific in-plane sample orientation on the stage to be achieved with either $[010]_{\mathrm{MgO}}$ or $[\bar{1}10]_{\mathrm{MgO}}$ parallel to the direct beam. The ω offset is then comparable to a tilt of the sample around the $[100]_{\mathrm{MgO}}$ or $[110]_{\mathrm{MgO}}$ direction (see Sec. 3.3).

The results are depicted in Fig. 5.4 and the peak positions allow for identification of the phase as a mixture of modulated 14M and tetragonal non-
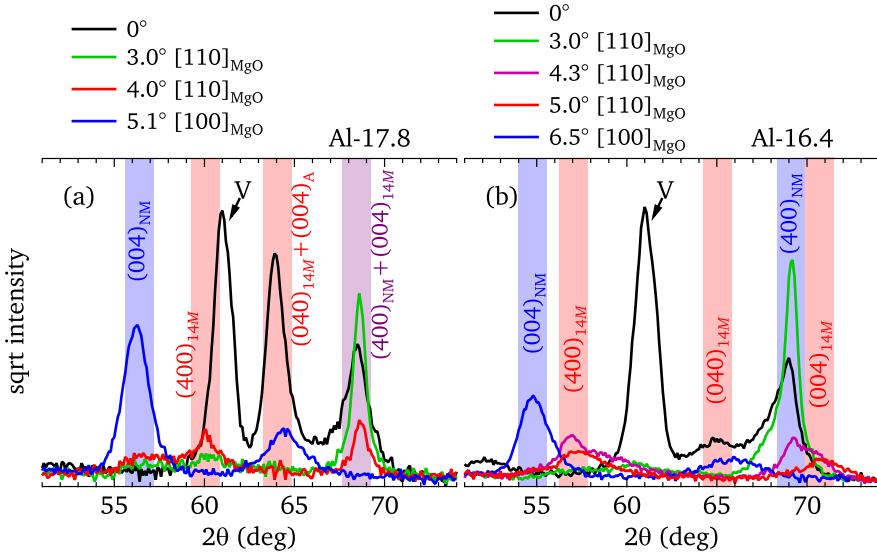
Figure 5.4. XRD patterns at different tilt angles of the MgO substrate around its [110] and [100] direction for (a) Al-17.8 and (b) Al-16.4.

modulated (NM) martensite. The lattice constants extracted from these XRD patterns are listed in Tab. 5.2. From the XRD measurements the c_{14M}/a_{14M} ratios are determined to 0.89 for Al-17.8 and 0.82 for Al-16.4, which fits in well with values determined from the AFM height profiles. Satellite peaks which appear for modulated phases between two fundamental peaks could not be measured for our films because of the low intensity of the fundamental peaks of the 14*M* structure. Nevertheless the occurring peaks are indexed by means of the 14*M* structure because the lattice parameters obtained fit in well with literature values for similar materials (see Tab. 5.2).

The largest reflexes in the XRD pattern are indexed by means of NM martensite. These larger NM variants form from the building blocks of the 14*M* martensite by twin coarsening as seen in Fig. 2.7 which enlarges the variants but conserves their crystallographic orientation. These large variants have a great enough coherence length for X-ray diffraction and by measuring their orientation it is possible to relate them to 14*M* martensite. In what follows, it will be shown that the observed 14*M* phase is an adaptive phase constructed from tetragonal building blocks in $(5\bar{2})_2$ periodicity in order to

Table 5.2. Lattice parameters of selected films first given in Heusler notation for comparison with epitaxial Heusler thin films from other studies and then in bct notation for comparison with bulk Ni-Mn-Al. All lattice constants are given in Å. β is the monoclinic angle and given in degrees.

sample	a_{NM}	c_{NM}	$(c/a)_{NM}$	a_{14M}	a_A, b_{14M}	c_{14M}	$(c/a)_{14M}$	a_{14M}^{bct}	b_{14M}^{bct}	c_{14M}^{bct}	β
Al-19.1					5.84						
Al-18.4					5.84						
Al-17.8	5.47	6.55	1.20	6.17	5.83	5.47	0.89	4.27	29.5	2.74	94.4
Al-16.4	5.43	6.70	1.23	6.47	5.75	5.32	0.82	4.31	29.7	2.72	95.2
1000 nm	5.46	6.58	1.21	6.14	5.81	5.46	0.89	4.27	29.5	2.73	94.6
1000 nm*	5.44	6.66	1.22		5.80						
Ni-Co-Mn-In[14]	5.48	6.88	1.26	6.33	5.94	5.56	0.88				
Ni-Mn-Ga[18]	5.42	6.65	1.23	6.18	5.78	5.62	0.91				
Ni$_{50}$Mn$_{34}$Al$_{16}$[83]	5.42	6.70	1.24					4.31	29.6	2.71	94.5
Ni$_{45}$Mn$_{40}$Al$_{15}$[83]								4.34	29.7	2.71	94.7
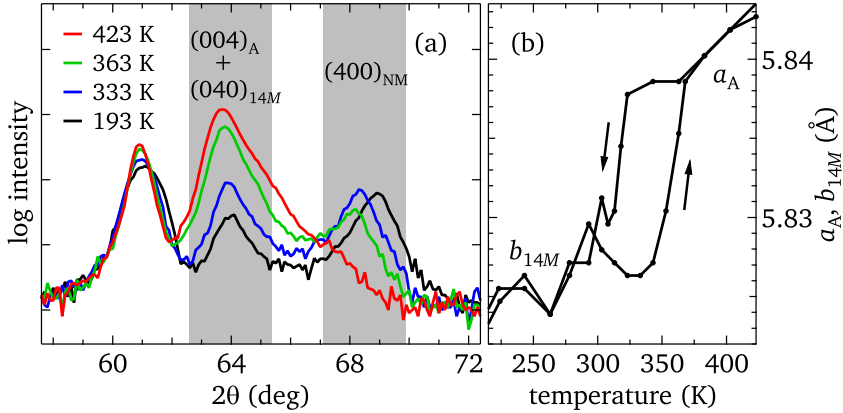
Figure 5.5. (a) XRD patterns of Al-17.8 at different temperatures during heating at zero tilt of the substrate. (b) Temperature dependence of a_A and b_{14M}. The arrows indicate the direction of temperature change.

obtain an almost exact interface to the austenite and the MgO substrate.[18, 31, 92]

The concept of adaptive martensite implies the following relations between 14M, NM, and austenite (see Sec. 2.1.3): i) $b_{14M} = a_A$, ii) $c_{14M} = a_{NM}$, and iii) $a_{14M} = c_{NM} + a_{NM} - a_A$.[18]

The first condition is related to the peak at about 64°. In order to distinguish a_A from b_{14M} the temperature dependence of this lattice parameter is analyzed. For this purpose, XRD patterns were taken at different temperatures as shown in Fig. 5.5(a) for Al-17.8. Apart from the change of the peak intensities due to the martensitic transformation. Changes of the peak positions are also visible. The lattice constant related to the peak at about 64° is depicted in Fig. 5.5(b) and corresponds to a_A at high temperatures and b_{14M} below the martensitic transformation. The hysteresis in the temperature range of the martensitic transformation reveals a difference between a_A and b_{14M} of about 0.01 Å. However, here it cannot be excluded that at low temperatures a mixture of $(004)_A$ and $(040)_{14M}$ is still measured because a small fraction of austenite is most likely present close to the substrate even at low temperature. Moreover, from Fig. 5.4(a) it is evident that the $(040)_{14M}$ appears not only at zero tilt but also at 5.1° tilt around $[100]_{MgO}$ at a slightly different angle. This peak belongs to a small fraction of nearly out-of-plane

b_{14M} variants within the type X structure and shows a lattice constant that is larger by 0.04 Å.

The second relation seems to be exactly fulfilled for Al-17.8 since the $(400)_{NM}$ and $(004)_{14M}$ cannot be distinguished. For Al-16.4, however, those peaks can be distinguished and the lattice constants differ by 0.11 Å.

The third relation can easily be checked using the lattice parameters from Tab. 5.2 and fits also almost exactly. However, this analysis reveals slight differences between the ideal model of adaptive martensite and the measured unit cells and also slightly different lattice constants depending on the orientation of the unit cell. One reason for that can be an incommensurate 14M microstructure. The decisive parameter for that is the twinning periodicity $d_1/d_2 = (a_{NM} - a_A)/(a_A - c_{NM})$, which is $d_1/d_2 = 2/5 = 0.4$ for a commensurate 14M structure. The calculated values are 0.49 for Al-17.8 and 0.33 for Al-16.4, thus the microstructure is incommensurate. This results in a high density of stacking faults, which can be the reason why the mentioned relations i)-iii) are not exactly fulfilled. Another error source is the fact that the determined lattice parameters do not belong to one martensitic variant, instead the nearly out-of-plane lattice parameters of all present variant orientations were measured. Those can differ significantly from the in-plane lattice parameters due to different boundary conditions and stress caused by the substrate.[19, 93]

To relate 14M and NM variant orientations, Fig. 5.6 shows the pole figure measurements for the $(004)_{NM}$ and $(400)_{NM}$ peaks. You can see that the main reflections of the $(004)_{NM}$ peak are at $\varphi = 0°$, and $\psi \approx 5°$ and 6.5° for Al-17.8 and Al-16.4, respectively, where $\varphi = 0°$ is equivalent to the $[100]_{MgO}$ direction. So, the main reflections of the pole figures fit the tilt angles used for maximum peak intensity (cf. Fig. 5.4). The observed tilt angles, and thus the orientation of the NM unit cell, originate from the orientation of the NM cells inside the 14M unit cell and the orientation of the 14M unit cell with respect to the austenite. The tilt between 14M and austenite is $\gamma = 45° - \arctan(c_{14M}/a_{14M})$ using the approximation that the 14M unit cell is orthorhombic.[94] This results in $\gamma = 3.42°$ for Al-17.8 and $\gamma = 5.55°$ for Al-16.4 where γ describes a tilt of the 14M unit cell around b_{14M}.[18] The relevant NM unit cells inside the 14M cell are inclined by 3.31° and 3.93° around c_{14M} for Al-17.8 and Al-16.4, respectively. These tilt angles can be determined from the structure of the 14M unit cell by basic geometry as described in Kaufmann et al. [18]. Combining these two tilts
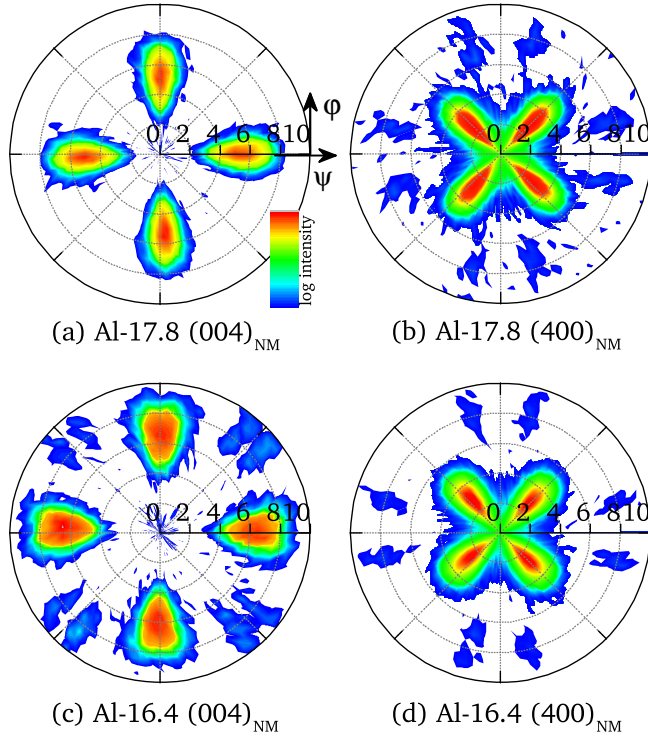
Figure 5.6. XRD pole figures of the $(004)_{NM}$ and $(400)_{NM}$ peaks for (a)–(b) Al-17.8 and (c)–(d) Al-16.4. The orientation of the NM variants matches the expected orientation of the building blocks of the 14*M* structure. $\varphi = 0°$ corresponds to $[100]_{MgO} = [110]_A$.

one can calculate the expected peak positions in the pole figures. The result is $\psi = 4.7°$, $\varphi = \pm 1°$ for Al-17.8 and $\psi = 6.8°$, $\varphi = \pm 10°$ for Al-16.4. The calculated ψ angles almost precisely fit to the measured angles for both films. The larger calculated φ for Al-16.4 also explains the broadening in φ direction of the measured major spots in the pole figure in Fig. 5.6(c), which look like superpositions of two peaks at slightly different φ. Due to 4-fold symmetry induced by the substrate, the corresponding reflections in the other quadrants of the pole figures are also explained. The minor reflections in the $(004)_{NM}$ pole figure of Al-16.4 at $\psi = 8°$ and $\varphi = 45° \pm 6.8°$ originate from type Y microstructure which is not observed in Al-17.8. ψ corresponds to the tilt of the smaller tetragonal twin within the 14*M* cell around c_{14M} to

$\psi = 7.99°$ and the distance between two neighboring spots in φ direction originates from the a_{14M}-c_{14M} twinning angle $\alpha = 11°$.

The main spots in the $(400)_{NM}/(004)_{14M}$ pole figures are at $\varphi = 45°$ and $\psi \approx 3°$ for both films. The orientation originates just from the tilt of the 14M cell in the type X structure around b_{14M} which is around 3°.[19] The positions of the minor reflections at $\psi = 7.5°$, $\varphi = \pm15°$ (calculated: $\psi = 7.7°$, $\varphi = \pm19°$) for Al-17.8, and $\psi = 8°$, $\varphi = \pm14°$ (calculated: $\psi = 9.7°$, $\varphi = \pm9.4°$) are calculated analogously to the $(004)_{NM}$ spots with the difference that here the 2-layer part of the 14M cell with tilts of 6.92° and 7.99° around c_{14M} for Al-17.8 and Al-16.4 is responsible. Deviations between calculated and measured positions of the spots in the pole figures can again originate from the uncertainty of the exact lattice constants since only nearly out-of-plane lattice constants are considered here, as stated above.

5.2.2 Freestanding films

Due to the omission of substrate clamping, freestanding films exhibit a waviness which effectively reduces texture of the specimen and hence the XRD peak intensity. In order to partly compensate for this, the structural characterization of freestanding films is based on a 1000 nm thick $Ni_{40.4}Co_{8.8}Mn_{33.4}Al_{17.4}$ film.

As is visible from Fig. 5.2, the substrate constrained film is martensitic at room temperature and the structure is adaptive 14M/NM with lattice parameters given in Tab. 5.2. The XRD pattern around the (004) peaks is shown in Fig. 5.7 (dashed lines), which reveals a similar structure as Al-17.8. After wet etching of the sacrificial V layer the freestanding film was kept on the MgO substrate in the same orientation as for the substrate bound film in order to retain the same crystal orientation. The XRD patterns of this 'as-released film' are shown in Fig. 5.7 as solid lines. Contrary to the substrate constrained film, the freestanding film exhibits only two detectable Bragg peaks in that range: $(400)_{NM}$ and $(004)_{NM}$. The absence of the small 14M peaks in this film can be explained by the waviness and therefore lower XRD intensity compared to the substrate constrained film.[2] Another possibility is the suppression of the 14M structure due to widening of the NM variants, which is energetically favorable after the loss of the substrate constraint. The

---

[2] The peak intensities of the freestanding film in Fig. 5.7 look comparable to those of the substrate constrained film because they were obtained by longer integration times.
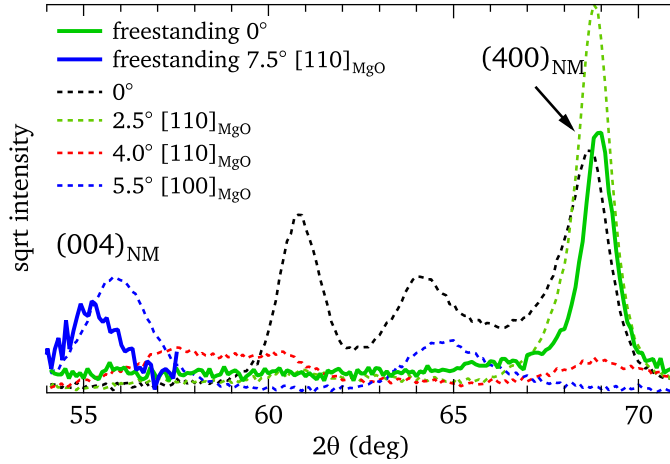
Figure 5.7. XRD patterns of the substrate constrained and freestanding (as-released) 1000 nm film. After releasing the film, only the $(004)_{NM}$ and $(400)_{NM}$ peaks remain.

$(040)_{14M}/(004)_A$ peak belonging partly to residual austenite is also gone due to the omission of the substrate clamping.

In order to study the real-space orientation of the martensitic variants, pole figure measurements were conducted for the $(004)_{NM}$ and $(400)_{NM}$ substrate-constrained and freestanding film. On substrate (Fig. 5.8(a) and 5.8(b)) the film exhibits the same orientation as the 200 nm film Al-17.8 (cf. Fig. 5.6(a) and 5.6(b)). Additionally, due to the larger ψ-range of the pole figures in Fig. 5.8, reflections from the in-plane lattice constants are visible when approaching $\psi = 90°$ at $\varphi = 45°$ which is equivalent to the $[100]_A$ direction. The range for the azimuth is only 180°, which is sufficient for the analysis due to the 4-fold symmetry of the pole figures that originates from the cubic austenite.

The pole figures of the as-released film are shown in Fig. 5.8(c) and 5.8(d). In the $(004)_{NM}$ pole figure (Fig. 5.8(c)) around $\psi = 54°$, $\varphi = 90°$ some intensity originating from the nearby $(222)_{NM}$ peak is visible due to the increased integration times for the freestanding films. Apart from that, the reflections around the origin are similar to those of the substrate constrained film and show that the variant orientation has not changed after the film was released. Also, around $\psi = 90°$ three reflections are still visible around $\varphi = 135°$, however, the central spot is considerably weaker than the outer
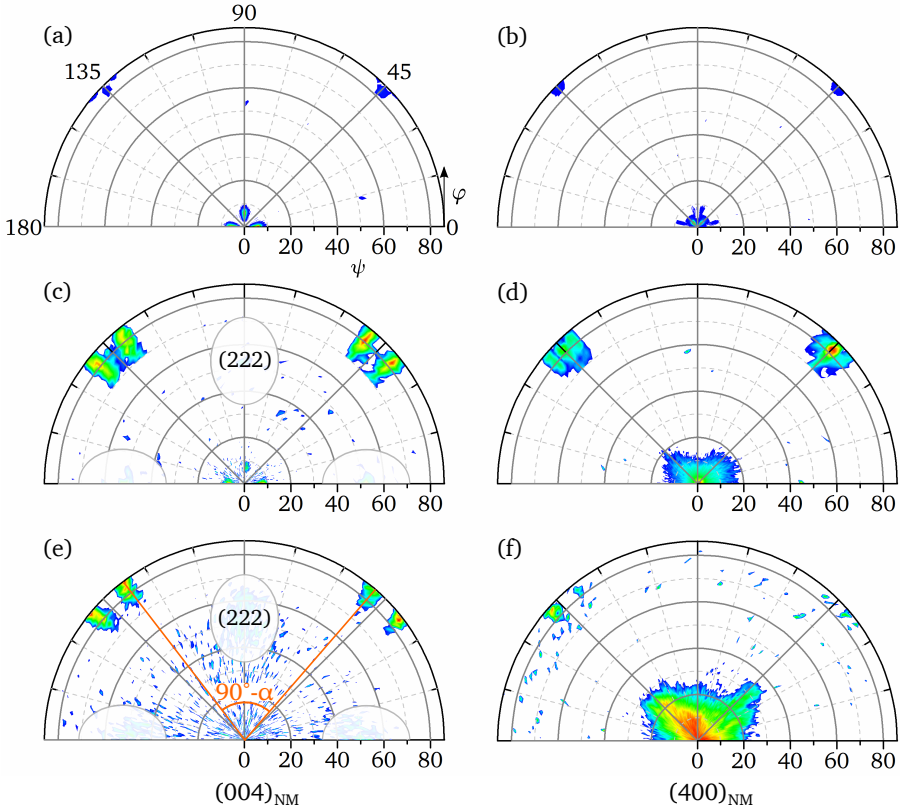
Figure 5.8. Pole figure plots of the $(004)_{NM}$ and $(400)_{NM}$ peaks for the substrate constrained film (a) and (b), the as-released film (c) and (d), and the annealed freestanding film (e) and (f). The positions of the spots and hence the orientation of the martensitic variant differ significantly between substrate constrained and freestanding films. The intensity in the $(004)_{NM}$ pole figures in (c) and (e) around $\psi = 54°, \varphi = 90°$ is an artifact originating from a nearby $(222)_{NM}$ peak.

ones at $\varphi = 135°\pm5.5°$ contrary to the substrate constrained film (Fig. 5.7(a)). Moreover, it is noted that for the freestanding films the spots are smeared out due to the waviness of the film and the features at 45° and 135° are not identical due to imperfect sample alignment. In the $(400)_{NM}$ pole figure (Fig. 5.8(d)), only one large spot with streaks in the direction of $\varphi = 45°$ is visible around the origin. Due to the waviness, the fine features visible for the substrate constrained film visible in Fig. 5.7(b) are not resolved. Around $\psi = 90°$ three spots are now visible at $\varphi = 135°$ and $\varphi = 135°\pm4.5°$

as opposed to only one spot for the substrate constrained film. So, the polefigures of the as-released film still show the same characteristics as the substrate constrained one; however, the spots from the in-plane lattice constants (i.e. at $\psi = 90°$) are significantly altered. This occurs on the one hand by widening of the spot size and by the appearance of additional spots, best seen in the $(004)_{NM}$ pole figure.

Moreover, it has to be considered that the as-released film not necessarily exhibits an energetically favorable structure because the material was already martensitic before releasing the film and is hence constrained in the microstructure induced by the substrate. In order to get the default microstructure of freestanding Ni-Co-Mn-Al films, the martensite was reset by annealing the freestanding film above the austenite finish temperature (annealing temperature $T_{ann} = 523\,\text{K}$) and subsequently cooling back to room temperature.

The pole figure measurements of the annealed film are depicted in Fig. 5.8(e) and 5.8(f) and reveal real space orientations of martensitic variants distinctly different from the as-released film and the substrate constrained film. It is striking that around the origin of Fig. 5.8(e) no intensity from $(004)_{NM}$ is found and also that the features around $\psi = 90°$ differ significantly from those measured for the as-released film. The absence of intensity around the origin indicates that out-of-plane orientation of the c-axis is suppressed in freestanding films. Also, it was stated above that the distinct features of the $(004)_{NM}$ pole figure around the origin are an indication of the adaptive 14*M*. However, in thin freestanding films there is no need for a 14*M* structure at the habit plane because two of the three tetragonal variants can form an exact interface to the austenite as explained in chapter 2.1.2. The third variant – that with an out-of-plane *c*-axis – cannot form an exact interface to the austenite and is therefore not present in the freestanding films.

Both, $(004)_{NM}$ and $(400)_{NM}$ generate two reflections near $\psi = 90°$, $\varphi = 45°$ instead of three for the as-released film. The central spots at $\varphi = 45°$ and 135° visible for the as-released film are therefore remnants from the 14*M* structure. The spot at the origin of the $(400)_{NM}$ pole figure is larger than that of the as-released film, which is caused by further increased waviness after the annealing process. The spot also pulls streaks in the $[100]_A$ direction, which therefore can be identified as the preferred orientation of the film's waviness.
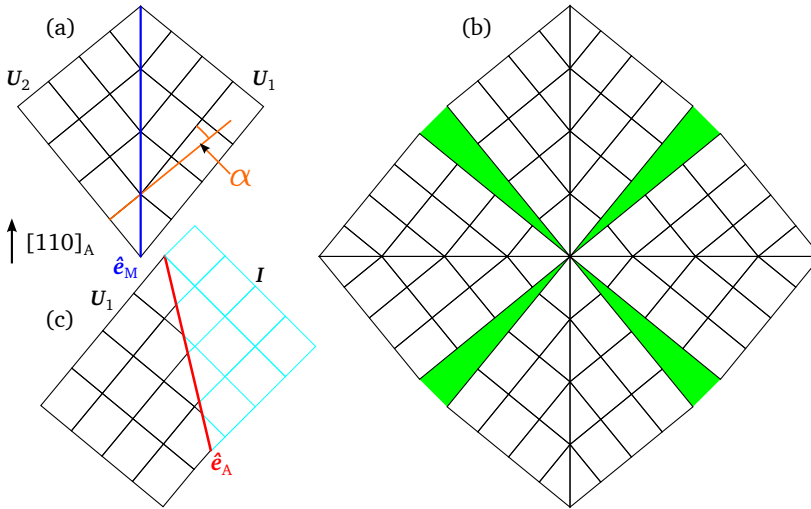
Figure 5.9. Sketch of the martensitic microstructure in freestanding films. (a) shows the two variants U_1 and U_2, and the twinning angle α which leads to the spots in the pole figures Fig. 5.8(e) and 5.8(f). (b) shows the misfit between twins with different twinning boundary orientations (green areas), and (c) shows the calculated habit plane orientation.

The pole figures of the freestanding film can be understood by solving the kinematic compatibility conditions. The result from Eq. 2.24 is that the invariant lines between two variants are in the $\langle 110 \rangle_A$ direction and the twinning angle is $\alpha_{U_1,U_2} = 11.5°$. One of the possible orientations is sketched in Fig. 5.9(a). This microstructure exactly fits the measured spots in the pole figures in Figs. 5.8(e) and 5.8(f) as indicated by the orange angle.

All four solutions of the twinning equation are found in the martensitic films because they are energetically equal. However, connecting these microstrucutres without deformations is not possible, as can be seen from the green areas in Fig. 5.9(c). Formation of these sketched gaps can also not easily be established because the lattice positions on opposite sides of the gap belong to the same atom, which means that the film must deform or rupture during the martensitic transformation. Advantageously, the geometry of freestanding thin films allows for macroscopic distortions since the film can freely bulge out of the film plane.

From the absence of out-of-plane c-axis orientation it follows directly that the film area increases by $a_{NM}c_{NM}/a_0^2 - 1 = 7.3\%$ compared to an austenitic
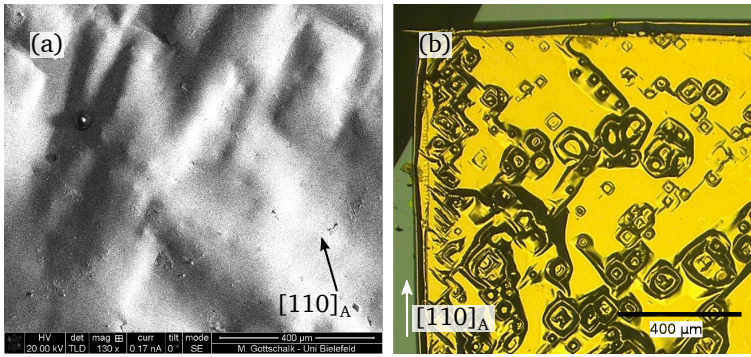
Figure 5.10. Bulging of martensitic freestanding films. (a) shows a SEM micrograph of the annealed 1000 nm film and (b) shows an optical micrograph of the partly martensitic freestanding film Al-19.1*.

film. This increase in area is also compensated by bulging up in out-of-plane direction.

Figure 5.10 shows a scanning electron microscopy (SEM) micrograph of the 1000 nm film in (a) and an optical micrograph of a partly martensitic 200 nm freestanding film of Al-19.1 in (b). The bulging of the films is clearly visible and the orientation of the bulged up tents and tunnels matches the orientation expected from the sketch in Fig. 5.9(b). The visible orientation of these tents and tunnels also explains the $[100]_A$ streaks pointing away from the origin in Fig. 5.8(f).

Further, it has to be stated that the visible $\langle 100 \rangle_A$ oriented ridges at the base of the bulges in Fig. 5.10 are not necessarily exact austenite-martensite interfaces. Instead, from Eq. 2.23 it follows that the invariant lines between austenite and martensite are described by the unit vectors $\hat{e}_{I,U_1} = (0.5236, \pm 0.8520, 0)$ for variant 1 and $\hat{e}_{I,U_2} = (\pm 0.8520, 0.5236, 0)$ for variant 2 in the austenite reference system and the inclination between $[100]_A$ and the Ith variant of martensite is $\alpha_{I,U_I} = 5.4°$. One possible austenite-martensite interface is sketched in Fig. 5.9(c) and it is inclined from the $[010]_A$ direction by $31.6°$. So, in order to resolve the real habit plane orientation further experiments employing, e.g., TEM will be conducted in future work.

5.2.3 Discussion

The key findings that the substrate constrained films exhibit 14*M* and NM, and the freestanding films NM martensite shows that the martensitic microstructure is not solely dependent on the composition of the material but also on boundary conditions and sample geometry. Structural data for bulk Ni-Co-Mn-Al were not available at the time of publication of this work, but for Ni-Mn-Al both 14*M* and NM martensites are recorded.[83] For structurally similar Ni-Mn-Ga compounds, epitaxial films also exhibit an adaptive 14*M* martensite, while bulk alloys of the same composition exhibit NM martensite.[18] Therefore, it can be concluded that the adaptive 14*M* martensite in epitaxial thin films is solely a result of the substrate constraint since it can form without macroscopic deformations of the film and it can easily form a habit plane with the austenite. In the freestanding film two of the NM variants can form an exact interface to the austenite and the film can also easily undergo macroscopic deformations and can therefore form larger NM variants in order to minimize twin boundary energy.

As a last point to be discussed here, it is striking that the tetragonality of the NM structure slightly enhances from $c/a = 1.205$ in the substrate constrained film to $c/a = 1.224$ in the freestanding film (cf. Tab. 5.2). However, calculations of the free energy vs. tetragonality of similar materials usually show a rather broad minimum. Therefore, it is plausible that c/a can be slightly varied depending on the boundary conditions in order to minimize the total energy of the system.[95, 96]

5.3 Magnetic properties

In order to analyze the metamagnetic characteristic of the martensitic transformation of Ni-Co-Mn-Al films, temperature dependent field cooling (FC) and field heating (FH) magnetization curves were measured and are shown in Fig. 5.11. A low applied field of 10 mT is chosen to generate only negligible field induced shift of the transformation temperatures and to avoid a contribution from the diamagnetic MgO. Al-19.1 (Fig. 5.11(a)) exhibits a monotonically decreasing magnetization with increasing temperature up to the austenite Curie temperature $T_C = 408 \, K$, which is determined by the inflection point of $M(T)$. The $M(T)$ curve shows no indication of a martensitic transformation.
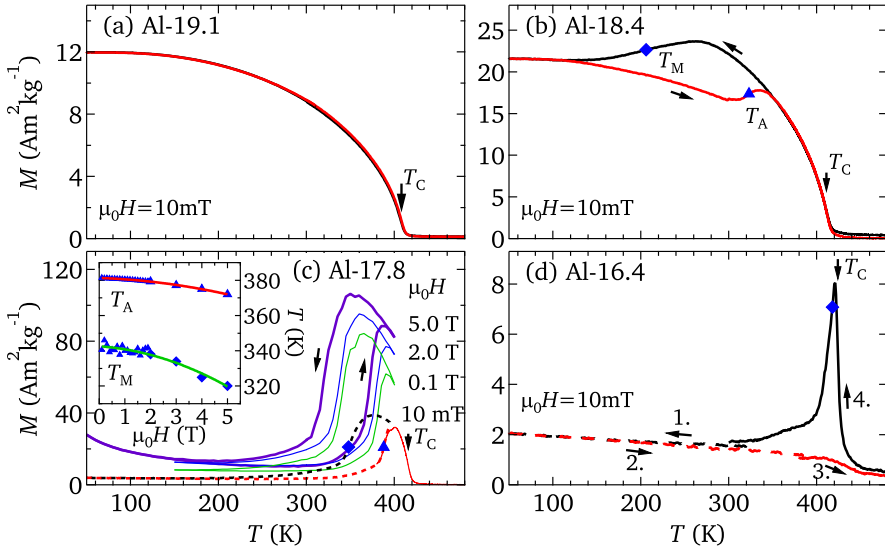
Figure 5.11. $M(T)$ curves of the substrate constrained films for field cooling (black) and field heating (red) at $\mu_0 H = 10\,\text{mT}$. Al-19.1 (a) shows no martensitic transformation and transformation of Al-18.4 (b) is incomplete resulting in a thermal hysteresis between 150 K and 330 K accompanied by only small changes of the magnetization. For Al-17.8 (c) $M(T)$ was measured at various fields up to 5 T in order to estimate the field induced shift of the transformation temperatures and the magnetocaloric properties. The blue squares and triangles depict T_M and T_A defined by the inflection points of the FC and FH curves. For each film $M(T)$ at $\mu_0 H = 10\,\text{mT}$ is presented as a combined curve where a cooling system and a heating system were employed, indicated by dashed and solid lines, respectively, in (c) and (d). The measurement sequence and direction are indicated by numbers and arrows in (d).

For Al-18.4 (Fig. 5.11(b)), the FC and FH curves envelop a thermal hysteresis between 150 K and 330 K which indicates a martensitic transformation and the inflection points in the transformation region define the forward (T_M) and reverse (T_A) transformation temperatures. However, the martensitic transformation of Al-18.4 is incomplete and residual austenite leads to high magnetization at low temperature. The large amount of residual austenite has been confirmed by low temperature XRD measurements (not shown).

For Al-17.8 (Fig. 5.11(b)), a distinct drop in the magnetization during cooling below 360 K is visible, which is due to the magnetostructural transformation from a strongly ferromagnetic austenite to a weakly magnetic

martensite. The difference in magnetization between martensite and austenite, ΔM, leads to a reduction of the transformation temperatures induced by the magnetic field. This follows from the magnetic Clausius-Clapeyron equation (Eq. 2.5)

$$\frac{\mathrm{d}T_{M/A}}{\mu_0 \mathrm{d}H} = -\frac{\Delta M}{\Delta S_{\mathrm{tot}}} \tag{5.1}$$

for two phases with entropy difference ΔS_{tot}. Hence, $M(T)$ curves at different applied fields up to 5 T were measured (Fig. 5.11(b)). For Al-17.8 the zero field transformation temperatures are $T_M = 348\,\mathrm{K}$ and $T_A = 389\,\mathrm{K}$.

The inset shows the dependence of T_M and T_A on the external field and to estimate the field induced change of the transformation temperature, $T_M(H)$ and $T_A(H)$ were fitted by a quadratic polynomial. From this,

$$\frac{\mathrm{d}T_M}{\mu_0 \mathrm{d}H} = -1(1)\,\tfrac{\mathrm{K}}{\mathrm{T}} - \mu_0 H \cdot 1.4(2)\,\tfrac{\mathrm{K}}{\mathrm{T}^2} \quad \text{and} \quad \frac{\mathrm{d}T_A}{\mu_0 \mathrm{d}H} = -0.50(4)\,\tfrac{\mathrm{K}}{\mathrm{T}} - \mu_0 H \cdot 0.55(2)\,\tfrac{\mathrm{K}}{\mathrm{T}^2}$$

are obtained. For comparison, for bulk $Ni_{40}Co_{10}Mn_{33}Al_{17}$, $\mathrm{d}T_M/\mathrm{d}H \approx -6\,\mathrm{K/T}$ and $\mathrm{d}T_A/\mathrm{d}H \approx -3.6\,\mathrm{K/T}$ can be estimated from Kainuma et al. [81] between 0.05 and 7.0 T ($T_M = 335\,\mathrm{K}$, $T_A = 361\,\mathrm{K}$, $T_C = 428\,\mathrm{K}$). If the above fits are averaged between 0 and 7 T, (i.e. evaluated at 3.5 T) $\mathrm{d}T_M/\mathrm{d}H(3.5\,\mathrm{T}) = -6(1)\,\mathrm{K/T}$ and $\mathrm{d}T_A/\mathrm{d}H(3.5\,\mathrm{T}) = -2.4(6)\,\mathrm{K/T}$ are obtained. While our $\mathrm{d}T_M/\mathrm{d}H$ coincides with the bulk value, the reason for the lower values for $\mathrm{d}T_A/\mathrm{d}H$ in the investigated film can be explained by the smaller ΔM at the reverse transformation due to the higher transformation temperatures and the resulting vicinity of T_A and T_C. Moreover, with decreasing $T_C - T_A$ it is also reported that the entropy difference ΔS_{tot} between austenite and martensite increases and thus $\mathrm{d}T_A/\mathrm{d}H$ decreases (cf. Eq. 5.1]).[97] The observed increase in magnetization below 100 K at 5 T is due to paramagnetic impurities in the MgO substrate. Since this film, Al-17.8, exhibits transformation temperatures close to room temperature combined with a large ΔM it is chosen for further magnetocaloric analysis discussed in Sec. 5.4.

It has to be noted that there is no physical model behind the polynomial fit and it is solely done in order to estimate the field dependent $\mathrm{d}T_{M/A}/\mathrm{d}H$, which is impractical directly from the rather noisy data.

Figure 5.11(d) shows the magnetization of Al-16.4. The FC curve depicts one sharp peak between T_M and the close-by T_C. In the FH curve, T_A is not visible in the magnetization because the reverse transformation occurs above
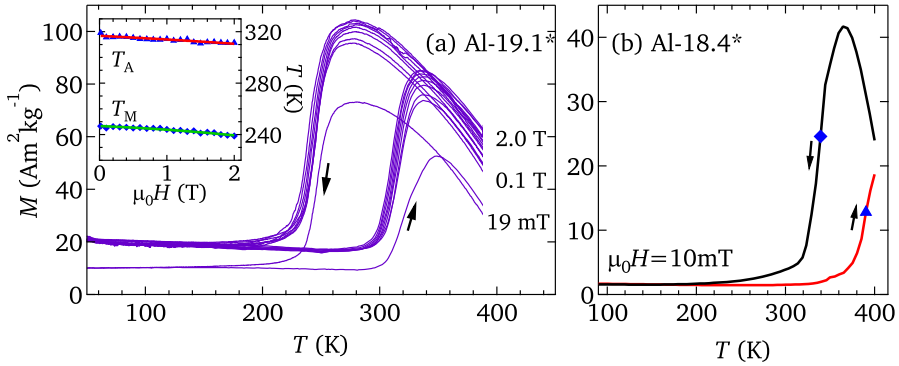
Figure 5.12. $M(T)$ curves of the freestanding films Al-19.1* (a) and Al-18.4* (b). For Al-19.1 several curves up to 2.0 T are measured in order to determine the field dependence of T_A and T_M, which is shown in the inset.

T_C. The FC and FH curves for Al-16.4 are combined from a high temperature ($T > 300$ K) and a low temperature ($T < 400$ K) measurement in order to cover the complete transformation range.[3]

Table 5.1 lists the Curie temperatures and martensitic transformation temperatures for all investigated films. As observed for other Ni-Mn-based Heusler alloys T_M is strongly dependent on the composition and increases with the valence electron concentration.[3] T_C shows a slight composition dependence, which can be explained by different Mn and Co concentrations. Both elements are known to increase T_C with increasing concentration, which is in agreement with our results (Table 5.1). [98–100]

For clarity, the freestanding films are marked by an asterisk. Figure 5.12 shows the isofield magnetization measurements of the freestanding films Al-19.1* and Al-18.4*. Both films exhibit a pronounced martensitic transformation, which is contrary to the behavior of the corresponding substrate constrained films that transform either only partially (Fig. 5.11(b)) or not at all (Fig. 5.11(a)). Additionally, the transformation temperatures of Al-18.4* are shifted substantially upwards after the film has been released, which is elucidated in detail in Sec. 5.5. Since for Al-19.1* the martensitic trans-

---

[3]In fact, all $M(T)$ curves which go beyond 400 K are combined in this way, but the measurement sequence and the way the final curve is put together is only important if the hysteresis is not closed below 400 K.
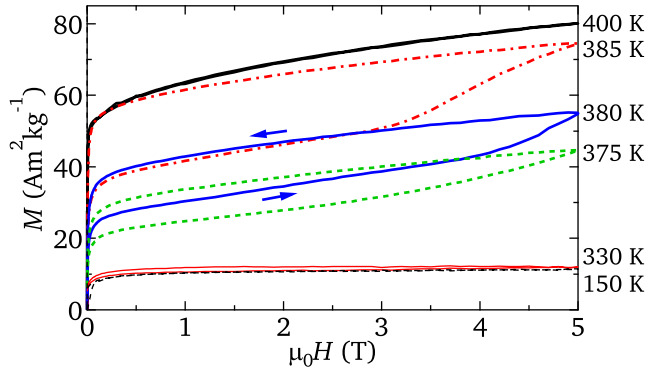
Figure 5.13. Isothermal magnetization measurements of Al-17.8 at different temperatures. Prior to each measurement the specimen was cooled to 150 K. Around T_A the magnetization shows significant hysteresis due to an irreversible field induced reverse transformation. The arrows indicate the direction of field change.

formation is close to room temperature with a large magnetization change ΔM, several isofield curves up to 2 T are measured to estimate the field induced shift of the transformation temperatures and the entropy change (see below in Sec. 5.4). In analogy to the substrate constrained film Al-17.8, the transformation temperatures shown in the inset of Fig. 5.12(a) were fitted by a quadratic polynomial which results in

$$\frac{\mathrm{d}T_\mathrm{M}}{\mu_0 \mathrm{d}H} = -2.1(4)\,\tfrac{\mathrm{K}}{\mathrm{T}} - \mu_0 H \cdot 1.5(2)\,\tfrac{\mathrm{K}}{\mathrm{T}^2} \quad \text{and} \quad \frac{\mathrm{d}T_\mathrm{A}}{\mu_0 \mathrm{d}H} = -2.6(3)\,\tfrac{\mathrm{K}}{\mathrm{T}} - \mu_0 H \cdot 0.5(9)\,\tfrac{\mathrm{K}}{\mathrm{T}^2}.$$

The comparison of the freestanding film Al-19.1* and the substrate constrained film Al-17.3 will be done in the following section.

5.4 Magnetocaloric properties

The following analysis of the field induced reverse transformation and magnetocaloric properties is focused on the substrate constrained film Al-17.8 and the freestanding film Al-19.1*, since they exhibit the largest ΔM, which is the driving force for field induced reverse transformation. Also, martensitic transformation occurs close to room temperature, which is desirable for many magnetocaloric applications.

Figure 5.13 shows $M(H)_T$ isotherms at selected temperatures, each measured after undercooling the specimen to 150 K in order to assure well-defined starting conditions. In the martensitic phase (150 K) the magnetization saturates below 1 T whereas in the austenite phase (400 K) up to 5 T the magnetization does not saturate. The coercive field of the material is $H_c = 1$ mT at room temperature and thus the magnetic hysteresis caused thereby is negligible. However, at temperatures around T_A, the $M(H)_T$ curves show significant thermal hysteresis. During the initial increase of the external field beyond a critical value the slope of the $M(H)$ curve increases due to a field induced reverse transformation whereas under subsequent decreasing field the magnetization is consistently higher. During a second field loop the magnetization retraces the curve of decreasing field of the first loop (not shown). Hence, the field induced reverse transformation is irreversible at the applied field of 5 T, which is a consequence of the thermal hysteresis seen in Fig. 5.11(c).

In order to determine the entropy change $\Delta S(T, \Delta H)$ caused by the field induced reverse transformation, FC and FH $M(T)_H$ have been measured for Al-17.8 and Al-19.1* at external fields of 0.1 T to 2.0 T in steps of 0.1 T, and additionally for Al-17.8 at 3 T, 4 T, and 5 T. Selected curves are shown in Figs. 5.11(c) and 5.12(a). The entropy change induced by a change of an applied field ΔH (from 0 to H_{max}) can be estimated by numerical evaluation of the integrated Maxwell relation, Eq. 2.33, or

$$\Delta S_m(T, H_{max}) = \mu_0 \int_0^{H_{max}} \left(\frac{\partial M(T, H)}{\partial T} \right)_H dH. \tag{5.2}$$

Figure 5.14 reveals ΔS_m for different applied fields. For Al-17.8, large values of 17.5 J kg^{-1}K^{-1} (FH) and 13.2 J kg^{-1}K^{-1} (FC) at a field change of $\mu_0 \Delta H = 5$ T are obtained. For comparison, Gd shows $\Delta S = -11$ J kg^{-1}K^{-1} for $\mu_0 \Delta H = 5$ T.[101]

The field dependence of ΔS_m is plotted in Fig. 5.15(a). The most striking feature is the visible difference in $\Delta S_m(5\,\text{T})$ between FC and FH of Al-17.8, however, the discussion of this is postponed to a later paragraph in this chapter. Up to $H_{max} = 2$ T, ΔS_m is almost equal around 7.5 J/(kg K) for the substrate constrained and freestanding film. Only the entropy change calculated from the FH curves of Al-19.1* is lower. This difference is due to the slight asymmetry of the hysteresis of the corresponding $M(T)$ curves visible in Fig. 5.12: $|\partial M/\partial T|$ is slightly larger for the FC branch than for the FH branch
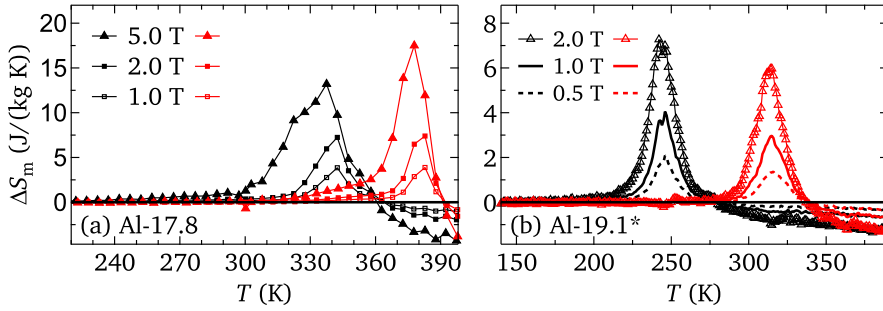
Figure 5.14. Entropy change of Al-17.8 (a) and Al-19.1* (b) calculated from FC (black) and FH (red) $M(T)$ curves (Fig. 5.11(b),Fig. 5.12(a)) using Eq. 5.2 for selected magnetic field changes.

and application of Eq. 5.2 results in decreased ΔS_{m}. Such an asymmetry was also found in epitaxial Ni-Co-Mn-Ga thin films where it is attributed to different nucleation barriers for the forward and reverse transformation.[102] It is more difficult to form a martensitic nucleus in a well-ordered austenitic single crystal due to the lack of nucleation centers. The martensite, however, is highly disordered, which anticipates the nucleation. Thus, the forward transformation occurs only after some undercooling, but then more rapidly than the reverse transformation, which occurs gradually. For the substrate constrained film, this kind of asymmetry is not present. However, it is visible from the XRD patterns in Fig. 5.5 that the martensite peak does not vanish completely even at high temperatures. These residual martensitic nuclei can grow as soon as the temperature falls below the martensite start temperature and thus, forward and reverse transformation have similar energy barriers.

For most of the other magnetocaloric Heusler compound thin films it is observed that the temperature range of the martensitic transformation is increased as compared to bulk, which results in broadening and flattening of the ΔS_{m} peak corresponding to the martensitic transformation. For example epitaxial Ni-Co-Mn-In films only show $\Delta S = 5\,\mathrm{J\,kg^{-1}K^{-1}}$ for $\mu_0\Delta H = 6\,\mathrm{T}$.[14] This broadening effect is less pronounced in Ni-Mn-Sn films[66] and the present Ni-Co-Mn-Al films. The reasons for the increase of the transformation range have not yet been ascertained, but size effects, substrate clamping, and phase compatibility between martensite and austenite affect the characteristics of the martensitic transformation in thin films.[10, 66] The heat
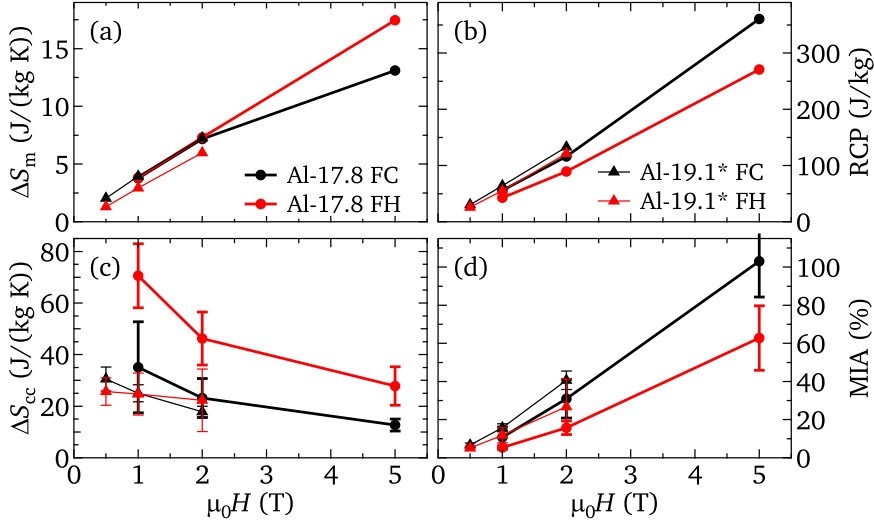
Figure 5.15. The magnetocaloric potential of Ni-Co-Mn-Al films. The field induced entropy change, ΔS_{m}, (Eq. 5.2) and the corresponding RCP (Eq. 5.3) are depicted in (a) and (b), respectively. (c) shows the total entropy difference between austenite and martensite, ΔS_{cc} (Eq. 2.5). The MIA $= \Delta S_{\mathrm{m}}/\Delta S_{\mathrm{cc}}$ is plotted in (d).

treatment and thus the crystallization process during the preparation of thin films should also be considered as it is completely different to bulk and can result in, e.g., substantial composition gradients.

Thus, as an appropriate measure to compare the magnetocaloric potential of bulk and thin film material, the relative cooling power

$$\mathrm{RCP} = \Delta S_{\mathrm{m}}^{\mathrm{max}} \delta T_{\mathrm{FWHM}} \qquad (5.3)$$

is introduced, where $\Delta S_{\mathrm{m}}^{\mathrm{max}}$ is the amplitude and δT_{FWHM} the full width at half maximum of the corresponding peak. For the calculation we did not consider any losses due to hysteresis effects of the material which reduce the cooling efficiency under field cycling as suggested by Guillou et al. [103] and the RCP is primarily used as a measure for the area of the ΔS_{m} peak. However, it has to be stated that due to the thermal hysteresis the inverse MCE in the present material is irreversible using moderate magnetic fields without manually adjusting the temperature after each field cycle. Before the inverse MCE of the material can be utilized in an efficient cooling system

it is necessary to optimize the thermal hysteresis. This was, for example, successfully done by Srivastava et al. by tuning the composition of Ni-Co-Mn-Sn in order to maximize the crystallographic compatibility between martensite and austenite.[104] Another approach to reduce or eliminate thermal hysteresis is the implementation of structural or chemical defects by, e.g., thermal treatment, substitution or doping with further atomic species, introduction of vacancies, or ion irradiation.[103, 105–107] For the Ni-Co-Mn-Al system, minimization of the hysteresis will be pursued in a future project.

The field dependencies of the RCP for Al-17.8 and Al-19.1* are depicted in Fig. 5.15(b). For both films the RCP calculated from FC curves is slightly larger than that from FH curves. This is due to the presence of the counter-acting conventional magnetocaloric effect close to T_C, which narrows the FH ΔS_m peak. This cMCE contribution is visible as a negative ΔS_m in the high temperature region of Fig. 5.14(a) and 5.14(b).

One of the most promising magnetocaloric Heusler compounds is Ni-Co-Mn-In, which shows $19\,\mathrm{J\,kg^{-1}K^{-1}}$ at $\mu_0\Delta H = 1.9\,\mathrm{T}$ for bulk $Ni_{45.7}Co_5Mn_{36.3}In_{13}$. Moreover, from Liu et al. [108] one can estimate the RCP of Ni-Co-Mn-In to be $135\,\mathrm{J\,kg^{-1}}$ for $\mu_0\Delta H = 1.9\,\mathrm{T}$ which is similar to our results for $\mu_0\Delta H = 2\,\mathrm{T}$. For comparison, Gd shows $RCP = 660\,\mathrm{J\,kg^{-1}}$ for $\mu_0\Delta H = 5\,\mathrm{T}$ (estimated from Dan'kov et al. [101]). Also, the RCP of Ni-Co-Mn-Al is comparable to other promising thin film systems like FeRh[109], MnAs[107] or $La_{0.8}Ca_{0.2}MnO_3$[110].

To further discuss the magnetocaloric properties, the full entropy change between austenite and martensite ΔS_{tot} is evaluated using the Clausius-Clapeyron relation (Eq. 5.1) and denoted as ΔS_{cc}. The values for $\mathrm{d}T_{M/A}/\mathrm{d}H$ are calculated from the polynomial fits given in the previous section. The magnetization difference ΔM between martensite and austenite at the temperatures $T_M(H)$ and $T_A(H)$ is estimated from Figs. 5.11(c) and 5.12(a). The values obtained for ΔS_{cc} are plotted in Fig. 5.15(c), where the error bars have been calculated from the uncertainties of the fit coefficients of $\mathrm{d}T_{M/A}/\mathrm{d}H$ and a $5\,\%$ error in the estimate of ΔM.

All curves reveal a decreasing entropy difference with increasing field. The reason for this is that the negative magnetic contribution to the entropy of the austenite increases with increasing field and increasing magnetization as is clear from Eq. 2.11. Moreover, since the transformation temperatures

shift substantially with increasing field, a change of the lattice contribution to the entropy is likely.

By comparing the field induced entropy change ΔS_m and the total entropy change ΔS_cc it is possible to estimate the maximum amount of material transformed due to a given magnetic field. This magnitude, the *magnetically induced austenite*, MIA $= \Delta S_\mathrm{m}^\mathrm{max} / \Delta S_\mathrm{cc}$ is plotted in Fig. 5.15(d). As expected the magnitude increases with increasing applied field. However, it is visible for the FC curve of Al-17.8 that the MIA reaches 100 % at 5 T, which means that a field change of $\mu_0 \Delta H = 5\,\mathrm{T}$ is enough for a complete phase transformation of the material because ΔS_cc is the upper limit for ΔS_m. This causes the saturation of the FC ΔS_m curve seen in Fig. 5.15(a) and accordingly the broadening of the peak in Fig. 5.11(a). Hence, further increase of the applied field will not increase $\Delta S_\mathrm{m}^\mathrm{max}$ but it will lead to a widening of the ΔS_m peak (Fig. 5.14(a)) to lower temperature due to the drop of T_M and hereby the RCP increases. The field dependence of the RCP is therefore not significantly affected by the saturation of FC $\Delta S_\mathrm{m}^\mathrm{max}$ and the FC RCP stays above the FH RCP as seen in Fig. 5.15(b).

5.5 Phase diagram

In this section, we put all zero field transformation temperatures available into a structural and magnetic phase diagram. So, for those films where the transformation temperatures could not be identified by $M(T)$ measurements (see Fig. 5.11 and Fig. 5.12), temperature dependent XRD measurements were performed and are presented in Fig. 5.16 as normalized integrated intensity of the $(004)_\mathrm{A}$ peak over temperature. The resulting phase diagram with all magnetic and structural transformation temperatures between 200 K and 450 K as a function of the valence electron concentration (e/a) is presented in Fig. 5.17. Clearly, T_M and T_A decrease with decreasing e/a ratio, as expected for Ni-Mn-based Heusler compounds.[3] Furthermore, it is visible that the martensitic transformation shifts to higher temperature when the film is released from the substrate and the substrate constrained films with low e/a ratio show no or only incomplete martensitic transformations. There are several influences directly or indirectly caused by the substrate that may hinder the martensitic transformation and lead to these observations.
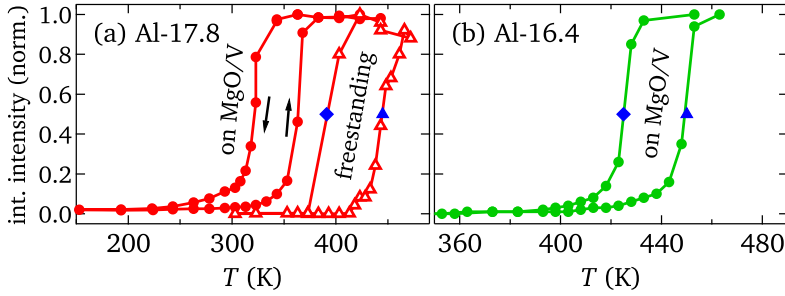
Figure 5.16. Temperature dependence of the $(004)_A$ XRD peak for substrate constrained (circles) and freestanding (open triangles) Al-17.8 (a) and substrate constrained Al-16.4 (b). XRD measurements allow for the determination of the transformation temperatures above T_C. T_M and T_A are indicated as blue squares and triangles, respectively.

Strain For martensitic materials in general the transformation temperatures are known to show a strong strain dependence because the crystallographic anisotropy in the martensite phase allows for the material to rearrange the variants in order to minimize the stress. Since this is not possible for the high symmetry austenite state, the application of uniaxial strain favors the martensite. This is contrary to the assumption of a strain induced by the substrate.

The lattice mismatch between the V buffer and the Heusler film leads to epitaxial (biaxial) strain close to the V/Ni-Co-Mn-Al interface which is released in the unconstrained freestanding film. The equilibrium lattice constant of V is 3.03 Å which is close to the in-plane lattice constant of 3.00 Å (out of plane: 3.05 Å) as determined by XRD measurements. So, the V is only slightly strained by the underlying MgO substrate ($a_{MgO}/\sqrt{2} = 2.98$ Å). The austenite lattice constants of Al-19.1, Al-18.4, and Al-17.8 are almost identical and the lattice mismatch is 2.7 % for the former two and 2.9 % for the latter film (cf. Tabl. 5.2). In another experiment we deposited the Ni-Co-Mn-Al onto different substrate and buffer layer materials. It revealed that the transformation temperatures are not significantly changed on different substrate materials with up to 3 % lattice mismatch.[111] Therefore, the influence of epitaxial strain on the austenite lattice can be excluded as a source for the shift of transformation temperatures upon release of the film.
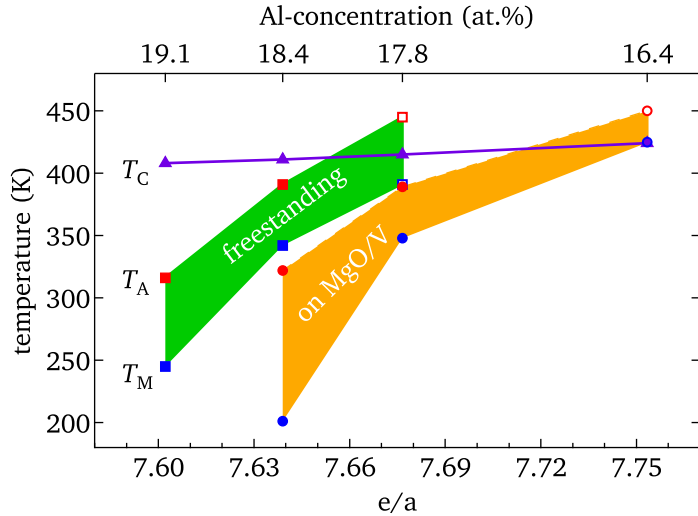
Figure 5.17. Structural and magnetic phase diagram of freestanding and substrate constrained Ni-Co-Mn-Al films. The transformation temperatures are shown as a function of the composition and the e/a ratio calculated from it. The Curie temperature depicted by purple triangles is extracted from $M(T)$ measurements of the substrate constrained films shown in Fig. 5.11. T_M and T_A are shown by blue and red symbols, respectively. The data points were obtained by $M(T)$ measurements (closed symbols) and XRD measurements (open symbols). The orange and green areas represent the transformation range of the substrate constrained and freestanding films, respectively.

Substrate clamping The presence of a cubic substrate or buffer layer prevents macroscopic geometrical changes of the material and leads to a certain amount of residual austenite at the interface even in the martensite phase. Also, as discussed in Sec. 5.2.3, the boundary condition at the habit plane leads to the formation of a finely twinned and adaptive 14*M* and NM martensite with many twin boundaries which raise the overall energy of the martensitic phase and thus, the martensite phase is stabilized only at lower temperature as compared to the freestanding films.

Size of the martensitic nucleus The relevant energy contributions for the nucleation of martensite are a volume term and a surface term which together define the size of a martensitic nucleus. The volume term is given by the difference in Gibbs free energy density between the two phases and

therefore increases with decreasing temperature. The interface energy is determined by the energy of the new habit planes enveloping the nucleus. For adaptive 14*M* martensite the martensitic nuclei are elongated and flat diamonds with habit planes inclined by few degrees from the $[011]_A$ direction and an aspect ratio of approximately 40 to 14 to 1 as shown by Niemann [19]. The maximum size is determined by one tip of the diamond touching the substrate because a larger nucleus requires a finitely extended interface with the substrate which is energetically vastly unfavorable.[19] Thus, the film thickness dictates the maximum size of a martensitic nucleus. The consequence is that with decreasing film thickness the nucleation requires more undercooling which shifts the transformation to lower temperature.[9, 72] The film thickness also determines the width of the martensitic variants which is seen on the film surface (cf. Fig. 5.3) since the nuclei grow mainly in length and not in width because they cannot form an interface with the substrate.

The freestanding films have two free interfaces and therefore, the condition of a maximum nucleus size does not apply here. The size of a martensitic nucleus is therefore much smaller for substrate constrained films than for freestanding films and the required undercooling for nucleation decreases the transformation temperatures.

Diestel et al. report similar transformation temperatures for substrate constrained and freestanding 3.84 μm thick Ni-Co-Mn-Ga films.[102] However, the authors do not provide a structural characterization, so it is not clear whether the freestanding films in that case also show a martensitic structure comparable to that found for Ni-Co-Mn-Al films. For substrate constrained films it is known from other publications of that group that Ni-Co-Mn-Ga and Ni-Co-Mn-Al are isostructural.[112] Furthermore, the film thickness dependence of the shift of the transformation temperatures in freestanding films has yet to be investigated, since in thicker substrate constrained films, the martensitic nuclei and variants grow and consequently the interface contribution decreases, which is expected to increase the transformation temperatures.

Kinetic arrest   For bulk Ni-Co-Mn-In and Ni-Co-Mn-Al with strongly ferromagnetic austenite it was found that if the transformation temperature is below the Curie temperature the total entropy difference between martensite

Figure 5.18. Total entropy change vs. difference between Curie and martensitic transformation temperatures at $\mu_0 H = 2\,\text{T}$. The entropy change related to the martensitic transformation decreases with $T_C - T_{M/A}$ due to the increase of the magnetic entropy.
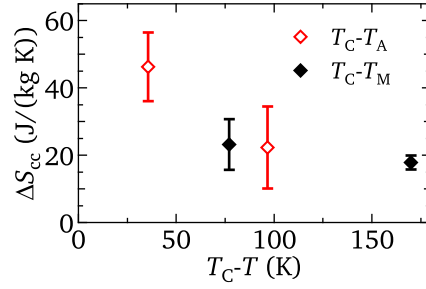
and austenite decreases with increasing $T_C - T_M$.[86, 97] This happens when the negative magnetic contribution is of the same order of magnitude as the positive lattice contribution. Thus, at temperatures well below T_C the undercooling needed for martensitic transformation increases until the transformation is entirely depleted. The connection between ΔS_{cc} and $T_C - T_M$ is shown in Fig. 5.18 for the transformation temperatures at $\mu_0 H = 2\,\text{T}$ of Al-17.8 and Al-19.1* from Fig. 5.15(c). Clearly, the entropy change decreases with decreasing transformation temperature. Therefore, it is plausible that if the transformation is shifted to even lower temperatures, it is depleted completely as seen for the substrate constrained Al-19.1. Similar temperature dependence of ΔS_{tot} is reported for bulk Ni-Co-Mn-Al alloys.[113] This temperature dependence also leads to the different field induced shifts for T_A and T_M and an increased structural hysteresis in $M(T)$ measurements at higher applied field.

A related effect is the reentrant martensitic transformation reported in certain off-stoichiometric $Co_2Cr(Ga,Si)$ Heusler alloys by Xu et al. [114] where at low temperatures the martensite transforms back to austenite. The key condition for this effect is a strongly ferromagnetic austenite and a non-magnetic martensite. The conventional martensitic transformation is then above the austenite Curie temperature between two non-magnetic phases and the reentrant transformation below T_C from non-magnetic martensite to ferromagnetic austenite during cooling. A reentrant martensitic transformation was not found in the investigated Ni-Co-Mn-Al alloys, however, our findings show a decreasing ΔS_{tot} for increasing $T_C - T_M$. Therefore, the kinetic arrest phenomenon is likely to be responsible for the suppression of the martensitic transformation of Al-19.1 and Al-18.4. Thus, in these films the substrate constraint leads to reduction of the transformation temperatures until the entropy difference between the two phases is too small to

enable a martensitic transformation. In the freestanding films the substrate constraint is released and the increased transformation temperatures allow for a martensitic transformation.

A last point for discussion is the influence of the substrate constant on the width of the thermal hysteresis. It is visible from Fig. 5.17 that the hysteresis width $\delta T_h = T_A - T_M$ significantly decreases for Al-18.4 and slightly increases for Al-17.8. For Al-18.4 the reason is clearly the kinetic arrest that significantly lowers T_M in the substrate constrained film and hence leads to very large δT_h. For Al-17.8, however, the transformation temperatures are too high for kinetic arrest to significantly influence the thermal hysteresis. For substrate constrained films exhibiting an adaptive 14M martensite, the hysteresis width is ascribed to the process of twin coarsening at a certain distance to the habit plane because the annihilation of twin boundaries represents an energy barrier.[90]. Since in freestanding films, single NM variants form a coherent habit plane, a twin coarsening process is not necessary. However, the martensitic transformation in freestanding films requires macroscopic plastic deformation of the film which in turn increases the hysteresis width and leads to a comparable hysteresis for freestanding and substrate constrained films.

5.6 Conclusions

We have studied the structure, magnetism, and magnetocaloric properties of epitaxial Ni-Co-Mn-Al thin films on MgO substrates. The martensitic structure of these films was determined to be a mixed phase consisting of adaptive 14M martensite and larger NM variants for substrate constrained films and solely NM martensite for freestanding films. Moreover, the variant orientation was found to change due to the different boundary conditions and ductility of freestanding films: The NM variants in the substrate constrained films are oriented in the same direction as the nanoscopic NM building blocks of the 14M structure noticeable from pole figure measurements of the NM reflections, while the freestanding films consist of in-plane oriented NM variants with exclusive out-of-plane a-axis.

We also found a bulk-like martensitic transformation and giant inverse magnetocaloric effect in Ni-Co-Mn-Al films with up to $\Delta S_m = 7.3\,\text{J/(kg K)}$ for both substrate constrained and freestanding films and with this Ni-Co-Mn-Al

qualifies as one of the most promising magnetocaloric thin film materials known so far. The entropy difference between austenite and martensite, ΔS_{cc}, decreases with increasing magnetic field which leads to saturation of the field induced entropy change and increasing $\mathrm{d}T_{M/A}/\mathrm{d}H$ at high field. The transformation temperatures increase when a film is released from the substrate, which was attributed to the absence of the need for a finely twinned martensite at the habit plane. The substrate also limits the size of a martensitic nucleus which also leads to higher interface energy that hinders the martensitic transformation. Moreover, it was found that the ΔS_{cc} decreases with decreasing transformation temperatures, which leads to kinetic arrest, and therefore some of the substrate constrained films do not exhibit a martensitic transformation, whereas their freestanding counterparts do.

The most striking problem that mitigates the applicability of Ni-Co-Mn-Al in magnetic cooling devices is the large structural hysteresis, which makes the effect irreversible at moderate magnetic fields. Therefore, the first challenge for future work will be to understand and reduce the structural hysteresis in this material.

Summary

In the prospect of examining shape memory Heusler alloy thin films for applications in spintronics and magnetocalorics, we investigated the potential of Ni-Mn-Sn films as pinning layers in magnetic tunnel junctions and Ni-Co-Mn-Al films for magnetic refrigeration. The underlying physical phenomenon for the first project is an intrinsic exchange bias effect caused by a cluster spin-glass state at low temperature, whereas for the second project the giant inverse magnetocaloric effect corresponding to the magnetostructural martensitic phase transformation is decisive.

We integrated a $Ni_{52}Mn_{34}Sn_{14}$ Heusler compound film on into an MgO (substrate)/Ni-Mn-Sn/CoFeB/MgO/CoFeB magnetic tunnel junction and have shown that the intrinsic exchange bias causes a shift on the switching field of the magnetic electrodes. From magnetization measurements on a separate MgO(substrate)/Ni-Mn-Sn sample (sample B) we know that the martensitic transformation in the film occurs at $T_{M} = 257$ K. Below 70 K an exchange bias effect is observed with H_{EB} up to 169 Oe at 10 K. Similar magnetization measurements on an MgO(substrate)/Ni-Mn-Sn/CoFeB/MgO/CoFeB specimen (sample A) have shown that the adjacent Ni-Mn-Sn/CoFeB layers exhibit common coercive fields and hence common H_{EB}, which, however, is reduced as compared to Ni-Mn-Sn alone due to the low H_c of CoFeB.

TMR measurements on nanofabricated MTJs (sample C) exhibit similar H_{EB} to that of sample A and therefore it was shown that Ni-Mn-Sn can act as a pinning layer in MTJs, however, the pinning mechanism is different from

that of common antiferromagnets (see Sec. 2.3). Here, the exchange bias originates solely in the Ni-Mn-Sn layer and due to the magnetic moment of Ni-Mn-Sn it is forced upon the adjacent CoFeB layer.

For the study of magnetocaloric Ni-Co-Mn-Al films we fabricated a series of films with different composition in order to obtain a set of different transformation temperatures. With this we compared the structural, magnetic and magnetocaloric properties of substrate constrained and freestanding films. The structural examination reveals an adaptive 14M martensite which coarsens into mesoscopic NM variants for substrate constrained films. Freestanding films exhibit only NM martensite with the peculiarity that the c-axis is exclusively in-plane oriented. Therefore, the martensite is not self-accommodating and a large misfit between the austenite and martensite film area is present. To compensate for this the film bulges out and as a consequence the martensitic film shows high waviness.

Magnetocaloric measurements were conducted on one substrate constrained film (Al-17.8) and one freestanding film (Al-19.1*) where different compositions were chosen because the martensitic transformation shifts to higher temperatures in freestanding films. The reason for this is that the boundary condition to the substrate demands a finely twinned martensite with high interface energy at the habit plane and it also limits the size of a martensitic nucleus which further leads to higher interface energy which hinders the martensitic transformation. Nevertheless, giant inverse magnetocaloric effects were found with up to $\Delta S_{\mathrm{m}} = 7.3\,\mathrm{J/(kg\,K)}$ for both substrate constrained and freestanding films. The entropy difference between austenite and martensite ΔS_{cc} was found to decrease with increasing magnetic field which leads to saturation of the field induced entropy change and increasing $\mathrm{d}T_{\mathrm{M/A}}/\mathrm{d}H$ at high field. Furthermore, ΔS_{cc} decreases with decreasing temperature which causes kinetic arrest and suppression of the martensitic transformation in films with low expected transformation temperature. This effect is also noticeable in the field dependence of the transformation temperatures. For both investigated films the lower T_{M} drops faster than T_{A} since the lower ΔS_{tot} between martensite and austenite at lower temperature accelerates the decrease of $T_{\mathrm{M/A}}$.

The most striking limitations that should be addressed in future work are the temperature dependence of the intrinsic EB in Ni-Mn-Sn and the structural hysteresis in Ni-Co-Mn-Al.

Outlook

In this chapter, in addition to the brief outlooks given at the end of the previous chapters, two separate topics are introduced that especially make use of substrate constrained or freestanding films. Specifically, these are the use of X-ray magnetic circular dichroism (XMCD) and energy-loss magnetic chiral dichroism (EMCD) for the element specific magnetic moments, and pump-probe spectroscopy to study the time scale of the martensitic transformation.

7.1 X-ray magnetic circular dichroism and energy-loss magnetic chiral dichroism

In order to understand the details of the metamagnetic phase transformation and the magnetic state of the martensite phase in magnetocaloric Heusler compounds one approach is to use element specific magnetic probes. X-ray magnetic circular dichroism measures the differential absorption of circularly polarized X-rays with different helicity near the absorption edges of the material and is a well established technique to study element specific magnetic moments.[115]

Figure 7.1 shows X-ray absorption spectroscopy (XAS) and XMCD spectra of Mn, Co, and Ni taken at the $L_{2,3}$ edges of the substrate constrained film Al-17.8 measured at the Advanced Light Source, Berkeley, beamline 4.0.2 in total electron yield mode. During measurement a magnetic field of ±0.5 T
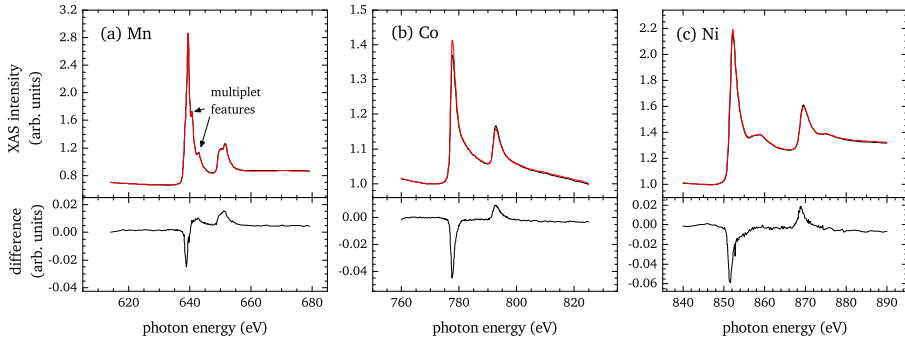
Figure 7.1. XAS (upper panel) and XMCD (lower panel) spectra of (a) Mn, (b) Co, and (c) Ni of Al-17.8 measured in total electron yield mode at 150 K. The Mn spectrum clearly shows fine structure features originating from surface oxide.
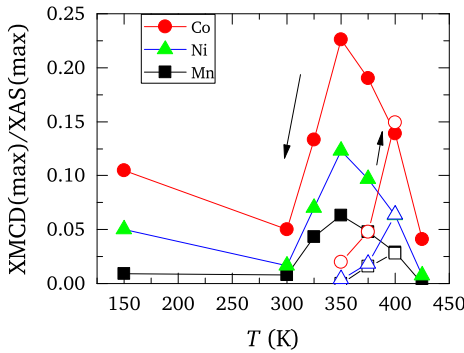
Figure 7.2. Element specific temperature dependence of the XMCD for cooling (filled symbols) and heating (open symbols). The XMCD signal is clearly correlated with $M(T)$ (cf. Fig. 5.11(c)) and reveals the martensitic transformation.

was applied and the spectra were taken in the martensite state at 150 K. In the Mn spectrum (Fig.7.1(a)), clear features originating from Mn multiplet are visible, which are an indicator of an oxidized surface. So the 2 nm MgO capping layer did not completely prevent surface oxidation of the Heusler layer. As a result a quantitative sum rule analysis of the XMCD spectra is not possible. The reasons for the oxidation may have been damage of the MgO capping caused by the martensitic transformation or humidity.

In Fig. 7.2 the XMCD signal amplitude is shown, which is an approximate measure for the difference in spin density of unoccupied states.[115] It is visible that a qualitative agreement with the $M(T)$ measurements exists and the martensitic transformation is revealed in the XMCD signal amplitude. However, although the Mn moment carries the largest magnetic moment,
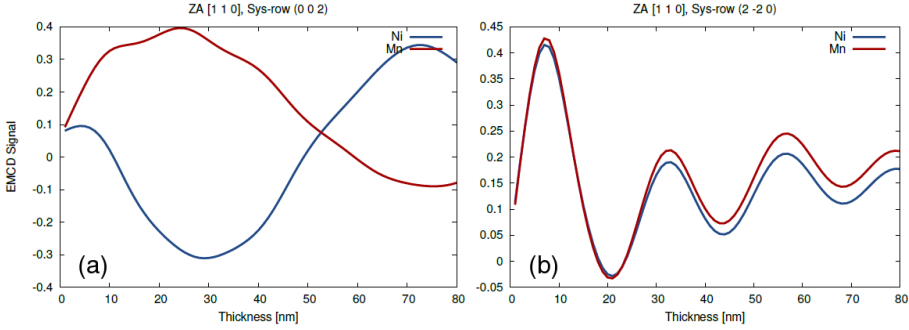
Figure 7.3. Simulated thickness dependence of the EMCD signal of Ni_2MnSn with [001] zone axis for (a) (200) and (b) (220) systematic row condition. Taken from Hetaba [116].

the XMCD signal is the smallest. This is probably caused by the oxidation which is most pronounced in the Mn XAS. So, in order to obtain the element specific magnetic moments, a new sample series will be prepared where surface oxidation will be prevented by choosing a more robust capping layer material.

Another powerful, though not yet well established element specific probe is the TEM technique EMCD, which is the electron equivalent to XMCD. Instead of circular polarized XAS it is based on electron energy-loss spectroscopy (EELS) measurements with different helicities. Since the probe is an electron beam EMCD allows for much higher spatial resolution than XMCD; however, it is a transmission technique which requires the preparation of thin samples. These are usually cut from a conventional substrate constrained thin film or bulk sample using a focused ion beam system. Moreover, the exact thickness of the specimen is crucial for the EMCD signal because of the strong interaction of the electron beam and the material, which results in strong thickness dependence of the EMCD signal (cf. Fig. 7.3).

Recently, several EMCD analyses of magnetocaloric Heusler compounds were conducted by W. Hetaba at TU Wien, on specimens which were cut from substrate constrained films or bulk material. One major problem with this kind of sample preparation for thin films undergoing a martensitic transformation is that the sample geometry is changed from a sample which is small in only one dimension to a TEM lamella that is small in two dimensions. The reduced size can hinder the martensitic transformation, and therefore

the transformation temperatures of the original thin film and the TEM lamella can differ. Another uncertainty comes from the use of Ga ions in the focused ion beam which can locally alter the composition and hence also changes the transformation temperatures. As a result, in many specimens the martensitic transformation was completely suppressed.

Single crystalline freestanding thin films, however, represent the ideal sample geometry for EMCD measurements because of the simplicity of the sample preparation and the well known and uniform thickness of the film. The transformation temperatures of the freestanding film are in fact different from the substrate constrained one but can easily be determined, e.g., by temperature dependent XRD measurement prior to the EMCD studies.

Therefore, in future studies thin ($< 50\,\mathrm{nm}$) freestanding films should be tested for EMCD studies where the substrate constrained counterpart can be examined by XMCD for direct comparison in order to study the element specific magnetic properties of the material and to advance the EMCD technique.

7.2 Pump-probe spectroscopy

The unique advantages of single crystalline freestanding films (fixed crystal orientation, uniform thickness, and easily detectable transformation temperatures) offer optimum conditions for pump-probe spectroscopy measurements because the whole sample thickness can be optically heated by a femtosecond laserpulse. With this method, the timescale of the martensitic transformation can be detected using time resolved electron diffraction and observing the intensity of the martensitic diffraction peaks as shown in Fig. 7.4. This first measurement, done by Nic Erasmus at Stellenbosch University on a $48\,\mathrm{nm}$ thick $Ni_{57.5}Mn_{19.5}Ga_{23}$ film indicates a timescale of a $400\,\mathrm{fs}$ for the martensitic transformation. The experiments will be continued in collaboration with the groups of Prof. Dr. Mehmet Acet (University of Duisburg-Essen) and Prof. Dr. Petra Rudolf (University of Groningen).
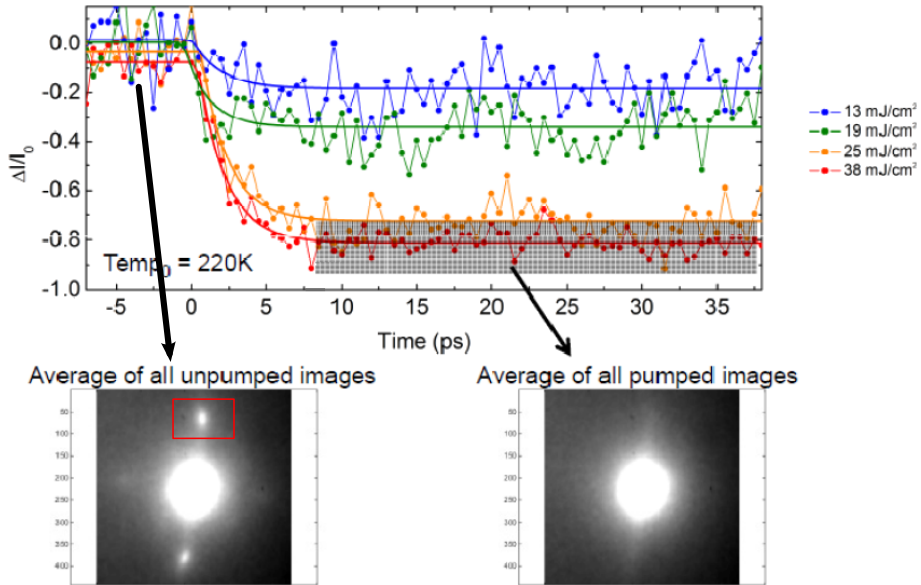
Figure 7.4. Pump-probe spectroscopy. Time resolved electron diffraction measurements of a 48 nm thick $Ni_{57.5}Mn_{19.5}Ga_{23}$ film with different pumping flux densities. $\Delta I/I_0$ describes the relative change in the intensity of the marked satellite peak belonging to the martensite phase.

Bibliography

[1] K. Ullakko, J. K. Huang, C. Kantner, R. C. O'Handley, and V. V. Kokorin, "Large magnetic-field-induced strains in Ni_2MnGa single crystals", Applied Physics Letters **69**, 1966 (1996).

[2] L. Mañosa, A. Planes, M. Acet, E. Duman, and E. F. Wassermann, "Magnetic shape memory in Ni-Mn-Ga and Ni-Mn-Al", Journal of Magnetism and Magnetic Materials **272-276**, 2090 (2004).

[3] A. Planes, L. Mañosa, and M. Acet, "Magnetocaloric effect and its relation to shape-memory properties in ferromagnetic Heusler alloys.", Journal of physics. Condensed matter : an Institute of Physics journal **21**, 233201 (2009).

[4] S. Y. Yu, L. Ma, G. D. Liu, Z. H. Liu, J. L. Chen, Z. X. Cao, G. H. Wu, B. Zhang, and X. X. Zhang, "Magnetic field-induced martensitic transformation and large magnetoresistance in NiCoMnSb alloys", Applied Physics Letters **90**, 242501 (2007).

[5] K. A. Gschneidner Jr, V. K. Pecharsky, and A. O. Tsokol, "Recent developments in magnetocaloric materials", Reports on Progress in Physics **68**, 1479 (2005).

[6] B. M. Wang, Y. Liu, P. Ren, B. Xia, K. B. Ruan, J. B. Yi, J. Ding, X. G. Li, and L. Wang, "Large Exchange Bias after Zero-Field Cooling from an Unmagnetized State", Physical Review Letters **106**, 077203 (2011).

[7] M. Khan, I. Dubenko, S. Stadler, and N. Ali, "Exchange bias in bulk Mn rich Ni–Mn–Sn Heusler alloys", Journal of Applied Physics **102**, 113914 (2007).

[8] A. Behler, N. Teichert, B. Dutta, A. Waske, T. Hickel, A. Auge, A. Hütten, and J. Eckert, "Thickness dependent exchange bias in martensitic epitaxial Ni-Mn-Sn thin films", AIP Advances **3**, 122112 (2013).

[9] N. Teichert, A. Auge, E. Yüzüak, I. Dincer, Y. Elerman, B. Krumme, H. Wende, O. Yildirim, K. Potzger, and A. Hütten, "Influence of film thickness and composition on the martensitic transformation in epitaxial Ni–Mn–Sn thin films", Acta Materialia **86**, 279 (2015).

[10] A. Auge, N. Teichert, M. Meinert, G. Reiss, A. Hütten, E. Yüzüak, I. Dincer, Y. Elerman, I. Ennen, and P. Schattschneider, "Thickness dependence of the martensitic transformation, magnetism, and magnetoresistance in epitaxial Ni-Mn-Sn ultrathin films", Physical Review B **85**, 214118 (2012).

[11] A. Auge, "The magnetic shape memory alloy Ni-Mn-Sn in thin films", Doctoral Thesis (Bielefeld University, 2012).

[12] S. Rios, D. Bufford, I. Karaman, H. Wang, and X. Zhang, "Magnetic field induced phase transformation in polycrystalline NiCoMnAl thin films", Applied Physics Letters **103**, 132404 (2013).

[13] Y. Mitsui, K. Koyama, W. Ito, R. Y. Umetsu, R. Kainuma, and K. Watanabe, "Observation of Reverse Transformation in Metamagnetic Shape Memory Alloy $Ni_{40}Co_{10}Mn_{34}Al_{16}$ by High-Field X-Ray Diffraction Measurements", Materials Transactions **51**, 1648 (2010).

[14] R. Niemann, O. Heczko, L. Schultz, and S. Fähler, "Metamagnetic transitions and magnetocaloric effect in epitaxial Ni–Co–Mn–In films", Applied Physics Letters **97**, 222507 (2010).

[15] K. Bhattacharya, *Microstructure of Martensite: Why it forms and how it gives rise to the shape-memory effect*, Oxford Series on Materials Modelling (OUP Oxford, 2003).

[16] Y. Song, K. P. Bhatti, V. Srivastava, C. Leighton, and R. D. James, "Thermodynamics of energy conversion via first order phase transformation in low hysteresis magnetic materials", Energy & Environmental Science **6**, 1315 (2013).

[17] Y. Song, C. Leighton, and R. D. James, "Thermodynamics and Energy Conversion in Heusler alloys", in *Heusler Alloys*, edited by C. Felser and A. Hirohata, Springer Series in Materials Science 222 (Springer International Publishing, 2016).

[18] S. Kaufmann, U. K. Rößler, O. Heczko, M. Wuttig, J. Buschbeck, L. Schultz, and S. Fähler, "Adaptive Modulations of Martensites", Physical Review Letters **104**, 145702 (2010).

[19] R. Niemann, "Nukleation und Wachstum des adaptiven Martensits in epitaktischen Schichten der Formgedächtnislegierung Ni-Mn-Ga", German, Doctoral Thesis (Technische Universität Dresden, 2015).

[20] A. Smith, C. R. Bahl, R. Bjørk, K. Engelbrecht, K. K. Nielsen, and N. Pryds, "Materials Challenges for High Performance Magnetocaloric Refrigeration Devices", Advanced Energy Materials **2**, 1288 (2012).

[21] V. D. Buchelnikov, V. V. Sokolovskiy, S. V. Taskaev, V. V. Khovaylo, A. A. Aliev, L. N. Khanov, A. B. Batdalov, P. Entel, H. Miki, and T. Takagi, "Monte Carlo simulations of the magnetocaloric effect in magnetic Ni–Mn–X (X = Ga, In) Heusler alloys", Journal of Physics D: Applied Physics **44**, 064012 (2011).

[22] J. Nogués and I. K. Schuller, "Exchange bias", Journal of Magnetism and Magnetic Materials **192**, 203 (1999).

[23] M. Ali, P. Adie, C. H. Marrows, D. Greig, B. J. Hickey, and R. L. Stamps, "Exchange bias using a spin glass.", Nature materials **6**, 70 (2007).

[24] M. Dove, *Structure and Dynamics: An Atomic View of Materials*, Oxford Master Series in Condensed Matter Physics 1 (OUP Oxford, 2003).

[25] P. J. Brown, A. Y. Bargawi, J. Crangle, K.-U. Neumann, and K. R. A. Ziebeck, "Direct observation of a band Jahn-Teller effect in the martensitic phase transition of Ni_2MnGa", Journal of Physics Condensed Matter **11**, 4715 (1999).

[26] J. Cui, Y. S. Chu, O. O. Famodu, Y. Furuya, J. Hattrick-Simpers, R. D. James, A. Ludwig, S. Thienhaus, M. Wuttig, Z. Zhang, and I. Takeuchi, "Combinatorial search of thermoelastic shape-memory alloys with extremely small hysteresis width.", Nature materials **5**, 286 (2006).

[27] A. Sozinov, A. A. Likhachev, N. Lanska, and K. Ullakko, "Giant magnetic-field-induced strain in NiMnGa seven-layered martensitic phase", Applied Physics Letters **80**, 1746 (2002).

[28] Y. Zhang, R. a. Hughes, J. F. Britten, W. Gong, J. S. Preston, G. A. Botton, and M. Niewczas, "Epitaxial Ni–Mn–Ga films derived through high temperature in situ depositions", Smart Materials and Structures **18**, 025019 (2009).

[29] T. Krenke, M. Acet, E. Wassermann, X. Moya, L. Mañosa, and A. Planes, "Martensitic transitions and the nature of ferromagnetism in the austenitic and martensitic states of Ni-Mn-Sn alloys", Physical Review B **72**, 014412 (2005).

[30] T. Graf, C. Felser, and S. S. Parkin, "Simple rules for the understanding of Heusler compounds", Progress in Solid State Chemistry **39**, 1 (2011).

[31] A. Khachaturyan, S. Shapiro, and S. Semenovskaya, "Adaptive phase formation in martensitic transformation", Physical Review B **43**, 10832 (1991).

[32] M. E. Gruner, S. Fähler, and P. Entel, "Magnetoelastic coupling and the formation of adaptive martensite in magnetic shape memory alloys", Physica Status Solidi (B) **251**, 2067 (2014).

[33] R. V. Kohn and S. Müller, "Branching of twins near an austenite—twinned-martensite interface", Philosophical Magazine A **66**, 697 (1992).

[34] Y. U. Wang, "Diffraction theory of nanotwin superlattices with low symmetry phase", Physical Review B **76**, 024108 (2007).

[35] W. P. and A. Piccard, "Le phénomène magnétocalorique", J. Phys. Theor. Appl. **7**, 103 (1917).

[36] A. Smith, "Who discovered the magnetocaloric effect?", The European Physical Journal H **38**, 507 (2013).

[37] G. V. Brown, "Magnetic heat pumping near room temperature", Journal of Applied Physics **47**, 3673 (1976).

[38] V. K. Pecharsky and K. A. Gschneidner, Jr., "Giant Magnetocaloric Effect in $Gd_5(Si_2Ge_2)$", Physical Review Letters **78**, 4494 (1997).

[39] G. Porcari, F. Cugini, S. Fabbrici, C. Pernechele, F. Albertini, M. Buzzi, M. Mangia, and M. Solzi, "Convergence of direct and indirect methods in the magnetocaloric study of first order transformations: The case of Ni-Co-Mn-Ga Heusler alloys", Physical Review B **86**, 104432 (2012).

[40] W. H. Meiklejohn and C. P. Bean, "New Magnetic Anisotropy", Physical Review **102**, 1413 (1956).

[41] A. K. Nayak, M. Nicklas, S. Chadov, P. Khuntia, C. Shekhar, A. Kalache, M. Baenitz, Y. Skourski, V. K. Guduru, A. Puri, U. Zeitler, J. M. D. Coey, and C. Felser, "Design of compensated ferrimagnetic Heusler alloys for giant tunable exchange bias", Nature Materials **14**, 679 (2015).

[42] Y. Fan, K. J. Smith, G. Lüpke, A. T. Hanbicki, R. Goswami, C. H. Li, H. B. Zhao, and B. T. Jonker, "Exchange bias of the interface spin system at the Fe/MgO interface", Nature Nanotechnology **8**, 438 (2013).

[43] Z. Li, C. Jing, J. Chen, S. Yuan, S. Cao, and J. Zhang, "Observation of exchange bias in the martensitic state of $Ni_{50}Mn_{36}Sn_{14}$ Heusler alloy", Applied Physics Letters **91**, 112505 (2007).

[44] M. Khan, I. Dubenko, S. Stadler, and N. Ali, "Exchange bias behavior in Ni–Mn–Sb Heusler alloys", Applied Physics Letters **91**, 072510 (2007).

[45] A. K. Pathak, M. Khan, B. R. Gautam, S. Stadler, I. Dubenko, and N. Ali, "Exchange bias in bulk Ni–Mn–In-based Heusler alloys", Journal of Magnetism and Magnetic Materials **321**, 963 (2009).

[46] R. Machavarapu and G. Jakob, "Exchange bias effect in the martensitic state of Ni-Co-Mn-Sn film", Applied Physics Letters **102**, 232406 (2013).

[47] S. Kämmerer, A. Thomas, A. Hütten, and G. Reiss, "Co_2MnSi Heusler alloy as magnetic electrodes in magnetic tunnel junctions", Applied Physics Letters **85**, 79 (2004).

[48] Y. M. Lee, J. Hayakawa, S. Ikeda, F. Matsukura, and H. Ohno, "Giant tunnel magnetoresistance and high annealing stability in CoFeB/MgO/CoFeB magnetic tunnel junctions with synthetic pinned layer", Applied Physics Letters **89**, 042506 (2006).

[49] J. M. Teixeira, J. Ventura, M. P. Fernández-García, J. P. Araujo, J. B. Sousa, P. Wisniowski, D. C. Leitao, and P. P. Freitas, "Exchange biased CoFeB-MgO tunnel junctions at the onset of perpendicular anisotropy with in-plane/out-of-plane sensing capabilities", Journal of Applied Physics **111**, 053930 (2012).

[50] P. Entel, V. V. Sokolovskiy, V. D. Buchelnikov, M. Ogura, M. E. Gruner, A. Grünebohm, D. Comtesse, and H. Akai, "The metamagnetic behavior and giant inverse magnetocaloric effect in Ni–Co–Mn–(Ga, In, Sn) Heusler alloys", Journal of Magnetism and Magnetic Materials **385**, 193 (2015).

[51] B. Krumme, A. Auge, H. C. Herper, I. Opahle, D. Klar, N. Teichert, L. Joly, P. Ohresser, J. Landers, J. P. Kappler, P. Entel, A. Hütten, and H. Wende, "Element-specific electronic structure and magnetic properties of an epitaxial $Ni_{51.5}Mn_{32.9}Sn_{15.5}$ thin film at the austenite-martensite transition", Physical Review B **91**, 214417 (2015).

[52] K. P. Bhatti, S. El-Khatib, V. Srivastava, R. James, and C. Leighton, "Small-angle neutron scattering study of magnetic ordering and inhomogeneity across the martensitic phase transformation in $Ni_{50-x}Co_x$ $Mn_{40}Sn_{10}$ alloys", Physical Review B **85**, 134450 (2012).

[53] K. P. Bhatti, V. Svivastava, D. P. Phelan, E.-K. S., R. D. James, and C. Leighton, "Magnetic Phase Competition in Off-Stoichiometric Martensitic Heusler Alloys: The $Ni_{50-x}Co_xMn_{25+y}Sn_{25-y}$ system", in *Heusler Alloys*, edited by C. Felser and A. Hirohata, Springer Series in Materials Science 222 (Springer International Publishing, 2016).

[54] S. Bedanta and W. Kleemann, "Supermagnetism", Journal of Physics D: Applied Physics **42**, 013001 (2009).

[55] S. Chatterjee and S. Majumdar, "Magnetic and Martensitic Transitions in $Ni_2Mn_{1+x}Sn_{1-x}$ Alloys", Materials Science Forum **635**, 97 (2009).

[56] BESTEC, *BERLIN*.

[57] R. Van Grieken and A. Markowicz, *Handbook of X-Ray Spectrometry, Second Edition,* Practical Spectroscopy (CRC Press, 2001).

[58] N. Teichert, A. Boehnke, A. Behler, B. Weise, A. Waske, and A. Hütten, "Exchange bias effect in martensitic epitaxial Ni-Mn-Sn thin films applied to pin CoFeB/MgO/CoFeB magnetic tunnel junctions", Applied Physics Letters **106**, 192401 (2015).

[59] *Heusler Alloy replacement for Iridium*, `www.harfir.eu`.

[60] M. Ye, A. Kimura, Y. Miura, M. Shirai, Y. T. Cui, K. Shimada, H. Namatame, M. Taniguchi, S. Ueda, K. Kobayashi, R. Kainuma, T. Shishido, K. Fukushima, and T. Kanomata, "Role of Electronic Structure in the Martensitic Phase Transition of $Ni_2Mn_{1+x}Sn_{1-x}$ Studied by Hard-X-Ray Photoelectron Spectroscopy and Ab Initio Calculation", Physical Review Letters **104**, 176401 (2010).

[61] S. Ikeda, J. Hayakawa, Y. Ashizawa, Y. M. Lee, K. Miura, H. Hasegawa, M. Tsunoda, F. Matsukura, and H. Ohno, "Tunnel magnetoresistance of 604% at 300 K by suppression of Ta diffusion in CoFeB/MgO/CoFeB pseudo-spin-valves annealed at high temperature", Applied Physics Letters **93**, 082508 (2008).

[62] J. Schmalhorst, A. Thomas, G. Reiss, X. Kou, and E. Arenholz, "Influence of chemical and magnetic interface properties of Co-Fe-B/MgO/Co-Fe-B tunnel junctions on the annealing temperature dependence of the magnetoresistance", Journal of Applied Physics **102**, 053907 (2007).

[63] Q. Meng, Y. Rong, and T. Hsu, "Nucleation barrier for phase transformations in nanosized crystals", Physical Review B **65**, 174118 (2002).

[64] G. A. Malygin, "Size effects under martensitic deformation of shape-memory alloys", Technical Physics **54**, 1782 (2009).

[65] S. Singh and C. Biswas, "Magnetoresistance origin in martensitic and austenitic phases of $Ni_2Mn_{1+x}Sn_{1-x}$", Applied Physics Letters **98**, 212101 (2011).

[66] E. Yüzüak, I. Dincer, Y. Elerman, A. Auge, N. Teichert, and A. Hütten, "Inverse magnetocaloric effect of epitaxial Ni-Mn-Sn thin films", Applied Physics Letters **103**, 222403 (2013).

[67]   S. Aksoy, M. Acet, P. P. Deen, L. Mañosa, and A. Planes, "Magnetic correlations in martensitic Ni-Mn-based Heusler shape-memory alloys: Neutron polarization analysis", Physical Review B **79**, 212401 (2009).

[68]   V. V. Sokolovskiy, V. D. Buchelnikov, M. A. Zagrebin, P. Entel, S. Sahool, and M. Ogura, "First-principles investigation of chemical and structural disorder in magnetic $Ni_2Mn_{1+x}Sn_{1-x}$ Heusler alloys", Physical Review B **86**, 134418 (2012).

[69]   S. Ikeda, K. Miura, H. Yamamoto, K. Mizunuma, H. D. Gan, M. Endo, S. Kanai, J. Hayakawa, F. Matsukura, and H. Ohno, "A perpendicular-anisotropy CoFeB-MgO magnetic tunnel junction.", Nature materials **9**, 721 (2010).

[70]   A. Anguelouch, B. D. Schrag, G. Xiao, Y. Lu, P. L. Trouilloud, R. A. Wanner, W. J. Gallagher, and S. S. P. Parkin, "Two-dimensional magnetic switching of micron-size films in magnetic tunnel junctions", Applied Physics Letters **76**, 622 (2000).

[71]   J. Hayakawa, S. Ikeda, F. Matsukura, H. Takahashi, and H. Ohno, "Dependence of giant tunnel magnetoresistance of sputtered CoFeB/MgO/CoFeB magnetic tunnel junctions on MgO barrier thickness and annealing temperature", Japanese Journal of Applied Physics **44**, L587 (2005).

[72]   A. Diestel, A. Backen, V. Neu, L. Schultz, and S. Fähler, "Magnetic domain structure of epitaxial Ni–Mn–Ga films", Scripta Materialia **67**, 423 (2012).

[73]   A. Kovacs, A. Kohn, J. Dean, T. Schrefl, A. Zeltser, and M. Carey, "Reversal Mechanism of Exchange-Biased CoFeB/IrMn Bilayers Observed by Lorentz Electron Microscopy", IEEE Transactions on Magnetics **45**, 3873 (2009).

[74]   N. Teichert, D. Kucza, O. Yildirim, E. Yuzuak, I. Dincer, A. Behler, B. Weise, L. Helmich, A. Boehnke, S. Klimova, A. Waske, Y. Elerman, and A. Hütten, "Structure and giant inverse magnetocaloric effect of epitaxial Ni-Co-Mn-Al films", Physical Review B **91**, 184405 (2015).

[75]   V. D. Buchelnikov and V. V. Sokolovskiy, "Magnetocaloric effect in Ni-Mn-X (X = Ga, In, Sn, Sb) Heusler alloys", **112**, 633 (2011).

[76] M. Khan, N. Ali, and S. Stadler, "Inverse magnetocaloric effect in ferromagnetic $Ni_{50}Mn_{37+x}Sb_{13-x}$ Heusler alloys", Journal of Applied Physics **101**, 053919 (2007).

[77] Z. D. Han, D. H. Wang, C. L. Zhang, H. C. Xuan, J. R. Zhang, B. X. Gu, and Y. W. Du, "The phase transitions, magnetocaloric effect, and magnetoresistance in Co doped Ni–Mn–Sb ferromagnetic shape memory alloys", Journal of Applied Physics **104**, 053906 (2008).

[78] S. Fabbrici, J. Kamarad, Z. Arnold, F. Casoli, a. Paoluzi, F. Bolzoni, R. Cabassi, M. Solzi, G. Porcari, and C. Pernechele, "From direct to inverse giant magnetocaloric effect in Co-doped NiMnGa multifunctional alloys", Acta Materialia **59**, 412 (2011).

[79] R. Kainuma, Y. Imano, W. Ito, Y. Sutou, H. Morito, S. Okamoto, O. Kitakami, K. Oikawa, A. Fujita, T. Kanomata, and K. Ishida, "Magnetic-field-induced shape recovery by reverse phase transformation.", Nature **439**, 957 (2006).

[80] R. Kainuma, Y. Imano, W. Ito, H. Morito, Y. Sutou, K. Oikawa, A. Fujita, K. Ishida, S. Okamoto, O. Kitakami, and T. Kanomata, "Meta-magnetic shape memory effect in a Heusler-type $Ni_{43}Co_7Mn_{39}Sn_{11}$ polycrystalline alloy", Applied Physics Letters **88**, 192513 (2006).

[81] R. Kainuma, W. Ito, R. Y. Umetsu, K. Oikawa, and K. Ishida, "Magnetic field-induced reverse transformation in B2-type NiCoMnAl shape memory alloys", Applied Physics Letters **93**, 091906 (2008).

[82] S. Morito and K. Otsuka, "Electron microscopy of new martensites with long period stacking order structures in $Ni_{50}Al_xMn_{50-x}$ alloys I. Structures and morphologies", Materials Science and Engineering: A **208**, 47 (1996).

[83] R. Kainuma, K. Ishida, and H. Nakano, "Martensitic transformations in NiMnAl β phase alloys", Metallurgical and Materials Transactions A **27**, 4153 (1996).

[84] A. Fujita, K. Fukamichi, F. Gejima, R. Kainuma, and K. Ishida, "Magnetic properties and large magnetic-field-induced strains in off-stoichiometric Ni–Mn–Al Heusler alloys", Applied Physics Letters **77**, 3054 (2000).

[85] M. Acet, E. Duman, E. F. Wassermann, L. Mañosa, and A. Planes, "Coexisting ferro- and antiferromagnetism in Ni_2MnAl Heusler alloys", Journal of Applied Physics **92**, 3867 (2002).

[86] X. Xu, W. Ito, M. Tokunaga, R. Y. Umetsu, R. Kainuma, and K. Ishida, "Kinetic Arrest of Martensitic Transformation in NiCoMnAl Metamagnetic Shape Memory Alloy", Materials Transactions **51**, 1357 (2010).

[87] H. Xuan, F. Chen, P. Han, D. Wang, and Y. Du, "Effect of Co addition on the martensitic transformation and magnetocaloric effect of Ni–Mn–Al ferromagnetic shape memory alloys", Intermetallics **47**, 31 (2014).

[88] Y. Kim, E. J. Kim, K. Choi, W. B. Han, H. S. Kim, Y. Shon, and C. S. Yoon, "Room-temperature magnetocaloric effect of Ni-Co-Mn-Al Heusler alloys", **616**, 66 (2014).

[89] A. Backen, S. R. Yeduru, M. Kohl, S. Baunack, A. Diestel, B. Holzapfel, L. Schultz, and S. Fähler, "Comparing properties of substrate-constrained and freestanding epitaxial Ni–Mn–Ga films", Acta Materialia **58**, 3415 (2010).

[90] S. Kaufmann, R. Niemann, T. Thersleff, U. K. Rößler, O. Heczko, J. Buschbeck, B. Holzapfel, L. Schultz, and S. Fähler, "Modulated martensite: why it forms and why it deforms easily", New Journal of Physics **13**, 053029 (2011).

[91] J. Buschbeck, R. Niemann, O. Heczko, M. Thomas, L. Schultz, and S. Fähler, "In situ studies of the martensitic transformation in epitaxial Ni–Mn–Ga films", Acta Materialia **57**, 2516 (2009).

[92] J. Pons, V. Chernenko, R. Santamarta, and E. Cesari, "Crystal structure of martensitic phases in Ni–Mn–Ga shape memory alloys", Acta Materialia **48**, 3027 (2000).

[93] B. Dutta, T. Hickel, J. Neugebauer, C. Behler, S. Fähler, A. Behler, A. Waske, N. Teichert, J.-M. Schmalhorst, and A. Hütten, "Interplay of strain and interdiffusion in Heusler alloy bilayers", physica status solidi (RRL) - Rapid Research Letters **9**, 321 (2015).

[94]   M. Thomas, O. Heczko, J. Buschbeck, U. K. Rößler, J. McCord, N. Scheerbaum, L. Schultz, and S. Fähler, "Magnetically induced reorientation of martensite variants in constrained epitaxial Ni–Mn–Ga films grown on MgO(001)", New Journal of Physics **10**, 023040 (2008).

[95]   J. W. Dong, "Shape memory and ferromagnetic shape memory effects in single-crystal Ni_2MnGa thin films", Journal of Applied Physics **95**, 2593 (2004).

[96]   M. Siewert, M. E. Gruner, A. Dannenberg, A. Chakrabarti, H. C. Herper, M. Wuttig, S. R. Barman, S. Singh, A. Al-Zubi, T. Hickel, J. Neugebauer, M. Gillessen, R. Dronskowski, and P. Entel, "Designing shape-memory Heusler alloys from first-principles", Applied Physics Letters **99**, 191904 (2011).

[97]   S. Kustov, M. L. Corró, J. Pons, and E. Cesari, "Entropy change and effect of magnetic field on martensitic transformation in a metamagnetic Ni–Co–Mn–In shape memory alloy", Applied Physics Letters **94**, 191901 (2009).

[98]   D. Cong, S. Roth, and L. Schultz, "Magnetic properties and structural transformations in Ni–Co–Mn–Sn multifunctional alloys", Acta Materialia **60**, 5335 (2012).

[99]   N. Wu, X. He, A. L. Wysocki, U. Lanke, T. Komesu, K. D. Belashchenko, C. Binek, and P. A. Dowben, "Imaging and Control of Surface Magnetization Domains in a Magnetoelectric Antiferromagnet", Physical Review Letters **106**, 087202 (2011).

[100] M. D. Mukadam, S. M. Yusuf, and P. Bhatt, "Tuning the magnetocaloric properties of the $Ni_{2+x}Mn_{1-x}Sn$ Heusler alloys", Journal of Applied Physics **113**, 173911 (2013).

[101] S. Dan'kov, a. Tishin, V. Pecharsky, and K. Gschneidner, "Magnetic phase transitions and the magnetothermal properties of gadolinium", Physical Review B **57**, 3478 (1998).

[102] A. Diestel, R. Niemann, B. Schleicher, S. Schwabe, L. Schultz, and S. Fähler, "Field-temperature phase diagrams of freestanding and substrate-constrained epitaxial Ni-Mn-Ga-Co films for magnetocaloric applications", Journal of Applied Physics **118**, 023908 (2015).

[103] F. Guillou, H. Yibole, G. Porcari, L. Zhang, N. H. van Dijk, and E. Brück, "Magnetocaloric effect, cyclability and coefficient of refrigerant performance in the MnFe(P, Si, B) system", Journal of Applied Physics **116**, 063903 (2014).

[104] V. Srivastava, X. Chen, and R. D. James, "Hysteresis and unusual magnetic properties in the singular Heusler alloy $Ni_{45}Co_5Mn_{40}Sn_{10}$", Applied Physics Letters **97**, 014101 (2010).

[105] E. K. Liu, W. Zhu, L. Feng, J. L. Chen, W. H. Wang, G. H. Wu, H. Y. Liu, F. B. Meng, H. Z. Luo, and Y. X. Li, "Vacancy-tuned paramagnetic/ferromagnetic martensitic transformation in Mn-poor Mn_{1-x}Co-Ge alloys", EPL (Europhysics Letters) **91**, 17003 (2010).

[106] N. H. Dung, L. Zhang, Z. Q. Ou, L. Zhao, L. Van Eijck, A. M. Mulders, M. Avdeev, E. Suard, N. H. Van Dijk, and E. Brück, "High/low-moment phase transition in hexagonal Mn-Fe-P-Si compounds", Physical Review B **86**, 045134 (2012).

[107] M. Trassinelli, M. Marangolo, M. Eddrief, V. H. Etgens, V. Gafton, S. Hidki, E. Lacaze, E. Lamour, C. Prigent, J.-P. Rozet, S. Steydli, Y. Zheng, and D. Vernhet, "Suppression of the thermal hysteresis in magnetocaloric MnAs thin film by highly charged ion bombardment", Applied Physics Letters **104**, 081906 (2014).

[108] J. Liu, T. Gottschall, K. P. Skokov, J. D. Moore, and O. Gutfleisch, "Giant magnetocaloric effect driven by structural transitions.", Nature materials **11**, 620 (2012).

[109] T. Zhou, M. Cher, L. Shen, J. Hu, and Z. Yuan, "On the origin of giant magnetocaloric effect and thermal hysteresis in multifunctional α-FeRh thin films", Physics Letters A **377**, 3052 (2013).

[110] J. C. Debnath, J. H. Kim, Y. Heo, A. M. Strydom, and S. X. Dou, "Correlation between structural parameters and the magnetocaloric effect in epitaxial $La_{0.8}Ca_{0.2}MnO_2/LaAlO_3$ thin film", Journal of Applied Physics **113**, 063508 (2013).

[111] M. Wodniok, in preparation, Masters Thesis (Bielefeld University, 2016).

[112] B. Schleicher, R. Niemann, A. Diestel, R. Hühne, L. Schultz, and S. Fähler, "Epitaxial Ni-Mn-Ga-Co thin films on PMN-PT substrates for multicaloric applications", Journal of Applied Physics **118**, 053906 (2015).

[113] X. Xu, W. Ito, T. Kanomata, and R. Kainuma, "Entropy Change during Martensitic Transformation in $Ni_{50-x}Co_xMn_{50-y}Al_y$ Metamagnetic Shape Memory Alloys", Entropy **16**, 1808 (2014).

[114] X. Xu, M. Nagasako, M. Kataoka, R. Y. Umetsu, T. Omori, T. Kanomata, and R. Kainuma, "Anomalous physical properties of Heusler-type $Co_2Cr(Ga, Si)$ alloys and thermodynamic study on reentrant martensitic transformation", Physical Review B **91**, 104434 (2015).

[115] J. C. Lang, "X-ray Magnetic Circular Dichroism", in *Characterization of Materials*, edited by E. Kaufmann (John Wiley & Sons, Inc., 2003).

[116] W. Hetaba, "The theory and application of inelastic coherence in the electron microscope", Doctoral Thesis (Technische Universität Wien, 2015).

Publications

1. A. Auge, N. Teichert, M. Meinert, G. Reiss, A. Hütten, E. Yüzüak, I. Dincer, Y. Elerman, I. Ennen, and P. Schattschneider, "Thickness dependence of the martensitic transformation, magnetism, and magnetoresistance in epitaxial Ni-Mn-Sn ultrathin films", Physical Review B, **84**, 214118 (2012).

2. A. Behler, N. Teichert, B. Dutta, A. Waske, T. Hickel. A. Auge, A. Hütten, and J. Eckert, "Thickness dependent exchange bias in martensitic epitaxial Ni-Mn-Sn thin films", AIP Advances **3**, 122112 (2013).

3. E. Yüzüak, I. Dincer, Y. Elerman, A. Auge, N. Teichert, and A. Hütten, "Inverse magnetocaloric effect of epitaxial Ni-Mn-Sn thin films", Applied Physics Letters **103**, 222403 (2013).

4. C. Wang, J. Meyer, N. Teichert, A. Auge, E. Rausch, B. Balke, A. Hütten, G. H. Fecher, C. Felser, "Heusler nanoparticles for spintronics and ferromagnetic shape memory alloys", Journal of Vacuum Science & Technology B **32**, 020802 (2014).

5. N. Teichert, A. Auge, E. Yüzüak, I. Dincer, Y. Elerman, B. Krumme, H. Wende, O. Yildirim, K. Potzger, and A. Hütten, "Influence of film thickness and composition on the martensitic transformation in epitaxial Ni-Mn-Sn thin films", Acta Materialia **86**, 279 (2015).

6. B. Dutta, T. Hickel, J. Neugebauer, C. Behler, S. Fähler, A. Behler, A. Waske, N. Teichert, J.-M. Schmalhorst, and A. Hütten, "Interplay of strain and interdiffusion in Heuser alloy bilayers", Physica Status Solidi (RRL) – Rapid Research Letters **9**, 321 (2015).

7. N. Teichert, A. Boehnke, A. Behler, B. Weise, A. Waske, and A. Hütten, "Exchange bias effect in martensitic epitaxial Ni-Mn-Sn thin films applied to pin CoFeB/MgO/CoFeB magnetic tunnel junctions", Applied Physics Letters **106**, 192401 (2015).

8. N. Teichert, D. Kucza, O. Yildirim, E. Yuzuak, I. Dincer, A. Behler, B. Weise, L. Helmich, A. Boehnke, S. Klimova, A. Waske, Y. Elerman, and A. Hütten, "Structure and giant inverse magnetocaloric effect of epitaxial Ni-Co-Mn-Al films", Physical Review B **91**, 184405 (2015).

9. B. Krumme, A. Auge, H. C. Herper, I. Opahle, D. Klar, N. Teichert, L. Joly, P. Ohresser, J. Landers, J. P. Kappler, P. Engel, A. Hütten, and H. Wende, "Element-specific electronic structure and magnetic properties of an epitaxial $Ni_{51.6}Mn_{32.9}Sn_{15.5}$ thin film at the austenite-martensite transition", Physical Review B **91**, 214417 (2015).

10. J. Meyer, N. Teichert, A. Auge, C. Wang, A. Hütten, and C. Felser, "Heusler Compounds Go Nano", in *Heusler Alloys*, edited by C. Felser and A. Hirohata, Springer Series in Materials Science 222 (Springer International Publishing, 2016).

Conferences

03/2012 Talk at the **76th Deutsche Physikalische Gesellschaft spring meeting**, Berlin, Germany.

03/2013 Poster at the **77th Deutsche Physikalische Gesellschaft spring meeting**, Regensburg, Germany.

05/2013 Talk at the **International Conference on Shape Memory and Superelastic Technology 2013**, Prague, Czech Republic.

07/2013 Talk at the **SPP 1599 Convention**, Lichtenfels, Germany.

09/2013 Talk at the **Fifth Seeheim Conference on Magnetism**, Frankfurt, Germany.

12/2013 Talk at the **SPP 1599 Focus Meeting A – Magnetocaloric materials**, Darmstadt, Germany.

04/2014 Poster at the **78th Deutsche Physikalische Gesellschaft spring meeting**, Dresden, Germany.

06/2014 Talk at the **SPP 1599 Convention**, Meißen, Germany.

07/2014 Poster at the **International Conference on Martensitic Transformations 2014**, Bilbao, Spain.

11/2014 Two posters at the **59th Annual Magnetism and Magnetic Materials (MMM) conference**, Honolulu(HI), USA.

12/2014 Co-organizer of the **SPP 1599 Focus Meeting A – Magnetocaloric materials**, Bielefeld, Germany.

03/2015 Talk at the **79th Deutsche Physikalische Gesellschaft spring meeting**, Berlin, Germany.

05/2015 Talk at the **IEEE International Magnetics Conference (INTERMAG) 2015**, Beijing, China.

09/2015 Talk (invited) at the **EMN Spain Meeting**, San Sebastian, Spain.

Danksagung

Für die Unterstützung, die ich beim Erstellen meiner Doktorarbeit erhalten habe, und die zum Erfolg dieser Arbeit beigetragen hat, bin ich vielen Menschen zu großem Dank verpflichtet. Ich möchte daher an dieser Stelle einigen von ihnen meinen besonderen Dank aussprechen.

Als erstes danke ich meinem Doktorvater Prof. Dr. Andreas Hütten, der es mir ermöglicht hat, meine Arbeit in seiner Gruppe durchzuführen, und mich während dieser Zeit hervorragend betreut hat.

Für die gute Zusammenarbeit auf dem Gebiet der Magnetokalorik danke ich meinem Kollegen Lars Helmich und meinen aktuellen und ehemaligen Studenten Timo Oberbiermann, Thomas Hederer, Daniel Kucza, Marius Wodniok und Nikolaus Derksen. Besonderer Dank gebührt auch meinem ehemaligen Betreuer, Dr. Alexander Auge, der durch seine Vorarbeit auf dem Gebiet der Formgedächtnislegierungen in Dünnschichten den Anstoß für diese Arbeit geliefert hat. Ich danke außerdem Alexander Böhnke für Elektronenstrahllithografie an meinen Proben und Hilfestellung bei AFM-Messungen und Martin Gottschalk für seine Geduld mit meinen Proben an der FIB. Dr. Christoph Klewe und Dr. Markus Meinert danke ich für Unterstützung bei der Probenherstellung und Fabian Schmidt-Michels für die Hilfe beim Bau eines Kryostaten für das Röntgendiffraktometer.

Größter Dank gebührt auch Dr. Karsten Rott für seine große Hilfsbereitschaft und für die Instandhaltung der Laborausrüstung und Aggi Windmann für häufige und schnelle Hilfe bei Verwaltungsaufgaben.

Bedanken möchte ich mich auch bei den Kollaborationspartnern dieser Arbeit und allen Co-Autoren, die durch wichtige Messungen und Diskussionen zu meinen Veröffentlichungen beigetragen haben. Insbesondere bedanke ich mich bei Gizem Durak Yüzüak, Dr. Ercument Yüzüak, Dr. Ilker Dincer

und Dr. Yalcin Elerman von der Universität Ankara, die durch ihre Aufenthalte in Bielefeld und meinen dreiwöchigen Aufenthalt in Ankara in vielerlei Hinsicht zu dieser Arbeit beigetragen haben. Des Weiteren bin ich meinen Kollaborationspartnern Tilmann Hickel, Biswanath Dutta und Anja Waske für viele wissenschaftliche Diskussionen und gemeinsame Veröffentlichungen zu Dank verpflichtet. Für Magnetisierungsmessungen an meinen Proben, ohne die meine Arbeit so nicht möglich gewesen wäre, danke ich Anna Behler und Bruno Weise, Oguz Yildirim, und Dr. Ercument Yüzüak. Dr. Walid Hetaba danke ich für zahlreiche HRTEM-Aufnahmen und EMCD-Messungen an meinen Proben an der TU Wien und Dr. Markus Meinert und Jan-Michael Schmalhorst für viele Hilfestellungen und XMCD-Messungen an der ALS, Berkeley[1].

Für eine angenehme Arbeitsatmosphäre danke ich der gesamten Arbeitsgruppe D2 und insbesondere Dr. Christoph Klewe, Alessia Niesen, Aggi Windmann, Alexander Böhnke, Christian Sterwerf, Dr. Daniel Meier, Marianne Bartke, Martin Gottschalk, Manuel Glas, Markus Schäfers, Niko Derksen, Polina Bougiatioti, Orestis Manos, Robin Silber, Stefan Niehörster und meinen ehemaligen Kollegen Nadine Mill, Dr. Frank Wittbracht, Katrin Eckstedt und Peter Hedwig.

Niko Derksen, Martin Gottschalk und Peter Hedwig danke ich außerdem für das Korrekturlesen dieser Arbeit.

Ich danke der Deutschen Forschungsgemeinschaft (DFG) für ihre finanzielle Unterstützung im Rahmen des Schwerpunktprogramms Ferroic Cooling (SPP 1599).

Ich danke an dieser Stelle auch Prof. Dr. Thomas Huser, der sich bereit erklärt hat, meine Arbeit als Zweitgutachter zu lesen und zu bewerten.

Abschließend möchte ich mich ganz besonders bei meiner Familie und meinem engen Freundeskreis bedanken. Sie haben mir während meines Studiums und während meiner Doktorandenzeit immer zur Seite gestanden und mir dadurch erst diese Doktorarbeit ermöglicht.

---

[1]The Advanced Light Source is supported by the Director, Office of Science, Office of Basic Energy Sciences, of the U.S. Department of Energy under Contract No. DE-AC02-05CH11231.